STUDY OF GALVANIC DISPLACEMENT REACTION OF METAL NANOSTRUCTURES ON SEMICONDUCTOR SURFACES USING TRANSMISSION ELECTRON MICROSCOPY

by

Tapas Ghosh

(Enrolment No.-PHYS05201204013)

Saha Institute of Nuclear Physics, Kolkata

A thesis submitted to the
Board of Studies in Physical Sciences

In partial fulfillment of requirements
for the degree of
DOCTOR OF PHILOSOPHY
of
HOMI BHABHA NATIONAL INSTITUTE

August, 2017

Homi Bhabha National Institute

Recommendations of the Viva Voce Committee

As members of the Viva Voce Committee, we certify that we have read the dissertation prepared by TAPAS GHOSH entitled "STUDY OF GALVANIC DISPLACEMENT REACTION OF METAL NANOSTRUCTURES ON SEMICONDUCTOR SURFACES USING TRANSMISSION ELECTRON MICROSCOPY" and recommend that it may be accepted as fulfilling the thesis requirement for the award of Degree of Doctor of Philosophy.

Chairman - Prof. Satyaranjan Bhattacharyya	**Date:**
SBhattacharyya	21/12/2017
Guide / Convener - Dr. Biswarup Satpati	**Date:**
Biswarup Satpati	21/12/2017
Co-guide - NA	**Date:**
Examiner – Prof. Dipak Kumar Goswami	**Date:**
DKGoswami	21/12/17
Member 1- Prof. Tapas Kumar Chini	**Date:**
Tapas Kumar Chini	21/12/2017
Member 2- Prof. Supratic Chakraborty	**Date:**
Supratic Chakraborty	21/12/17

Final approval and acceptance of this thesis is contingent upon the candidate's submission of the final copies of the thesis to HBNI.

I/~~We~~ hereby certify that I/~~we~~ have read this thesis prepared under my/~~our~~ direction and recommend that it may be accepted as fulfilling the thesis requirement.

Date: 21-12-2017

Place: Kolkata

Biswarup Satpati

Co-guide (if applicable)

Guide

STATEMENT BY AUTHOR

This dissertation has been submitted in partial fulfillment of requirements for the doctoral degree at Homi Bhabha National Institute (HBNI) and is deposited in the Library to be made available to borrowers under rules of the HBNI.

Brief quotations from this dissertation are allowable without special permission, provided that accurate acknowledgement of source is made. Requests for permission for extended quotation from or reproduction of this manuscript in whole or in part may be granted by the Competent Authority of HBNI when in his or her judgment the proposed use of the material is in the interests of scholarship. In all other instances, however, permission must be obtained from the author.

Tapas Ghosh

DECLARATION

I, hereby declare that the investigation presented in the thesis has been carried out by me. The work is original and has not been submitted earlier as a whole or in part for a degree / diploma at this or any other Institution / University.

Tapas Ghosh

List of Publications arising from the thesis

Peer reviewed Journals:

1. *Electrochemical Ostwald Ripening and Surface Diffusion in the Galvanic Displacement Reaction: Control Over Particle Growth.*
   T. Ghosh, P. Karmakar and B. Satpati, *RSC. Adv.* **2015**, 5, 94380-94387.

2. *Role of oxygen in wetting of copper nanoparticles on silicon surfaces at elevated temperature.*
   T. Ghosh and B. Satpati, *Beilstein J. Nanotechnol.* **2017**, 8, 425-433.

Conference proceeding:

1. *Substrate Decomposition in Galvanic Displacement Reaction: Contrast between Gold and Silver Nanoparticle Formation.*
   T. Ghosh, D. Kabiraj and B. Satpati, *AIP Conf. Proc.* **2015**, 1665, 080040(1)-080040(3).

2. *Galvanic displacement reaction and rapid thermal annealing in size/shape controlling silver nanoparticles on silicon substrate.*
   T. Ghosh and B. Satpati, *AIP Conf. Proc.* **2017**, 1832, 080049(1)-080049(3).

Tapas Ghosh

To my "Family and Friends"

Acknowledgements

In spite, the beginning was principally academic, the knowledge acquiring was never subjective rather it was more diverse. Thus, arriving at the completion of this thesis work, I must express my gratitude to the people, who enriched the journey. I apologise if I forget to mention anyone at this moment.

At first I would like to sincerely thank my thesis supervisor Dr. Biswarup Satpati. His dedication and ability to stick with problems, was always a great support. Without his stretching hand, the work would remain incomplete.

I thank my doctoral committee members, Prof. Satyaranjan Bhattacharyya, Prof. Tapas Kumar Chini and Prof. Supratic Chakraborty for their continuous encouragement.

I thankfully acknowledge our collaborators, Dr. Prasanta Karmakar, Dr. Debdulal Kabiraj and my lab members, Tanmay Da, Gourab, Abhijit, Bipasha.

I am grateful to SPMS division members, lab assistants and my seniors.

I thank all the MSA-1 hostel boarders and my Post M.Sc. batchmates.

I would like to thank the free work environment of my beloved SINP.

Finally I extend my gratitude to all of my friends and my family.

SINP, Kolkata

August, 2016 Tapas Ghosh

Contents

Synopsis

Significant differences arise when bulk material is brought down to nanometer size, which lead to many scientific improvement. The modification of characteristics of nanomaterials from their bulk materials can be exemplified as improved catalytic property, band gap modulation, electric field enhancement on electromagnetic wave irradiation and many more [1–3]. The novel properties of nanomaterials provide diverse application such as electronic devise, chemical sensor, drug delivery, cancer therapy etc [3–5]. Reducing size provides a large surface to volume ratio, which is one of the different parameters, defining the fascinating properties of the nanomaterials. Apart from the size, the shape of the nanomaterials also plays an important role in their characteristics. Generally the nanoparticles are synthesised in colloidal solution. Few such colloidal synthesis processes are viz., seed mediated growth, thermal synthesis, template assisted growth. Advantage of colloidal synthesis is the controllability of size and shape of the nanoparticles. Nanoparticles can be synthesised up to few nanometer size and different shape that includes one dimensional, multifaceted, hollow shaped, core shell and other nanostructure [6–9]. Apart from the application of nanoparticles in colloidal form, metal nanopaticles arrangement on semiconductor surfaces has become indispensable in electronic industry and many other applications. Nanoparticles of noble metal are of special interest because of their unique physical property and technological importance. Thus the combination of the noble metal nanopaticles and semiconductor is more noticeable in the metal semiconductor conjugate. For instance, noble metal nanostucture on semiconductor surfaces provide the opportunity to implement them as bio-sensor [5]. Again deposition of noble metal nanoparticles on silcon solar cell surfaces increases its absorption efficiency [10]. The exclusive optical properties of nanoparticle arises due to the surface plasmon resonance (SPR) between the free electrons and incident electromagnetic wave and surprisingly the surface plasmon resonance frequency of noble metal nanoparticles lies in the visible wavelength range [11]. Characterization of nanoparticles is important to perceive their properties and to make them more convenient for industrial application, where principal hinderance is their tiny size. Transmission electron microscope (TEM) is one of the leading instrument to study many properties of nanoparticles, substrate supported nanoparticles and their interface property using cross-sectional mode with atomic level resolution. Assembling of metal nanoparticles on substrate can be done using different ways. The nanoparticles can be synthesised initially in the colloidal form

and then they can be applied on the substrate by immersing the substrate into the nanoparticle solution or spraying the nanoparticle solution on the substrate [11, 12]. Metal nanoparticles can also be deposited by chemical vapor deposition (CVD), thermal evaporation, pulsed laser deposition (PVD)[13–15]. Better adhesion and hence versatility in nanoparticle shape formation, galvanic displacement reaction (GDR) process has become an efficient candidate for metal particle deposition on semiconductor as well as different metal surfaces [16]. Another important feature of the GDR is its selectivity; nanoparticles of two different elements can be deposited on a substrate, without affecting the structure of one another. Different shaped nanoparticles such as nanobelt, nanoinukshuk, nanodendrite, nanosphere, have been fabricated by GDR in recent time [17, 18]. The GDR has also been utilized in microelectro-mechanical systems (MEMS), sensor technology and solar cell application [4, 18, 19]. In the present thesis work, the underlying mechanism and control in achieving uniform size in GDR of noble metal naoaprticles on semiconductor surfaces have been studied using scanning/transmission electron microscopy (S/TEM), atomic force microscopy (AFM), scanning electron microscopy (SEM). The thesis work has been divided mainly into two parts. In the first part, the galvanic displacement of noble metal nanoparticles on semiconductor substrate has been studied by modifying the substrate surface by ion irradiation and subsequently thin film deposition. In the second part the thermal evolution of the naoparticles on semiconductor surfaces has been investigated.

The general condition for occurrence of GDR is having a net positive electrode potential between the elements. GDR between Ag and Ge can be described by two half-cell reaction as,

$$Ge \rightarrow Ge^{4+} + 4e^{-} \quad (E^0 = -0.12V)$$
$$Ag^{+} + e^{-} \rightarrow Ag \quad (E^0 = 0.8V)$$

We have performed GDR on crystalline and amorphous Ge substrates. To obtain the amorphous Ge layer, cleaned and degreased Ge(100) substrates were bombarded with a 14 keV mass analyzed oxygen beam at a normal angle of incidence (0^o) with a fluence of 1.8×10^{18} ions/cm^2. Then the crystalline and ion bombarded Ge substrates were dipped into 1 mM $AgNO_3$ solution in different containers to complete the reaction in same experimental environment.

AFM images (figure 1(a) and 1(b)) show the Ag particle formed by GDR on crystalline and ion bombarded amorphous Ge surface. Elemental mapping (figure 1(d)) by collecting X-rays from the rectangular areas of the cross sectional high

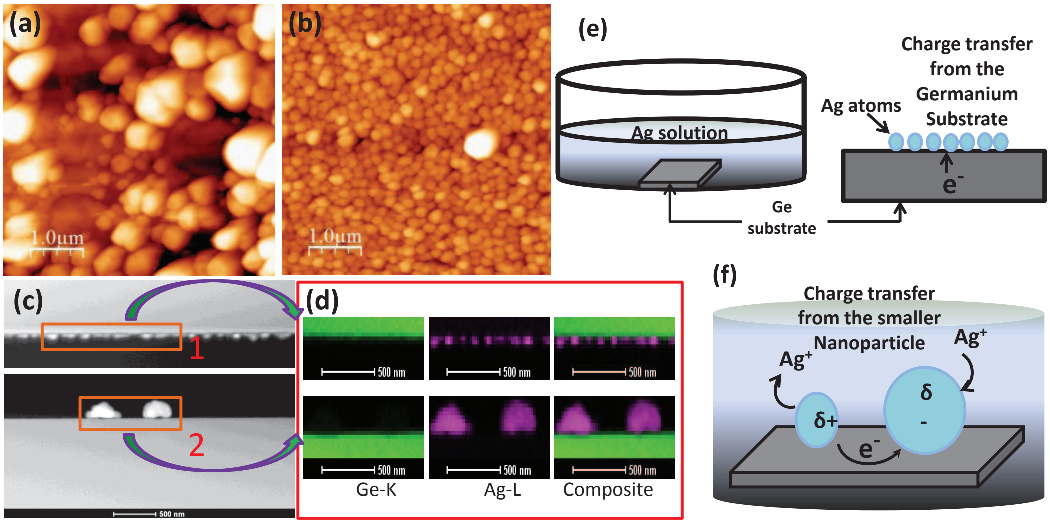

Figure 1: *AFM images of Ag nanoparticles on (a) crystalline, (b) O^+ ion bombarded Ge substrate. (c) cross sectional STEM-HAADF image of Ag nanoparticles deposited on the crystalline (bottom) and ion bombarded (top) Ge substrate. (d) elemental mapping of the areas marked by 1 and 2 in (c). Illustration of (e) galvanic displacement reaction, (f) electrochemical Ostwald ripening.*

angle annular dark field scanning TEM (STEM-HAADF) image (figure 1(c)) of Ag particles on crystalline and amorphous Ge substrate together, describes Ag (indicated by pink) and Ge (indicated in green) elemental distribution precisely. From these AFM and cross sectional TEM analysis one can see the formation of Ag nanoparticles on Ge surfaces. On can also observe that Ag nanoparticles formed on crystalline Ge (c-Ge) substrate are big and random in size but particles formed on ion bombarded amorphous Ge (a-Ge) surface are small and uniform in size. To explain this different particle formation on crystalline and amorphous Ge substrate, we incorporate the idea of electrochemical Ostwald ripening, which arises because of size dependent electrochemical potential described by Plieth's equation,

$$\triangle E = -\frac{2M\gamma}{zFr} \tag{1}$$

where M, γ, z, and F represent the molar volume, surface free energy, lowest valence state, and Faraday constant, respectively and r is the radius (assuming a spherical shape) of the particle. Thus when the size of the particles are reduced, the electrode potential will be shifted negatively . On the crystalline Ge surface, initially Ag atoms are deposited on the Ge surface by GDR (figure 1(e)). All these particles are not of exact same size. In electrical equilibrium larger particles possess a partial negative charge compared to smaller particles as the Ag^+ ion density near the bigger particles decreases in the solution. This size difference introduces electrochemical Ostwald ripening during the GDR, where the Ag^+ ions got deposited on to the bigger nanoparticles which possess partial negative charge and the electrons are supplied by the smaller particles resulting in Ag^+ ion release from the smaller particles into the solution (figure. 1(f)). Here the GDR also continue at the same time but the emergence of Ostwald ripening makes the particle formation irregular. Now Ag particles grown on ion bombarded amorphous Ge surface shows lesser contact angle, so they have larger radius of curvature. Thus from the Equation 4.1, the negative shift in the electrode potential will be less, so the Ag particles will not be oxidized easily and the Ostwald ripening will not be dominant. Again the amorphization of the substrate lead to decrement in the conductivity, hence the charge transfer from the smaller particles to the bigger particles will be prevented. Thus the amorphization of the substrate introduces hinderance in the Ostwald ripening that gives rise to a uniform particle formation. In this way electrochemical Ostwald ripening plays an important role in particle growth by galvanic displacement and by introducing defects controlled particle growth can be achieved. Rate of substrate decomposition in GDR has also been studied. Ag and Au particles deposited on Ge thin film/Si substrate further indicated autocatalytic behavior of Au deposition.

To study the thermal evolution of naoparticles on semiconductor surfaces copper nanoparticles were deposited by GDR on Si substrate. To prepare Cu thin film/Si substrate, Si substrate was dipped into a solution of 5 ml $CuSO_4$ and 200 μl HF mixture. The addition of HF is to remove the water insoluble SiO_2, which is produced during the deposition. The reaction is described in the following way,

$$2Cu^{2+} + Si + 6F^- = 2Cu + SiF_6^{2-}$$

In presence of HF, SiF_6^{2-} is produced, which is water soluble and hence reaction proceeds uninterruptedly. Formation of Cu nasnoparticles on Si surface has been observed by the plan-view TEM image (figure 2(a)) and cross sectional TEM image (figure 2(d)). Now this Cu nanoparticles contained Si substrate is annealed in a rapid thermal annealing (RTA) unit at 500^oC for 1 minutes in O_2 environment (2(b) and 2(e)). The phase of the as deposited and annealed samples are analyzed

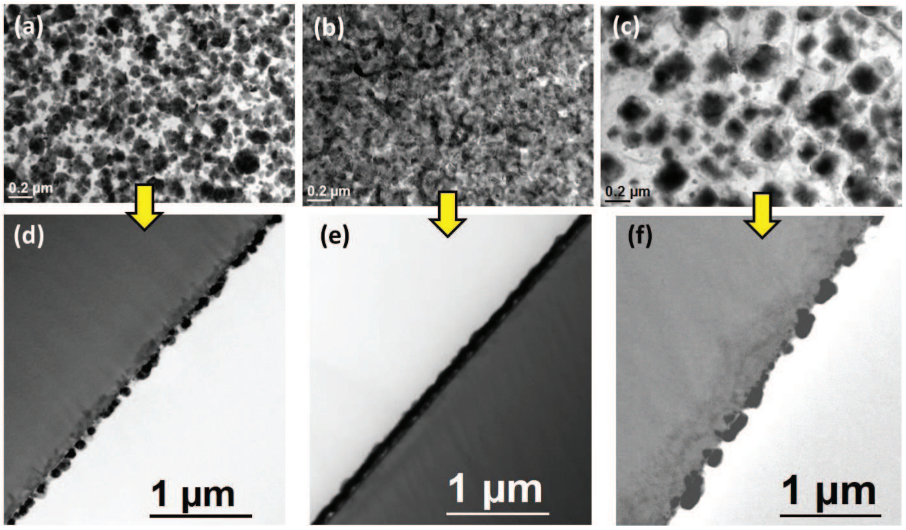

Figure 2: *Plan-view TEM images (a) as-deposited copper nanoparticles on Si substrate, (b) when the particle substrate annealed at* O_2 *atmospheric condition and (c) when annealed at* N_2 *atmospheric condition. (e),(f) and (g) are the cross sectional view of (a), (b) and (c) respectively.*

by selected area electron diffraction (SAED). In the SAED pattern of the as deposited Cu nanoparticles on Si surface (figure 3(a)), the bright spots are indexed as crystalline Si along the [100] zone axis and the faint ring patterns correspond to cubic Cu structure along with presence of Cu_2O. But when the same sample was annealed at O_2 atmospheric condition, appearance of monoclinic CuO in addition to Cu_2O is observed (figure 3(b)). The TEM imaging (figure 2(a), 2(b), 2(d) and 2(e)) revealed that, when the Cu nanoparticles on Si surface are annealed at O_2 atmospheric condition, the particles are wetting on the Si surfaces though in general thermal annealing leads to agglomeration because of Gibb's energy minimization principle. Again the same sample annealed at N_2 atmospheric condition leads to particle enlargement. So the lattice transformation as well as the surface energy modification during the CuO formation by the thermal oxidation of Cu nanoparticles on the silicon surface at O_2 atmosphere leads to the wetting that implies a strong interaction between the CuO and Si interface. Annealing of Ag nanoparticles in N_2 ambience produces perfectly round shaped particles from the as-deposited irregular shaped particles.

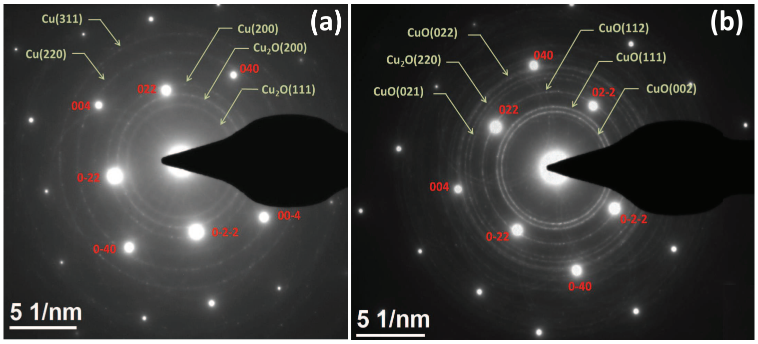

Figure 3: *SAED pattern of (a) as-deposited copper nanoparticles on the silicon substrate (b) the same sample annealed at* 500^oC *in* O_2 *atmospheric condition. The bright spot (indexed in red) are from single crystal silicon and the ring patterns (indexed in green) are from polycrystalline Cu,* Cu_2O *or CuO*

In conclusion, in this thesis work, we have demonstrated a cost effective and controlled way of producing noble metal nanoparticles on semiconductor surfaces at different atmospheric condition using versatile GDR. Occurrence of electrochemical Ostwald ripening during GDR was established in a suitably designed experiment. We have shown that by controlling defects in substrates during amorphization one can control nanoparticle growth on such substrates in GDR. Finally, the combination of GDR and RTA at different atmospheric condition can offer the control in size and shape of deposited nanoparticles on semiconductor surfaces.

Bibliography

[1] M. Kidwai, S. Bhardwaj, Appl. Catal. A **387**, 1 (2010)

[2] Y. W. Jun, J. S. Choi, J. Cheon Angew. Chem. Int. Ed. **45**, 3414 (2006)

[3] M. Baia, F. Toderas, L. Baia, J. Popp, S. Astilean, Chem. Phys. Lett. **422** 127 (2006).

[4] L. Magagnin, R. Maboudian and C. Carraro, Electrochem. Solid-State Lett. **4**, C5 (2001).

[5] S. Eustis, M. A. El-Sayed, Chem. Soc. Rev. **35**, 209 (2006)

[6] N. R. Jana, L. Gearheart, Catherine J. Murphy, J. Phys. Chem. B **105**, 4065 (2001).

[7] Y. Wang, D. Wan, S. Xie, X. Xia, C. Z. Huang, Y. Xia, ACS Nano **7**, 4586 (2013).

[8] Y. Sun, Y. Xia, Science **298**, 2176 (2002).

[9] T. Ghosh, B. Satpat, J. Phys. Chem. C **117**, 1082 (2013).

[10] Y. Liu, W. Zi, S. Liu, B. Yan, Sol. Energy Mater. Sol. Cells. **140**, 180 (2015).

[11] P. K. Jain, X. Huang, I. H. El-Sayed, M. A. El-Sayed, Plasmonics **2**, 107 (2007).

[12] M. Baia, F. Toderas, L. Baia, J. Popp, S. Astilean, Chem. Phys. Lett. **422**, 127 (2006).

[13] Z. Yuan, N. H. Dryden, J. J. Vittal, R. J. Puddephatt, Chem. Mater. **7** , 1696 (1995).

[14] L. S. Kibis, A. I. Stadnichenko, E. M. Pajetnov, S. V. Koscheev, V. I. Zaykovskii, A. I. Boronin, Appl. Surf. Sci. **257**, 404 (2010)

[15] R. J. Narayan, Diamond Relat. Mater. **14**, 1319 (2005).

[16] C. Carraro, R. Maboudian, L. Magagnin, Surf. Sci. Rep. **62**, 499 (2007).

[17] R. Liu, A. Sen, Chem. Mater. **24**, 48 (2012).

[18] T. Ghosh, P. Das, T. K. Chini, T. Ghosh, B. Satpati, Phys.Chem.Chem.Phys., **16**, 16730 (2014).

[19] V. Sivakov, G. Andr, A. Gawlik, A. Berger, J. Plentz, F. Falk, S. H. Christiansen, Nano Lett. **9**, 1549 (2009)

List of Figures

Chapter 1

General Introduction

In this chapter a brief discussion about the inspiration of the thesis work and its outlook has been presented.

1.1 Introduction

In attaining knowledge of our very own universe, we, the human being, have roamed our thoughts in the length scale of Plank length to light year. Adding a drop into the ocean, in this present thesis work, restriction has been imposed in the nanometer length region . The physical mechanism of an electrochemical nanostructure deposition process, namely galvanic displacement reaction and thermal evolution of nanoparticles on substrate surface are the main objects of this thesis work. Before stepping out for the presentation of the thesis work here we discuss few prerequisite concepts.

1.1.1 Aspects of nanomaterials

According to the definition of nanometer as thousand-millionth of a meter, in this dimension a few number of atoms can be fitted and such a collection of atoms is termed as nanoparticles. Thus nanoparticles are in the size range between molecular and bulk solid-state structure. Richard W. Siegel has classified nanomaterials into four types, viz. zero, one, two and three dimensional [1]. Sphere, clusters are 0D nanostructures, wire, fibre are the 1D nanostructures, films, plate, networks are 2D nanostructures and faceted and other come into the 3D nanostructures. In nature the existence of nanoparticles is from the very beginning as existence of nanoparticles is evidenced in the interstellar dust. The interstellar extended red emission is consequence of nanoparticle excitation. Such extended red emission, blue luminescence mainly arise from the carbonaceous and silicon nanoparticles [2]. The earth's atmosphere is a sea of floated particles where the 99% of the particles are in the size range of 1-300 nm [3]. The sources of the atmospheric nanoparticles are desert surfaces from where the air current lifts the mineral dust and anthropogenic pollutants, volcanic eruption etc. The existence of the nanoparticle in the volcanic eruption is given by a good example of eruption of Krakatoa in 1883, where optical effect appeared in the ionosphere and the global temperature was decreased by 1.2^oC in the next two year, as the nanoparticles acted as a solar radiation filter [4]. The human contribution of pollutant nanoparticle into the atmosphere is also very much countable which is evidenced by the occurrence of smog in the different big cities in world in recent time. The application of nanoparticles started long ago in the bronze age, when copper nanoparticles were introduced in the top layer of glass in the reducing condition that makes the glass colorful [5]. At that time such implementation of nanoparticles was a fluke, with-out having any idea or understanding about nanoparticles. It was Michael Faraday, who first prepared colloidal gold particles by reducing gold chloride in 1857 and also tried to explain the presence of gold particle in the ruby glass by comparing their optical behavior. Faraday's work remained unnoticed and 40 years later Zsigmondy introduced the seed-mediated synthesis of nanoparticles utilizing the Faraday's process [6]. First theoretical prediction of behavior of nanoparticles different from their bulk materials was originated in the Mie theory of light scattering by spherical structure in 1908. Though the Mie theory doesn't give size and shape dependent characteristic, the Gan-Mie theory and other corrected theory provide such anisotropic shape dependent characteristics. The evolution of the interstellar media containing the nanoparticles is described by theoretical modelling named, 'The Heterogeneous dust Evolution Model for Interstellar Solids', in brief THEMIS, which is also based on the Mie theory [7]. The fascinating physical properties of nanomaterials arise depending on their tiny size, high surface to volume ration and the diversity in such physical properties is added by their different isotropic and anisotropic shape. The zero dimensional nanoparticle domain where the quantum confinement of electrons and holes is occurred, is referred as quantum dot. So under this condition, the confined electrons and holes can be treated as 'particle in a box problem'. The optical and electronic properties of semiconductor nanoparticles are modified because of such quantum confinement effect, where the same set of properties of the bulk material are determined by their electronic structure [8]. The nanoparticle of magnetic material shows supermagnetic behavior as the nanoparticle becomes single magnetic domain [9].

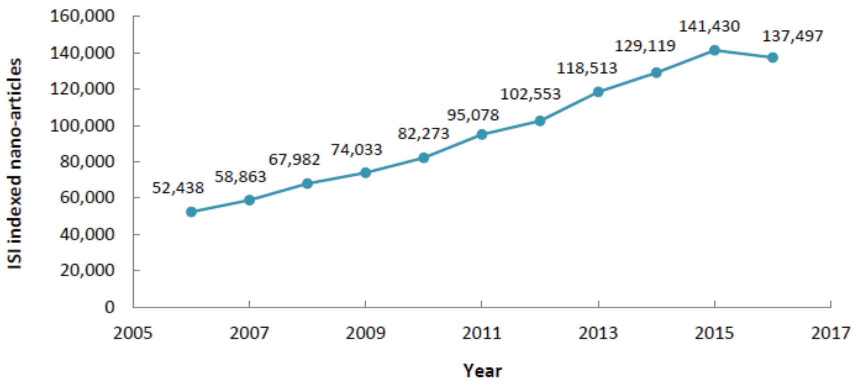

Figure 1.1: *Growth of nano-publication.*

Supermagnetic state makes the particle to posses a large magnetic moment to offer a fast response to the applied magnetic field as the nanoparticle act like a giant paramagnetic atom. The supermagnetism of the magnetic nanoparticle also includes very negligible remanence and coercivity. Now the building block of living organisms, cell is 10 μ across but the size of proteins is only few nanometer. As the size of the nanomaterials are comparable with the proteins, in the early 50s consideration of nanoparticles for targeted drug delivery was expounded. Combining all these successive progresses of nanomaterials, in the past few decades a interdisciplinary subject of physical, chemical and biological sciences, the nanotechnology has been established. If we look at the existence of the nanoparticles in the interstellar dust, the analysis of the nanoparticles provide information about the galaxy. Study of the nanoparticles in the pollutant air is important to take care of environment and human health. The fascinating feature of the nanomaterials has been propagated to electronic, optical, medical devise fabrication to make our daily life more feasible and prosperous. In this way the nanomaterial has become a part of our better future which is reflected in the progression of the worldwide nanoscience publication as presented in Figure 1.1 [10]. In this thesis work, the deposition of nanoparticles on semiconductor surface, using an eco-friendly technique and investigation for the evolution of the structural properties of nanoparticles at elevated temperature have been elucidated.

1.1.2 Probing nano-object

Different novel techniques have been improvised to study nanomaterials because of their tiny size and different physical properties. The structural property evaluation of nanomaterials is not possible to deal with normal optical microscope as its resolution is limited by the light wavelength. A modified ultramicroscope that uses light scattering provides better visualization of nanoparticles with bigger size. Near-field scanning optical microscopy (NSOM) can also produce spacial resolution of 50-100 nm, where higher resolution is obtained by using an aperture of diameter less than the wavelength of the optical source.

The light microscopy is direct measurement process of the nanoparticle size and shape. In this context, spectroscopy is an indirect measurement procedure to perceive nanomaterial size and shape. In UV-visible spectroscopy absorbance or transmittance is measured as a function of incident electromagnetic wave length. The light with continuously changing wavelength is impinged on the specimen and the reflected or transmitted wave is detected, at the same time, as a reference, a non-interacted wave is also collected by the detector. When incident wavelength matches the gap of the electron energy level in the specimen, then the electron is shifted to a higher molecular energy level, so energy is absorbed. Comparison of the intensity between the incident wave and the reflected or transmitted wave provides absorbance. In case of nanoparticles, surface plasmon resonance plays an important role on the absorbance spectra. The size, shape and element of the nanoparticle define the absorbance spectra. UV-visible spectroscopy in this way can give a rough estimation about the size and shape of the nanoparticles. The Raman spectroscopy is also an important technique to characterize nanomaterial. Raman effect is an inelastic light scattering with matter, where the emitted photon may have lower or higher frequency than the incident light, called the Stokes and anti Stokes line consecutively. The raman spectroscopy can be used for the phase identification of nanomaterials and using the phonon confinement model (PCM) raman spectroscopy can be implemented in size determination of nanoparticles. The surface enhanced raman spectroscopy (SERS) is also an effective way for understanding nanoparticle properties.

Since light microscopy is lame in providing enough resolution and to give information about small nanoparticles, probing microscopy comes with sub-nanometer resolution to give the information even about the constituents of nanomaterial. The scanning tunneling microscopy is a powerful probing tool with atomic level resolution which is based on the concept of quantum tunneling. If a sharp probing tip is brought very closer to the surface of metal or semiconducting specimen and a voltage is applied between the probe and the specimen, then electrons from the specimen can tunnel through the vacuum to the probe. When a low voltage is applied, this tunnelling current is a function of density of state at the fermi level of the specimen. Moving the probe over the specimen, the tunnelling current variation is obtained and transformed into image that provides an atomic level resolution. As a probing technique, the quality of atomic force microscopy (AFM) is that it is an non-destructive technique to study specimen surface in nanometer scale. Measuring the van der Waal and other physical forces between the probe and the specimen, a three dimensional information of a specimen surface is constructed.

Electron microscopy is a powerful tool for nanomaterial characterization. Providing accurate size and shape information with sub-nanometer resolution, crystallographic orientation, elemental differentiation, phase identification of a specimen within a short interval of time, the electron microscopy becomes a superior technique among the other candidates. In scanning electron microscopy (SEM) a high energetic electron beam is scanned over the specimen surface and the generated secondary electrons, back-scattered electrons, characteristic x-ray are collected to get the topographic and compositional information. On the other hand in transmission electron microscope a high energetic electron beam is transmitted through the specimen and the transmitted and other signals are accumulated to get the different specimen information at a time. In the thesis work, along with the TEM, SEM and AFM have been utilized, so we will discuss their operations in details.

1.1.3 Substrate supported nanoparticles

As we discussed, the first synthesis process of nanoparticle was a colloidal protocol. The nanoparticles in colloidal state show potential application in various fields such as chemical sensing, drug delivery. Main advantages of the liquid phase synthesis are the stabilization, size and shape control, conjugate particle synthesis etc. The fascinating electric and magnetic properties make the nanoparticle potential candidate for electronic, sensing and many other solid state device fabrication. Now, the colloidal nanoparticle is suitable for protein encapsulation, targeted drug delivery or other application, but for the solid state device, nanoparticles have to be assembled avoiding the solution form. Incorporation of substrate with nanoparticles also makes impacts to arise new physical properties. For instance, substrate induced strain may influence the transport and magnetic properties of the nanomaterial when deposited on substrate [11]. Similarly, electric field enhancement of metal nanoparticles in electromagnetic wave incidence is affected by the electromagnetic field coupling between the nanoparticles and their supporting substrate as the experimental and theoretical study show that noble metal/Ge substrate has better field enhancement than noble metal/Si substrate [12]. One way to assemble the nanoparticle on solid surface is initially the nanoparticles be synthesised in solution form then they are applied on the substrate by spraying the nanoparticles onto the substrate surface or by immersing the substrate into the nanoparticle solution [13, 14]. Good uniformity of particle deposition is challenging to achieve in these ways. Adhesion of nanoparticles to the substrate surface is also questionable in these processes. Another way is the centrifuge sedimentation process. In this process the substrate is placed into the nanoparticle solution and they are centrifuged at suitable rpm to attach the nanoparticles on the substrate from the solution. Spin coating is also a similar process that uses centrifugal force but here concentrated colloidal nanoparticle drop is placed on the substrate surface and then substrate is rotated at high speed to spread the nanoparticles [15]. The sedimentation process gives a better substrate adhesion whereas the spin coating provides better particle uniformity. Gas phase deposition of nanoparticles is a convenient technique in terms of substrate adhesion, cluster formation and precise particle size control. Few such gas phase depositions are physical vapor deposition (PVD), chemical vapor deposition (CVD), pulsed laser deposition (PLD), sputtering etc [16–18]. Main drawbacks of these depositions is that high vacuum is to be maintained which needs extra effort and expense. As the colloidal synthesis soon came up with formation of different faceted and three dimensional nanomaterials and their applications was proved to be marvellous, assembling of such facetted and different shaped three dimensional nano-objects emerged as an essential part of the substrate supported nanoparticles. Now the gas phase deposition of nanoparticle is incapable of producing such faceted and different shaped three dimensional nanoparticles. In this thesis work the galvanic displacement deposition technique has been utilized that fulfill few such fundamental deficiencies of nanoparticle deposition.

1.1.4 Galvanic displacement reaction (GDR)

GDR is established for versatile applicability [19–21]. In the discussion of the thesis work detail mechanism of GDR has been elaborated. Here few interesting behaviors of the GDR are depicted.

1.1.4.1 Selectivity

Two or more different element nanoparticle deposition on substrate is an attractive way to explore different new application of nanoparticle-substrate conjugate. An example can be cited as the more uniform SERS signal has been obtained for Ag-Au nanoparticles assembly on Ge substrate in comparison to only Ag nanoparticles grafted on Ge [22]. For the conventional PVD, CVD, PLD or sputtering, they have limitation for deposition of distinct clusters with different elements as the later elements overlap the first element as depicted in Figure 1.2(a). Hence the effect of the multiple nanoparticles with different elements is missed. Here the GDR differs from other techniques due to its selective deposition. Since the GDR depends on the electrode potential difference between two elements, if a third element doesn't satisfy the deposition criterion with any of the previous two elements then it can not affect the reacted elements. As depicted in Figure 1.2(b), two

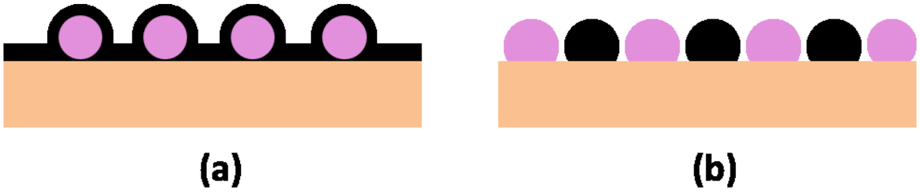

Figure 1.2: *Multi-element deposition by (a) conventional gas phase deposition (b) galvanic displacement reaction*

different elements (marked by pink and black) can be deposited on a substrate by GDR. The deposited elements don't have suitable redox potential of GDR between them, so the later element can be deposited in the vicinity of the first deposited nanoparticles with out disturbing them.

1.1.4.2 Substrate adhesion

For a substrate supported nanoparticle system and its applicaiton, the adhesion between the nanoparticles and substrate surface always comes under special consideration. In a conventional evaporation technique the substrate adhesion can be improved by raising the substrate temperature during the deposition. At room temperature, the substrate adhesion in GDR may be comparable with the evaporation technique up to some extent [23]. In GDR, substrate heating is forbidden as the deposition is conducted in a solution bath but substrate adhesion in GDR arises in different ways. The substrate adhesion in GDR can be increased by adhesion-promoting additives. For instance, the adhesion of copper film on silicon substrate is improved by the presence of ascorbic acid or sodium sulfite and maximum adhesion was obtained by the ascorbic acid presence [24]. The other way is chemical bond formation that assists substrate adhesion in GDR. For instance, Magagnin et al [25] has observed that the bond formation at the Au-Ge interface in galvanic displacement of Au on Ge substrate creates a better substrate adhesion.

1.1.4.3 Three dimensional nanostructure growth on substrate surface

The substrate supported three dimensional faceted nanostructures with interesting physical properties provide scopes of different applications. Now the gas phase deposition or lithography techniques are not suitable techniques for faceted three dimensional nanostructure growth on substrate surface. A two step process of embedding seed nanoparticles on substrate surface and then growth of three dimensional structure on the seed particle can be employed. As Mieszawska et el synthesised Au nanorods on SiO_2/Si substrate by microprinting Au nanoparticle seeds [26]. For microprinting SiO_2/Si substrate was coated with 3-mercaptopropyl trimethoxysilane (MPTMS) and Poly dimethylsiloxane(PDMS) stamp was dipped into Au nanoparticle solution to adhere the nanoparticles, then the PDMS was stamped on the SiO_2/Si surface. In this context the GDR is an easier and versatile technique to obtain three dimensional nanostructure on substrate surface. Improvising GDR, icosahedra, triangular and hexagonal plates have been grown on InP surface. Silver hexagonal plates, nanoinukshuks and dendritic structures on Ge surface can olso be obtained by GDR [27]. Thus GDR is proved to be simple one step process to obtain such three dimensional nanostructures on different substrate surfaces.

1.1.5 Thermal behavior of substrate supported nanoparticles

Thermal annealing of nanomaterials is an inseparable part of the nanoscience. Thermal annealing may be implemented to obtain elongated nanostructure from a flat particle distribution on substrate surface or to improve the adhesion of deposited nanomaterials with the substrate surface [23]. Residual oxide may be decomposed at elevated temperature that helps to get the actual metal nanoparticle properties [28]. Thermal annealing can also lead to phase separation of bimetallic nanoparticle assemblies [29]. To understand the structural reconstruction of nanomaterial at raising temperature the following points are needed to be considered.

1.1.5.1 Surface energy, contact angle and wetting-dewetting

At thermodynamic equilibrium, the energetic of solid-liquid-gas interface can be described by Young's equation as

$$\sigma_{SG} = \sigma_{SL} + \sigma_{LG} \cos\theta \tag{1.1}$$

where, σ_{SG} is the solid-gas interface energy, σ_{SL} is the solid-liquid interface energy, σ_{LG} is the liquid-gas interface energy, θ is the contact angle that the liquid-gas interface makes with the solid, measured through the liquid. If θ is less than 90^o then the solid surface is said to be hydrophilic and if θ is greater than 90^o then the solid surface is said to be hydrophobic (Figure 1.3). If θ is more than 150^o then the solid surface is called super hydrophobic. If we consider a liquid drop is placed on a solid surface then, it is easier to describe the thermal equilibrium by the Young's equation, as we can easily equate the physical force balance. If external energy is given in the system then the equilibrium can not be simply described by the Young's equation. Now in our work we are interested about the thermal evolution nanoparticles, a collection of atoms, supported on a substrate. The external thermal energy input into the system generally makes the particle more spherical to minimize the surface free energy [30], as a result the contact angle is increased. Instead of agglomeration, the particles may also spread on

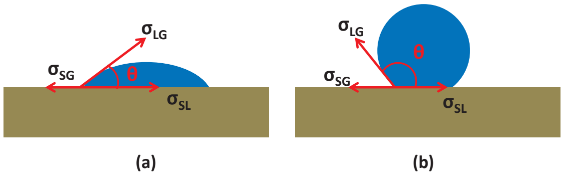

Figure 1.3: *contact angle for (a) hydrophilic surface, (b) hydrophobic surface*

the supported substrate, if irreversible reaction occurs to form interfacial product [31]. This type of wetting is called chemical wetting. It may occur in different mechanism process. For example, the particle may reduce the substrate element at the interface that lead the wetting [31, 32]. Such wetting is called displacement or redox wetting. The particle and the substrate may dissolve to form a reaction product at interface. This dissolution at the interface bring the wetting. This type of wetting is called solution reaction wetting. If we compare between the displacement and solution reaction, the later has better spreading. In this context the thermodynamic work of adhesion represent the wetting, which is defined as,

$$W = \sigma_{SG} + \sigma_{LG} - \sigma_{SL} \tag{1.2}$$

so the work of adhesion can be written as

$$W = \sigma_{LG}(1 + \cos\theta) \tag{1.3}$$

Negative value of W, refers to the wetting [33]. Because of irreversible reaction and interfacial product formation as described earlier in terms of displacement or solution reaction, more energy is gained and the consequence is more more negative value of work of adhesion and occurrence of wetting. Yu et al [33] observed the wetting of Pt nanorystal on silica surface and Baldwin et al [31] observed wetting of copper alloy on alumina surface. In both of their work the, the intermixing between the particle and substrate occurred, giving rise to a negative work of adhesion. This is clearly a solution reaction wetting process. Again Ti may reduce Al_2O_3 substrate [31], producing a negative work of adhesion and wetting as consequence, which is a displacement or redox wetting process.

1.1.5.2 Thermal annealing and particle enlargement

Negative work of adhesion in thermal annealing of nanoparticles on substrate leads to wetting of the nanoparticles but more thermodynamically favorable process is dewetting of the particles. Another important phenomenon, Ostwald ripening, arises in the thermal annealing of nanoparticles on substrate surface. The ostwald ripening makes the formation of larger particle by dissolution of small particle and hence the particle arrangement is redistributed. Wilhelm Ostwald first described such particle enlargement at the cost of small particles in 1896 [34, 35]. The Ostwald ripening is based on the energy minimization principle. Ostwald ripening may occur in different systems such as supersaturated solution [36], cellular structure [37], gas-liquid foam [38]. Ostwald ripening may also occur in the substrate supported nanoparticles. The particle transport may occur by surface diffusion, diffusion through substrate and diffusion through the vapor phase (Figure 1.4). The surface diffusion process is dominant among the three processes.

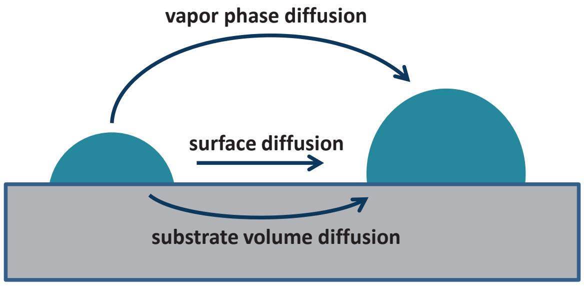

Figure 1.4: *diffusion processes in thermally activated Ostwald ripening*

The chemical potential is a function of radius of curvature of a particle and it is given by the Gibbs-Thomson relationship as [39],

$$\mu = \mu_0 + \frac{2\gamma V}{r} \tag{1.4}$$

where, μ_0 is the chemical potential of infinite size particle, V is the atomic volume, and r is the radius of curvature of the particle. From the Gibbs-Thomson equation, we see that larger particle has lower chemical potential and smaller particle has greater chemical potential, which implies that the adatoms will easily diffuse from the smaller particles to the bigger particles. Hence the bigger particles will be enlarged at dissipation of the smaller particles. The growing particle may also form facets. Such facet formation is called inhibited particle growth and accomplished by nucleation. The non-inhibited particle growth by the Ostwald ripening was first elaborately described by Chakraverty by the equation [39, 40],

$$\frac{r}{r_0} = 1 + \frac{Kt}{r_0^n} \tag{1.5}$$

Where, r_0 and r are the average radii of curvature of the particles at time $t = 0$ and at time $t = t$, K is a mechanism dependent constant, n is an integer with value in the range $2 - 4$, depending on the rate of the growth. The above equation fails to explain some experimental result. Later the corrected explanation was given by Wynblatt et al [39] as follows,

$$(\frac{r^*}{r_0^*})^4 = 1 + \frac{27A_d t}{64(r_0^*)^4} \tag{1.6}$$

Where, A_d is a temperature dependent function, $r^* = 0.97r$, and r_0^* is the value of r^* at time $t = 0$.

Previously we saw that depending on the surface energy the nanoparticles may get wetted on the substrate surface and here we notice that thermal annealing induced surface diffusion may lead to agglomeration and particle enlargement. In the the thesis work both such phenomena are witnessed and discussed in the thermal evolution of nanoparticles on substrate surface.

1.2 Outline of the thesis

The convenient implementation of galvanic displacement deposition in many directions makes it a potential candidate for assembling nanostructure on solid surfaces. Due to the fast occurrence of the charge exchange between the oxidizing and reducing species, turns the control in achieving desired thickness in the GDR is a challenging job [41]. Where our study in identification of Ostwald ripening in the GDR by the assistance of defect induced substrate provides an insight and as well as control achieving in GDR. Again the thermal treatment is a precious tool for the structural transformation of nanomaterials on substrate surface. The combination of the galvaic displacement reaction and thermal treatment has also been considered in the present thesis work. The complete work has been described arranging them into different chapters are as follows

Chapter 2 represents different experimental technics that have been utilized for completion of the work. The basic principle of electron microscopy, its many fold application and comparison between the SEM and TEM have been eleborated. The operation of AFM and RTA system also have been elucidated.

Chapter 3 describes the primary aspects of GDR. The mechanism, application and the diversity of the GDR are discussed in progression.

Chapter 4 demonstrates the insight of the GDR. The detail study of Ag nanoparticle deposition on ion bombareded amorphized Ge substrate incorporating the the description of electrochemical Ostwald ripening, surface diffusion and control achieving in particle growth has been presented. Again substrate decomposition, the consequence of GDR has been narrated by observing the Ge film decomposition by Ag and Au partcle deposition.

Chapter 5 deals with the thermal evolution of nanoparticles on substrate surface. The role of oxygen in wetting of Cu nanoparticles on Si surface at elevated temperature has been explored. The GDR and RTA have been conjugated to produce well separated Ag nanoparticle arrangment on Si surface.

Finally in **Chapter 6** conclusion has been drawn.

Chapter 2

Experimental methods

This chapter describes different experimental methods that have been used for the study of the GDR and thermal evolution of nanoparticles on substrate surface. The description are mainly the basic operation of TEM, SEM, AFM, XRD, RTA etc.

2.1 Introduction

To study the GDR of metal nanoparticles on semiconductor surfaces in great details, we have utilized different experimental techniques. We have used the transmission electron microscope intensely as one of the main technique. Nanoparticles shape and size have been observed by the TEM imaging; the crystal structure and the interface properties have been inspected by high resolution imaging (HRTEM) and electron diffraction; elemental identification has been carried out by STEM-HAADF technique and the energy dispersive X-ray spectroscopy (EDX) attached with the TEM. For the microscopic size distribution of the nanoparticles in wider range, scanning electron microscope(SEM) and atomic force microscope (AFM) have been used. Thermal treatment of nanoparticles on semiconductor substrate has been done using a rapid thermal annealing (RTA) system. For the phase identification of the as deposited and the annealed nanoparticles on the substrate surface, X-Ray diffraction (XRD) also has been performed.

2.2 Transmission Electron Microscopy (TEM)

After Louis de Broglie introduced the wave nature of particle in 1925 , the idea was adopted in no time to use electrons for the microscopy imaging and in 1933 Ruska and Knoll built the first electron microscope. Ruska won the noble prize for his contribution in electron microscopy. The later development made the transmission electron microscope with different attachment, one of the best tool to analysis material in nanometer and sub-nanometer scale along with structural and elemental details. In a transmission electron microscope, when electrons impinge on a specimen, several secondary signals are produced. From these secondary signals, apart from the imaging with far better resolution than optical microscope, different analytical information can be obtained. The occurrence of electron diffraction and high resolution imaging provides the crystallographic information. Measuring the loss of energy of the electron after it passes through the specimen, the chemical and plasmonic properties can be obtained. Again the X-rays produced from the specimen due to the incident of the high energetic electron provides elemental identification. All these make the transmission electron microscopy a nano research laboratory.

2.2.1 Brief comparison with the light microscopy

The need of a microscope is unavoidable as the man eye is limited with the resolution with $0.1 - 0.2$ mm. That is the human eye cannot distinguish between two points closer than this distance. The light microscope with the glass lens was invented in the seventeenth century. Till date different compound light microscope are available with good resolution but the resolution of the light microscope is constrained on the wavelength of the illuminating light. The wavelength dependent resolution of the light microscope is given by

$$\delta = \frac{0.61\lambda}{\mu \sin\beta} \tag{2.1}$$

Where μ is the refractive index of the viewing medium, β is the semi angle of the magnifying lens and λ is the wavelength of the incident light. The wavelength of the visible light lies in the range $400 - 700$ nm. So from the above equation the maximum resolution of a light microscope is around $200 - 300$ nm. Here comes the transmission electron microscope that offers higher resolution than the optical microscope. By increasing the operating voltage of a transmission electron microscope, the resolution can be reached up to subnanometer range. The magnifying power of a microscope depends on the lens system of the microscope. In both the light and the electron microscope, collection of lenses are used but there is a huge difference between the lens system used in optical and electron microscope. Glass lenses are used in optical microscope but magnetic lenses are used in transmission electron microscope. The basic principle of a magnetic lens lies on the fact that application of magnetic field changes the direction of the electron beam. Since, unlike the light in optical lens, in magnetic lens the electron cannot be passed through material other than specimen, because it will interact with it and will not give the actual images and other information, so the structure of a magnetic lens is completely different from that of an optical lens. A magnetic lens (Figure 2.1(a))

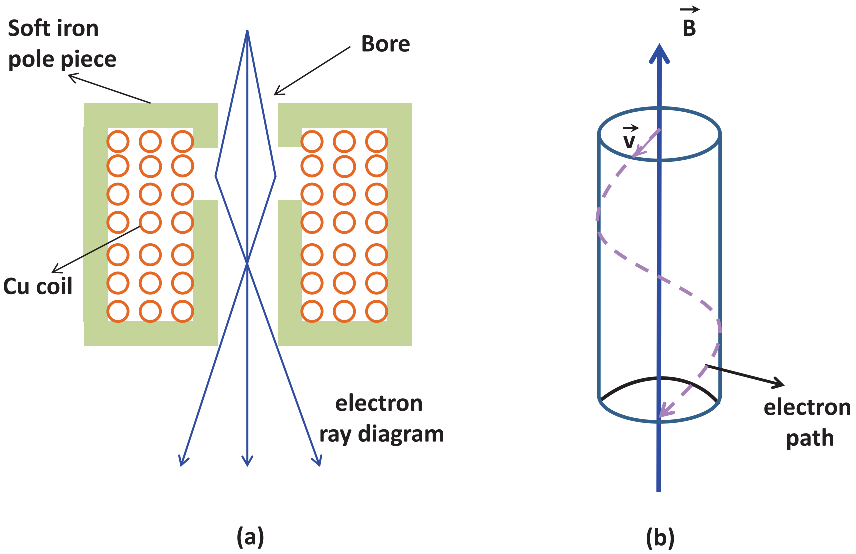

Figure 2.1: *(a) Magnetic lens, (b) Path of electron in a magnetic lens.*

mainly contains two parts, a cylindrically symmetrical core of soft magnetic material (like soft iron), which is called pole piece and a hole drilled through it, which is called the bore of the pole piece. There are copper coil that surrounds the pole pieces. Passing current through the coil produces magnetic field that controls the trajectory of the electron beam. Due to the resistive heating in the copper coil, cooling of the lens is required. Most of the time we represent the electron path in TEM by ray diagram but when the electron passes through the electromagnetic lens, it doesn't follow the straight line path at all. When the electron traverses through magnetic field of the magnetic lens, the force experienced by the electron is given by the Lorentz force

$$\vec{F} = -e\vec{v} \times \vec{B} \tag{2.2}$$

where $\vec{B}$ is the magnetic field and $\vec{v}$ is the velocity of the electron. Solving the above force equation it can be shown that the electron moves in a helical path (Figure 2.1(b)), where the radius 'r' and the cyclotron frequency 'ω' are given by

$$r = \frac{mv}{eB} \quad \text{and} \quad \omega = \frac{eB}{m} \tag{2.3}$$

The above description is a preliminary one, the actual path of the electron is far complex, where many influences and many number of electrons have to be considered.

2.2.2 Electron interaction with matter

When a moving electron impinges on a specimen the following phenomenon may arise. The electron can make a head on collision with the nucleus of the atom of the specimen and scattered back in the opposite direction, so called the back scattering;

it can have elastic or inelastic collision and transmit through the specimen, or it can transmit without any interaction, so called the direct beam or the electron can lose all of its energy and comes to rest, eventually absorbed by the matter. Now when the electron loses some energy to the specimen atom the following signal may be generated (Figure 2.2).

Secondary electron: If the speedy electron supplies sufficient amount of energy to the shell electrons to cross over the work function, they are simply knocked out. These electrons are called secondary electron. These electrons are considered for the scanning electron microscopy.

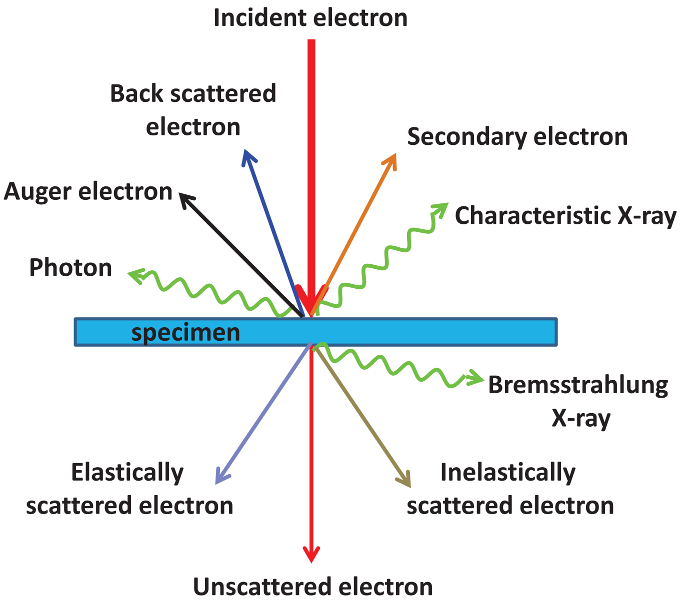

Figure 2.2: *Schematic for the electron interaction with matter.*

Characteristic X-ray and Auger electron: Due to the gain of energy from the incident electron the inner shell electron can be promoted to the lowest unoccupied electron level or can be knocked out of the atom. Then upper shell electron jumps to fill the vacancy which is energetically favourable. When the electron jumps from the higher energy level to the lower energy level the energy difference between the levels is released in the form of X-ray which is the elemental characteristic. Again this liberated energy can knock out another electron too, which are called the auger electrons.

Bremsstrahlung X-ray: When an electron passes through the electron cloud of the specimen atom it can lose energy due to the coulomb interaction with the atomic nucleus. This absorbed energy is released as electromagnetic radiation having any amount of energy with the limit of the incident electron energy. This radiation is named as the Bremsstrahlung X-ray.

2.2.3 Different component of TEM

The TEM is a quite big instrument with different attachments. The structural description of TEM can be made by classifying it into three basic component, namely the illuminating system, specimen stage system and the imaging system.

2.2.3.1 Illuminating system

In the illuminating system, the electrons are generated from the electron gun, then they are accelerated towards the specimen by a high voltage and in between the electrons are controlled by condenser lenses.

Electron gun: There are mainly two types of electron sources which are used in transmission electron microscope, they are thermionic emission gun and the field emission gun. In a thermionic gun, the electron is pulled out by thermal energy, whereas in a field emission gun electric field is used to knock out the electron and combining both these principle a different Schottky gun is constructed.

In thermionic emission, the tip of the gun is heated sufficiently that the electrons cross the potential barrier and the current density of the emission is given by the Richards equation $J = AT^2e(-\phi/kT)$ where 'A' is the Richardsons constant (10^{-6} in SI unit), ϕ is the work function and k is the Boltzmann constant. For thermionic emission gun generally lanthanum hexaboride (LaB_6) is used. Compared to other material for the thermionic LaB_6 has low work function that makes it suitable and needed to heat it in the the temperature range 1400K-2000K. The electrons coming out from the filament, are controlled by a electrode called Wehnelt cylinder. The Wehnelt cylinder surrounds the filament and is biased more negatively than the filament. Smaller emitting areas is obtained by the negative applied voltage in the Wehnelt cylinder. Below the Wehnelt cylinder, the anode plate is placed that accelerates the electrons (Figure 2.3(a)). On the other hand for the field emission (Figure 2.3(b)), strong enough electric field is applied to the cathode tip such that electrons overcome the potential barrier. The electric field required for an electron

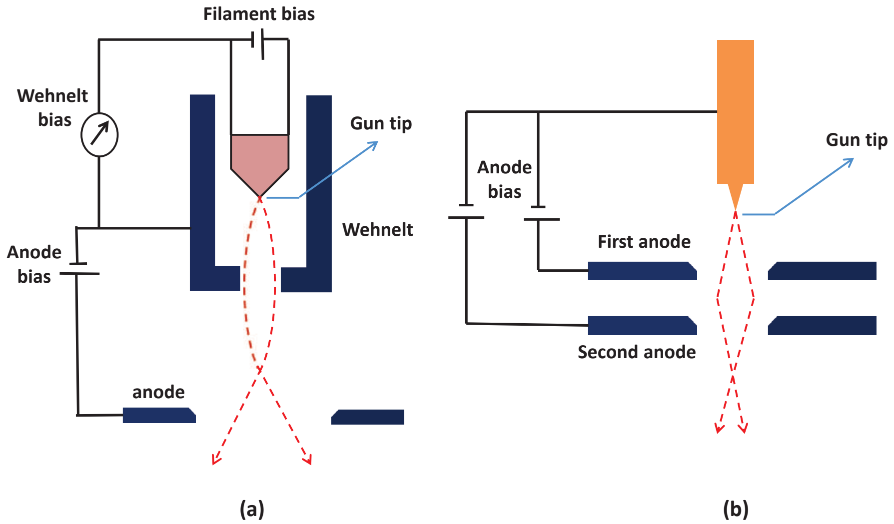

Figure 2.3: *(a)Thermionic gun, (b) field emission gun*

to jump over the potential barrier is given by E=($\phi/e\lambda$); λ (10^{-9} m) and ϕ are the de Broglie wavelength and work function, respectively. For tungsten filament (ϕ=4.5 eV) the magnitude of the electric field is $\sim 10^{-9} V/m$. Now for the applied voltage V on the cathode tip with radius of curvature ‘r’, the electric field at the cathode tip will be V/r. Typically ‘r’ is 0.1μ m, which implies that for the applied voltage of 1KV the electric field is $\sim 10^{10}$ V/m, which is lesser than the potential barrier and electrons tunnel out of the filament. Since the electrons can be emitted at room temperature with out heating the filament, the field emission referred as cold field emission. In a field emission gun, there are two anode plates, the first one extracts the electrons and the second one accelerates them. The combination of these two anodes, provides the effect of a electrostatic lens to control the electrons. In Schottky gun, the filament is heated as well as the electric field is applied. So the Schottky provides an intermediate temperature and applied electric field for gun filament and the filament tip also not needed to be too sharp.

Acceleration of the electron beam: In a electron gun, the electrons are either extracted from the filament cathode by thermal heating or by the application of electric field and after the electrons are produced, they are accelerated towards the specimen by a high electric field. The electric field is applied between the cathode filament and an anode. The anode is a metal plate with a central hole. The potential difference between the cathode and the anode accelerates the electrons and passes them through the anode hole. Roughly 1% of the emitted electrons pass through the anode hole. Till now we have considered electron as a particle, where we knocked them from the atom by external influence. When they are accelerated by high energy, we have to be concerned about its wavelength, given by the de

Broglie wavelength $\lambda = \frac{h}{p}$. If potential 'V' is applied between the cathode and the anode, then the kinetic energy of the electron is given by

$$T = \frac{p^2}{2m} = eV \tag{2.4}$$

where e and p are charge and momentum of electron respectively. So the de Broglie wave length of the electron,

$$\lambda = \frac{h}{p} = \frac{h}{\sqrt{2meV}} \tag{2.5}$$

When the accelerating voltage exceeds 100 KeV, the speed of the electron reaches 0.5c, so the relativistic effect also have to be incorporated and the corrected wavelength is given by,

$$\lambda = \frac{h}{\sqrt{2meV(1 + \frac{eV}{2mc^2})}} \tag{2.6}$$

In the transmission electron microscope we utilize both the wave and the particle nature of electron.

Condenser lens: To illuminate the required area of specimen that produces sufficient magnified image at viewing screen, before the electrons impinge on specimen, they are controlled by condenser lenses. Generally two condenser lenses are used. The first condenser lens is a strong magnetic lens with a focal length of few mm. It produces a better point source by demagnifying the virtual electron source of electron gun. This point source size can be controlled by changing the first condenser lens strength. The second condenser lens has lesser strength compared to the first condenser lens and has focal length of few cm. The second condenser lens controls the spread of the illumination to the specimen. A condenser aperture is attached with the second condenser lens, that selects the convergence of illumination.

2.2.3.2 Specimen stage system:

The specimen stage is a complicated part of the TEM, situated below the condenser lens system. The specimen is inserted without disturbing the column vacuum of the microscope. To maintain the column vacuum during inserting the specimen, special design is required for the stage. This is done by incorporating an airlock and a high vacuum system. The airlock is chamber which is evacuated before inserting the specimen holder into the TEM column and this is followed by the high vacuum operation. There are two types of stage system, they are viz, side entry and top entry stage. In a side entry stage, the specimen is inserted by a metal sample holder at its one end and the other and is connected to external power source. On the other hand, in a top entry stage, specimen is insert by a cartridge, which is placed completely and has no external connection. In our work we have used the side entry holder and a schematic for the side entry holder is given in the Figure 2.4.

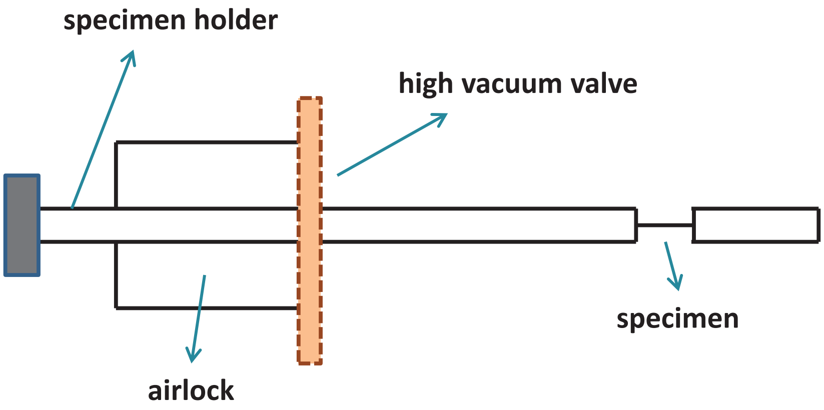

Figure 2.4: *Schematic of a side entry specimen holder*

2.2.3.3 Imaging system:

In a modern transmission electron microscope, the imaging system consists of the objective lens, intermediate lens and the projector lens. The objective lens produces a magnified real image of the specimen. It is required to keep the specimen just above the objective lens where the part of the focusing field of the objective lens acts on the electron beam and which is called the post field of the objective lens. The objective lens focuses the electron beam for the imaging, when the electron beam impinge on the specimen from the final condenser lens. The intermediate lens is a combination of several lenses which stands between the objective and the projector lens. The main function of the intermediate lens is to vary the magnification by changing its focal length gradually. A wide range of variation, typically 10^3 to 10^6 is obtained by the intermediate lens system. The final lens of the microscope column is the projector lens which constructs the image or the diffraction pattern on the screen of the transmission electron microscope which is of several centimetres diameter. The final magnification is the algebraic product of the magnification factor produced in each magnetic lens.

2.2.4 Diffraction and imaging in TEM

When the parallel beam from the condenser lens system impinges on specimen, the electron beam is diffracted at different angles. The objective lens focuses this diffracted beams at its back focal plane and also produces an image at its image plane. Now the diffraction or the image formation on the viewing screen depends on adjustment of the intermediate lens. If the intermediate lens is adjusted such that the back focal plane of the objective lens becomes its objective plane then diffraction pattern is obtained at the viewing screen (Figure 2.5(a)). When the intermediate lens is adjusted such that the image plane of the objective lens becomes its objective plane then image is obtained on the viewing screen (Figure 2.5(b)).

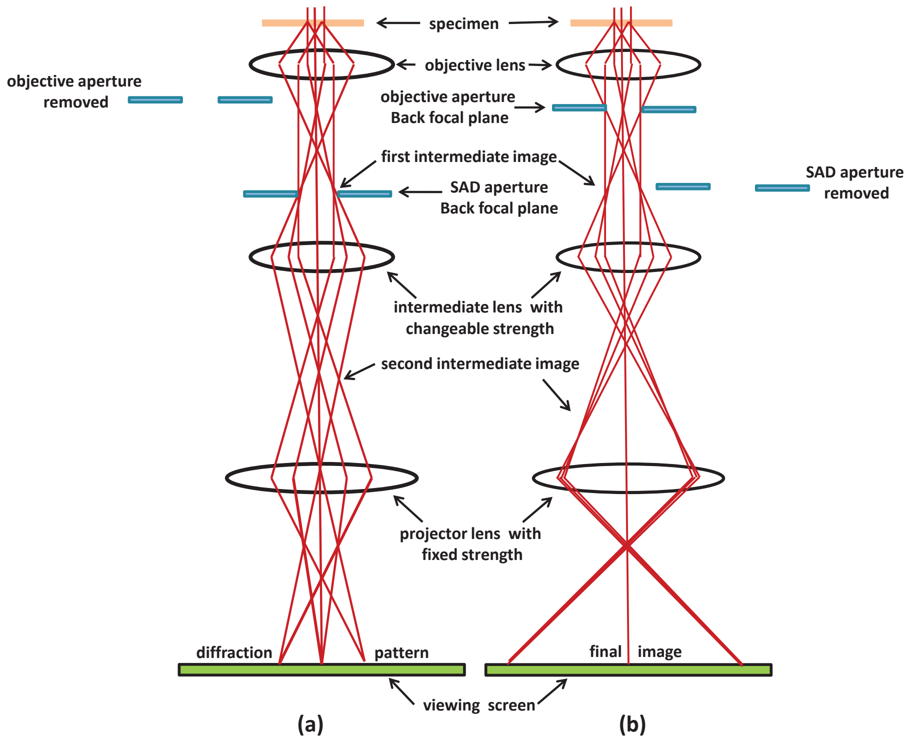

Figure 2.5: *(a) diffraction, (b) imaging*

2.2.5 Selected area electron diffraction (SAED)

The electron diffraction is a significant technique for getting the crystallographic information of a specimen. In a TEM depending on the way of the electron beam impingement, two types of electron diffraction can be obtained, they are selected area electron diffraction(SAED) and convergent beam electron diffraction(CBED). To form SAED pattern, parallel beam is to be impinged on the specimen, which is done by the condenser lens system and CBED is formed by impinging convergent beam. The CBED provide more information than the SAED. In this thesis work, we have mostly used the SAED for the phase information of nanomaterial.

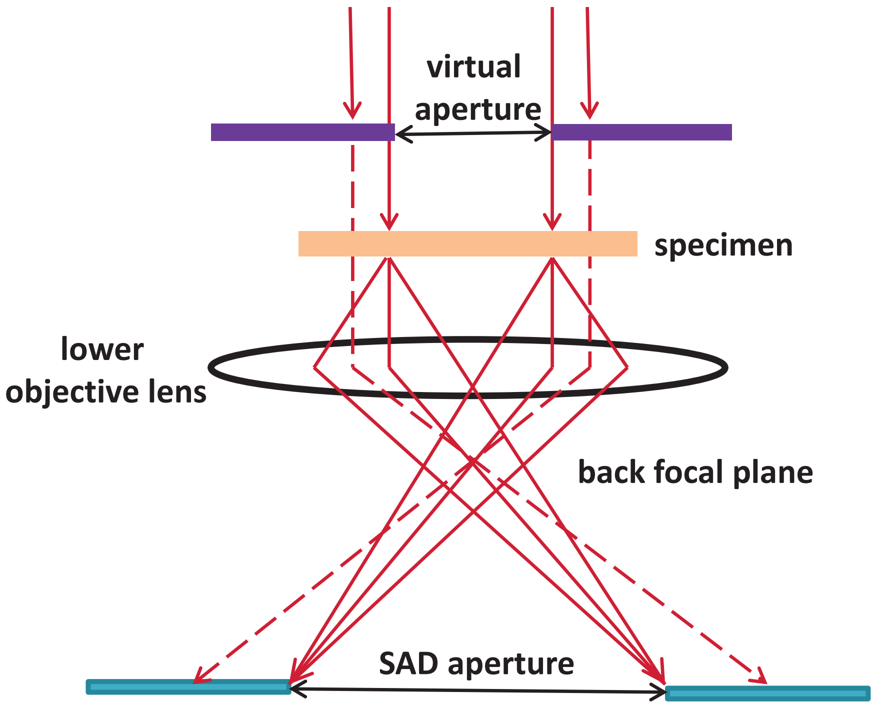

Figure 2.6: *SAD aperture and formation of virtual aperture*

The SAED operation was first invented by Le-Pool in the year 1947. In a diffraction pattern formation, it is necessary to illuminate small area of the specimen to reduce the intensity of the diffraction spots. Since we deal with the parallel beam for the SAED, it is not possible to decrease the illumination area by converging the beam. So an aperture, called selected area diffraction (SAD) aperture is used to reduce the area of the incident beam. The SAED aperture is inserted at the image plane of the lower objective lens which forms a virtual aperture above the specimen (Figure 2.6). The minimum size of the objective aperture is $\sim 10\mu$m and the virtual aperture is demagnified below 1μm. Out side this area, all the electron that impinge on the specimen, do not contribute to the final diffraction pattern. As described in Figure 2.7(a), when an incident wave front w_i impinges on a plane of atom at an angle θ, after diffraction it takes the form as indicated by the wave front W_d. If we denote the incident wave vector by $\overrightarrow{k_i}$ and the diffracted wave vector by $\overrightarrow{k_d}$ then the angle between the incident and the diffracted vector is 2θ. Now from the Figure 2.7(b), we can write,

$$\overrightarrow{k} = \overrightarrow{k_i} + \overrightarrow{k_d} \tag{2.7}$$

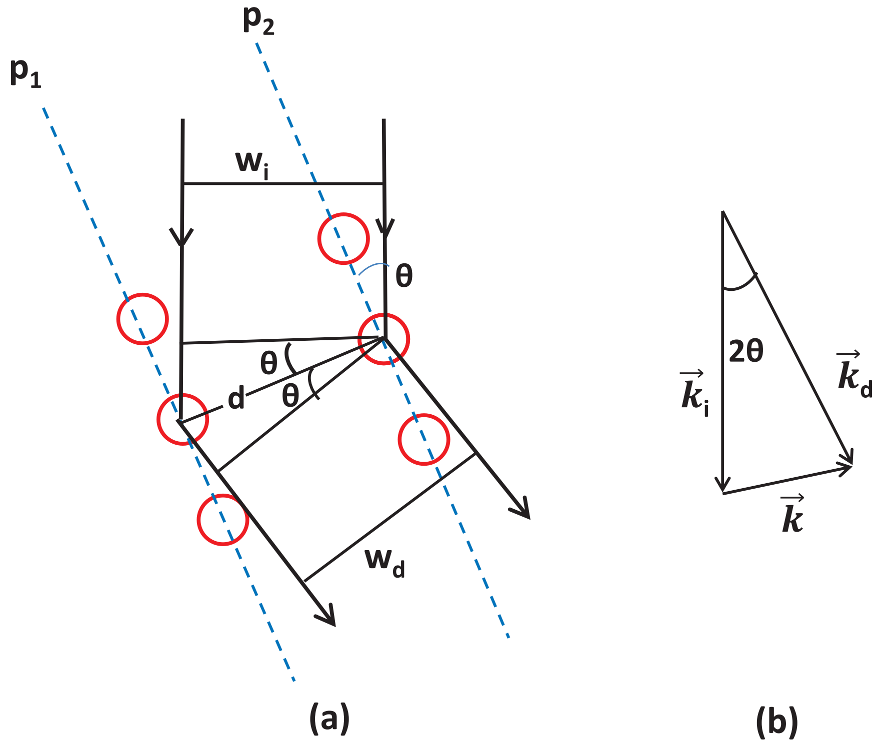

Figure 2.7: *(a) Diffraction from a plane, (b) the wave vectors*

Again from the Figure 2.7(a) we can see that the path difference between the incident and the diffracted wave is $2d\sin\theta$. If for the incident angle θ_B, Bragg condition of diffraction is satisfied, then

$$2d\sin\theta_B = n\lambda \tag{2.8}$$

where n is an integer and λ is the wavelength of the incident wave vector. Again from the Figure 2.7(b), we can write

$$\sin\theta = \frac{\mid \overrightarrow{k}/2 \mid}{\mid \overrightarrow{k_i} \mid} \tag{2.9}$$

since λ is magnitude of the incident wave vector, we can write

$$\mid \overrightarrow{k} \mid = \frac{2\sin\theta}{\lambda} \tag{2.10}$$

So, when the incident wave vector makes an angle equal to brag angle θ_B then,

$$\mid \overrightarrow{k} \mid = \mid \overrightarrow{k_B} \mid = \frac{1}{d} \tag{2.11}$$

The diffracting wave vector is defined as,

$$\overrightarrow{g} = \overrightarrow{k_B} \tag{2.12}$$

We can easily relate this diffracting wave vector $\overrightarrow{g}$ with the diffraction spot in TEM.

When electron beam is diffracted from a single crystal then for each plane we get a sharp spot in the diffraction pattern. The spot distance from the direct beam depends on the lattice constant of the crystal plane and the spot orientation of the spots is dependent on crystal plane orientation. Since in a poly crystalline substance, small single crystals are oriented in different direction, for each orientation of a particular plane produces a spot at same distance from the direct beam. Combination of these spots create a ring in the diffraction pattern. The radius of the ring is depends on the lattice constant of the crystal plane. A schematic of spot and ring diffraction pattern is presented in Figure 2.8. Diffraction pattern from an amorphous material also produces ring pattern but the rings are wide and there is no speckle.

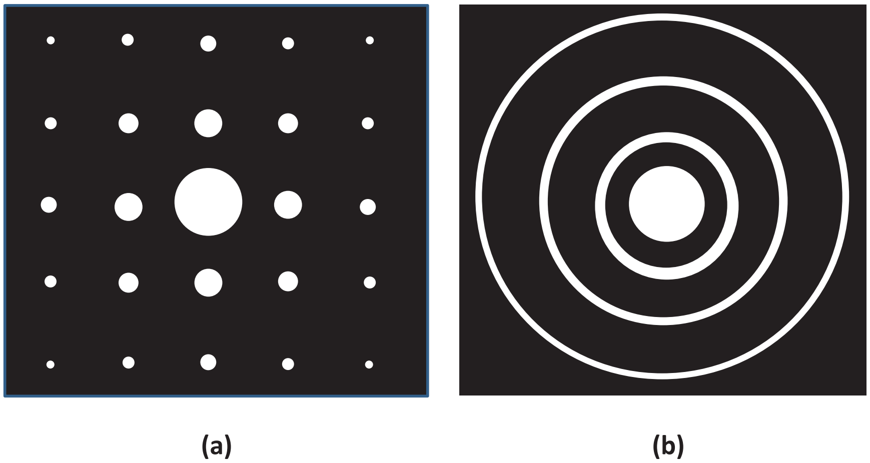

Figure 2.8: *diffraction pattern from (a) single crystalline material, (b) poly crystalline material*

From SAED pattern of a single crystalline material, we can obtain the lattice constant and the orientation of the plane. If ‘r’ is the distance of a diffraction spot from direct beam ‘d’ is the lattice constant of that plane, then the relation between them is given by,

$$rd = \lambda L \tag{2.13}$$

where ‘L’ is the camera length, which is the distance between the specimen and the screen. From the above equation, we can see that ratio of any two diffraction spots is equal to the ratio of lattice constant of corresponding planes. So from here we can find out the lattice constant and to get the orientation of the planes, we use the Weiss zone law. The diffraction pattern of a crystal depends on which zone axis we are looking through. The zone axis is defined as the the direction which is common to all set of planes in the diffraction pattern. If [UVW] is the zone axis then for any plane [hkl], the Weiss zone law is given by,

$$hU + kV + lW = 0 \tag{2.14}$$

If specimen is thick, then another type of diffraction may occur which is Kikuchi diffraction. Because of larger thickness (compared to electron transmission), many electrons are incoherently scattered. When these electrons satisfy Bragg condition then we get the Kikuchi diffraction. We observe the Kikuchi diffraction as a line on the screen, called kikuchi line. We can see the Kikuchi lines along with the SAED.

2.2.6 Bright field and dark field imaging

When the electron beam passes through the specimen, the electrons either interact with the specimen atoms or travel with out any interaction which are the so called direct beam. Depending on the choice of the electron beam selection, the bright field (BF), dark field(DF) and the central dark field (CDF) image is formed. For the BF imaging the direct beam is selected (Figure 2.9(a))and for the DF one of the diffracted beam is selected (Figure 2.9(b)). Now for the BF imaging , the selected direct beam proceeds along the optic axis but for the DF imaging the selected diffracted beam doesn't move along the optic axis. This may introduce different abberation for the DF imaging but the drawback can be removed by bringing the

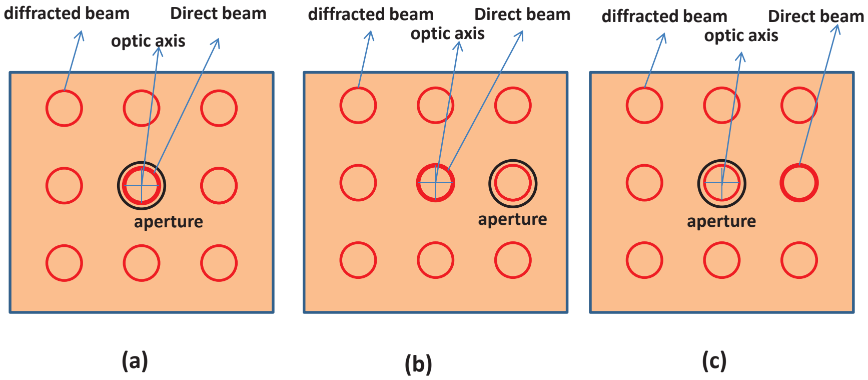

Figure 2.9: *(a) Bright field, (b)dark field, (c) centred dark field imaging*

scattered beam along the optic axis and it is accomplished by impinging the incident beam on the sample at an angle equal and opposite to the selected scattered angle(Figure 2.9(c)).

2.3 Scanning transmission electron microscopy (STEM)

Using a probe if the electron transmitting from an area of specimen are scanned then an image can be formed. This technique is called scanning transmission electron microscopy (STEM). The STEM technique is completely different from the TEM technique as lenses are not used to form the image. So in STEM operation we use a convergent beam and with out the scanning it resembles to the CBED pattern formation. The scanning of the beam is done using a double deflection coil in both x and y direction of the selected specimen area. The double deflection scanning coil is inserted at the front focal plane of the upper objective lens. By this upper objective lens the electron beam is brought parallel to the optic axis, such that diffraction pattern remains unaltered during the beam scanning. The scanning process takes longer time for image formation than TEM image formation but the advantage of the STEM technique is that the chromatic abberation is absent as the lens system is not used. Magnification in STEM imaging depends on selection of specimen area.

Like the BF and DF imaging in TEM, BF and DF STEM imaging is also possible. For BF and DF TEM imaging, aperture is used, where detectors are used for the STEM BF and DF imaging. For BF STEM imaging the detector is placed along the optic axis to collect the direct beam. Similarly to the DF TEM imaging, the diffracted beam is collected in the STEM imaging but here an annular dark field (ADF) detector is used and many number of diffracted beam are accumulated to form the image that gives better contrast. Now the electrons that are deflected by large angle due to Rutherford scattering can be collected by an another annular

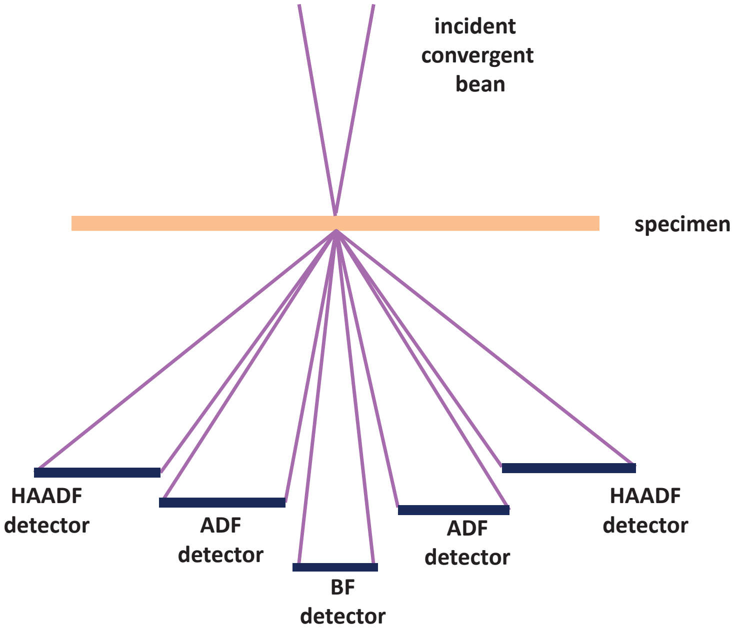

Figure 2.10: *Position of different detectors*

detector to obtain image which is called high angle annular dark field (HAADF) imaging. Generally the BF detector collect the electrons which are deflected less than 10 mrads, the ADF detector collects the electrons between 10 mrads to 50 mrads and the HAADF detector collect the electrons which are scattered more than 50 mrads (Figure 2.10). It can be calculated that the intensity of HAADF image varies with the square of the atomic number of the specimen. This intensity variation in HAADF image is useful to differentiate between elements.

2.4 Energy dispersive X-ray spectroscopy (EDX)

In a TEM when the high energetic electron hits the specimen, x-ray is also produced along with different signal. So an x-ray energy dispersive spectrometer is attached to collect and analysis x-rays to get elemental information of a specimen. An EDX spectrometer has mainly three parts, they are namely, detector, processing unit and multi channel analyzer (MCA). The detector collect the x-ray and convert them into electrical pulse and send it to the processing unit. The processing

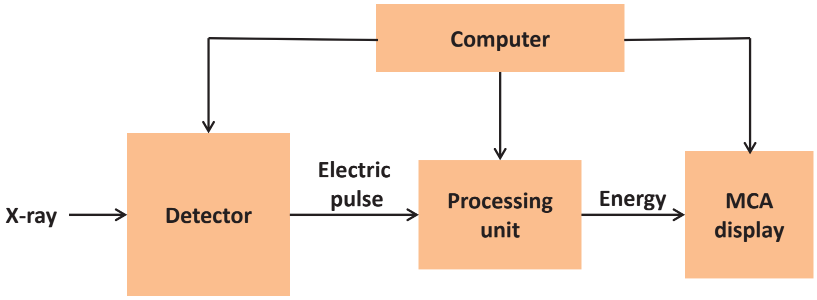

Figure 2.11: *X-ray energy dispersive spectroscope diagram*

unit amplify the signal and we see the final spectra in the MCA display. Generally Si(Li) detector is used in EDX spectrometer. When x-ray interact with the detector electron-hole pair is generated. These electron-hole pairs are separated by applying a reverse bias to create electric pulse (Figure 2.11).

We have used TEM imaging and analysis (TIA) software of FEI to perform the EDX analysis. The EDX can be done in TEM or STEM mode. For selecting the position of specimen STEM-HAADF image is captured. With the combination of the EDX and STEM we can identify multiple elements in a specimen. After acquiring a STEM-HAADF image we can select an image area and get the EDX spectra to find which elements are present (Figure 2.12(a)).

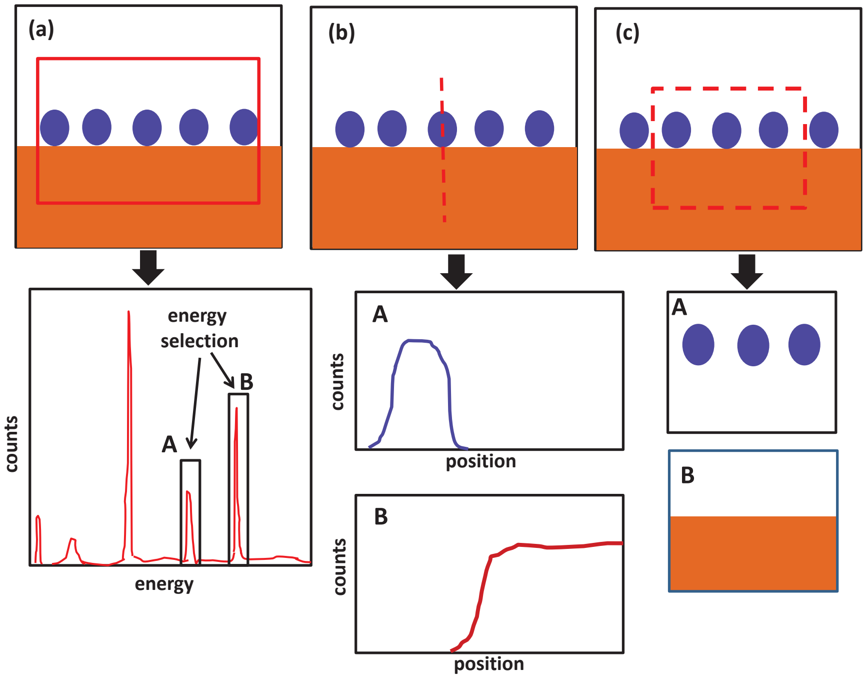

Figure 2.12: *(a) EDX spectra (b) line profile, (c) elemental mapping for STEM-HAADF image*

We can also obtain elemental line profile and mapping that provides elemental details with definite position. In line profile, at first EDX spectra is collected, then energy window is selected. Now a line is drawn on the STEM-HAADF image and elemental acquisition is started. The scanning is continued along the drawn line. When the acquisition is completed, for each element one spectra is obtained, which gives the elemental signature along the line. In Figure 2.12(a), the line is shown on a cross section image of nanoparticle deposited substrate and below the corresponding nanoparticle element and substrate element is displayed in two different window. For the elemental mapping an area is selected and the scanning is performed at each point of the area and finally the individual elemental image is obtained as shown in (Figure 2.12(c)).

2.5 TEM specimen preparation

TEM as a powerful instrument for micro-structure and composition analysis, but it requires special attention for the specimen preparation. In the TEM, the high energetic electron has to be transmitted through the sample, so we cannot insert the sample in any form. The liquid sample can be inserted by drying them on carbon coated copper grid but the solid sample is to be made electron transparent in the following way.

2.5.1 Initial thinning

The general size of TEM specimen are of 3 mm diameter. So a 3 mm diameter disc is cut from the sample and using a disc grinder (Gatan) and silicon carbide paper they are thinned to the appropriate thickness for dimpling. Care is taken such that no crack is introduced, otherwise the sample will be broken at the later stage when it is thinned down more.

2.5.2 Dimpling

After the initial thinning the centred portion of the sample is dimpled to reduce more thickness. As dimpling makes very small portion of the sample thinner, it diminishes chances of breaking of the sample. The sample is placed on the turntable of the dimple grinder, which rotates with a constant speed. The grinding wheel is rotated orthogonally to the turntable rotation. Its speed can be varied according to the sample hardness. We have used a dimple grinder of Gatan. While dimpling, diamond paste of grain size 3μ was applied on the sample, dimple thickness was set and then the grinding wheel was lowered on the sample. After dimpling the final polishing was done with $0.25\mu m$ grain size diamond paste.

2.5.3 Ion milling

The previously described mechanical thinning is not enough to make the sample electron transparent to analyse in TEM. A Precession Ion Milling System (PIPS)(Gatan, Pleasanton,CA model) has been used in this purpose. In a PIPS, generally Ar ions are impinged on the dimpled sample to knock out atoms from it to get the electron transparent sample. A CCD attachment with a LCD display is used to monitor the sample inside the PIPS chamber. In our present ion milling system, the energy of the ions can be varied upto 6 Kev and the angle of incident can be varied upto $\pm 10^\circ$. For ion milling of Ge, Si substrates, the energy of the ions was set to 3.5 KeV with a $\pm 4^\circ$ incident angle and under this condition, within $2-4$ hours electron transparent region is obtained. The electron transparency of the sample is confirmed when a tiny perforation appears in the dimpled region, which can be viewed in the LCD display.

2.5.4 Cross sectional TEM sample preparation

Cross sectional view in TEM impressively ease the detail structural analysis of nano-cluster or its interface property with the depositing surface. For the nanoparticles deposited on semiconductor substrates (Si, Ge), at first two pieces sample substrates of less than 3 mm width were cut and they are bonded with epoxy, keeping the deposited or the treated side face to face. We have used the Gatan Epoxy, which consists of two parts a resin and a hardener. They were mixed in 8:1 (resin:hardener) ratio. After the epoxy was applied to the sample, it is heated at 120° to get the strong adhesion.

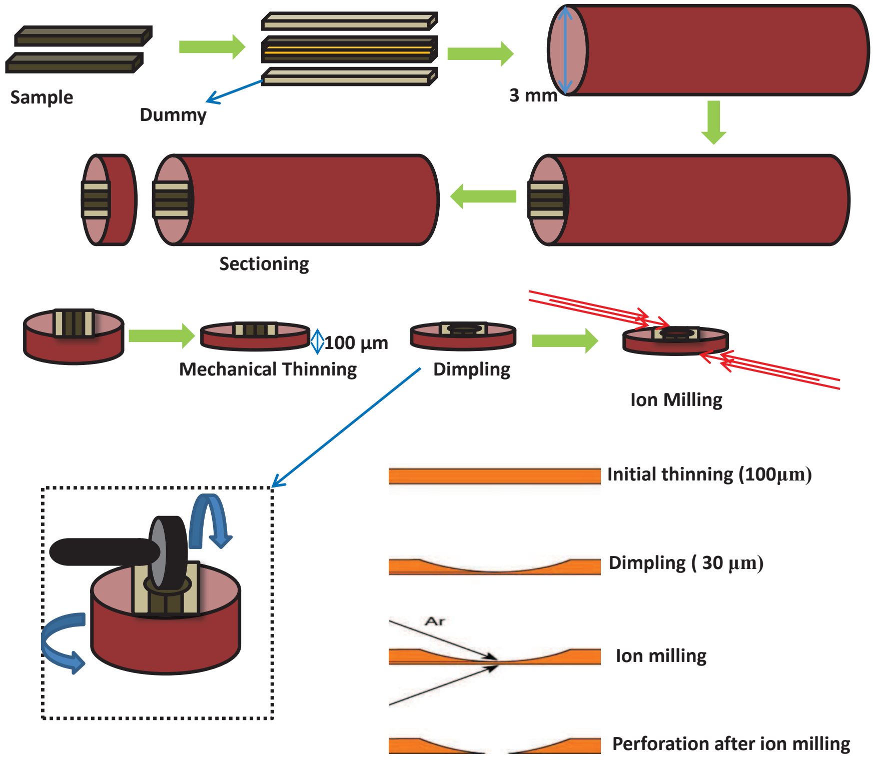

Figure 2.13: *Schematic for the TEM cross-sectional sample preparation.*

Now this composite is inserted into a brass tube and the empty place is filled with thin dummy substrates and epoxy. The sample contained brass tube is cut to get a 0.5 mm disc, using a diamond wire saw. This disc is now mechanically thinned to 60-100 μm as described earlier, with the disc grinder and silicon carbide paper of different grit size. The centre potion of this thin sample is now dimpled down to $30\mu m$ thickness and inserted inside the PIPS chamber for ion milling. After the ion milling the electron transparent sample is obtained which is ready for the TEM study. A schematic of the cross sectional specimen preparation is given in the Figure 2.13.

2.5.5 Plan-view TEM sample preparation

For the plan-view TEM specimen preparation, using low melting wax, the sample slice is bonded on a glass slide with the coating side facing it and a 3 mm size disc is cut from the sample using an ultrasonic disc cutter. The substrate side of the disc is processed through the mechanical thinning, dimpling and ion milling, to get the electron transparent specimen. Since the electroless deposition is simple deep and rinse process so it is possible to perform the deposition on the ion milled plan view substrate but care has to be taken as the sample edge is only 100 μm thick.

2.6 Scanning electron microscopy (SEM)

In earlier section, we have discussed about the electron interaction with matter. where we saw that when electron beam impinges on specimen many signals are generated. In a transmission electron microscope we are more interested in the transmitted electrons but utilizing the SE and BSE it possible to form image of a specimen with good resolution (lesser than TEM image). Advantage of the SEM is that the specimen is not needed to be thin and the incident electron beam is also of lesser energy but it provides mainly the surface information of the specimen. The accelerating voltage in a SEM is typically 5-30 keV. The beam diameter is made less than 10 nm by the lens system. This sharp electron beam act as probe is scanned over the specimen surface. The scan is performed in x and y perpendicular direction. The scan process is explained by the schematic (Figure 2.14).

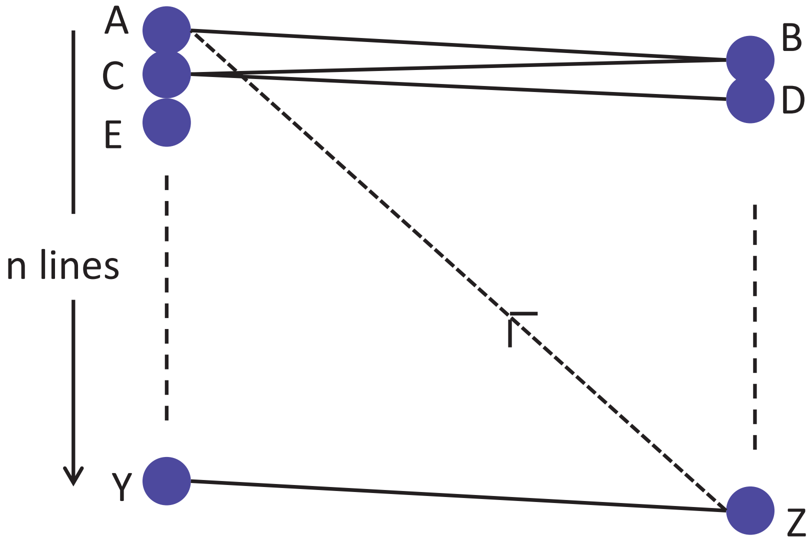

Figure 2.14: *Scanning process in a SEM*

Suppose after an x axis scan the probe reaches at point ‘B’ from the starting point ‘A’. Now when the the beam is brought back to the x axis position is doesn’t reach at point ‘A’, rather it reaches at point ‘C’ as y axis scan moves it. So it is clear that if there are n scan line for the x axis scan, its frequency will be n times of the y axis san. In this way the scan proceeds and when the final point

'Z' is reached, the probe is brought back to the point 'A'. As in SEM both SE and BSE image can be formed by scanning the probe they give two different contrast images. The SE image gives the surface information so it is called topological contrast image and the BSE image is called the atomic number contrast image as the BSE is produced by the Rutherford back scattering which depends on the atomic number.

2.7 Rapid thermal annealing (RTA)

Rapis thermal annealing is an effective procedure for fast heating in low cost. In a rapid thermal annealing unit it is possible to reach around 1000° within few minutes. To achieve this faster heating radiation heating is used. Generally halogen lamps are incorporated for radiation heating. In the rapid thermal annealing unit,

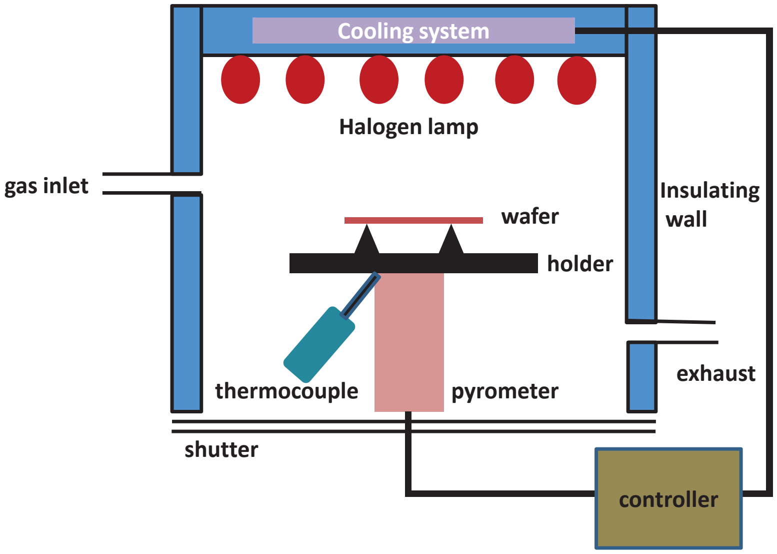

Figure 2.15: *Rapid thermal annealing(RTA) system*

the specimen is placed on a stage (generally made of silicon) below the radiation lamp. The heating chamber has a gas inlet and an exhaust valve to insert different gasses and to evacuate the chamber before and after the annealing process. In our rapid thermal unit, three gas inlets namely, oxygen, nitrogen and argon are connected and for vacuum operation a turbo-molecular pump and a backing rotary pump are used. Temperature in the heating chamber is measured by thermocouple and pyrometer which are connected to controller. Compressed air is maintained by this controller for steady temperature raise. With an interface software different parameters like the ramp up and down time, total annealing time, different gas injection rate, vacuum time is controlled.

2.8 Atomic force microscopy (AFM)

The atomic microscopy (AFM) is a simple and effective technique for three dimensional imaging with nanometer resolution. It is scanning probe technique, where the used probe is a sharp tip integrated at the end of a cantilever. The basic principle of AFM is that when the sharp tip is brought closer to the surface of a substance then different forces viz. van de Waals force, electrostatic force etc deflect the cantilever depending upon interaction forces. Measuring this cantilever deflection based on Hook's law a three dimensional surface image can be obtained.

The probe is scanned in a raster way over the specimen surface. Piezo-eelctric element is used to maintain this scanning process. To detect the deflection of the cantilever during the scan, a laser source is attached. The laser beam falls on the cantilever and reflects back and this reflected laser beam is detected by a position sensitive photodiode detector. A feedback electronics is included to monitor the

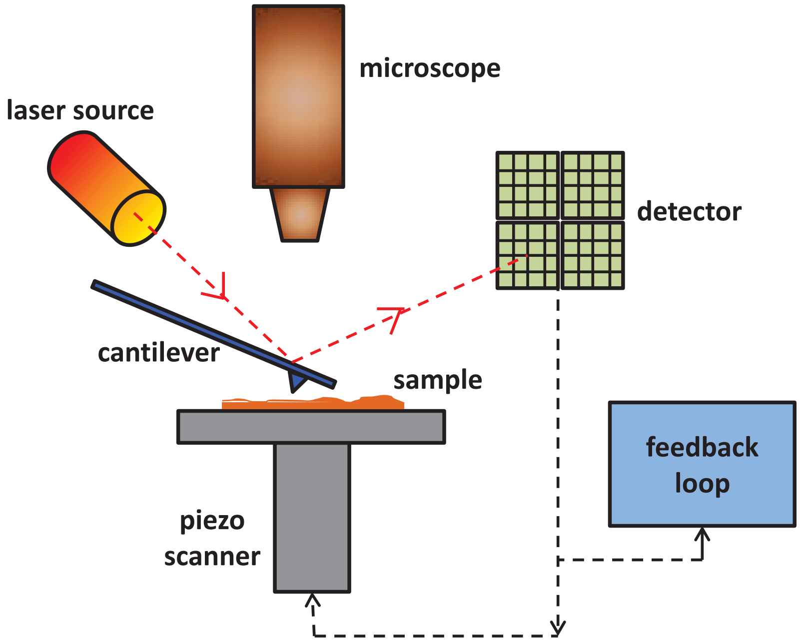

Figure 2.16: *Schematic of an atomic force microscope*

deflection of the cantilever. For the imaging, if the tip makes physical contact with the specimen surface during the scan, a constant force is maintained during the scan between the tip and surface by the feedback circuit and it is named as contact mode imaging. In non-contact imaging mode, the tip doesn't make any contact with the surface. This time the tip is oscillated near its resonance frequency and during the scan amplitude of the tip frequency is kept constant. There is another made, called tapping mode where the tip is scanned at an intermediate distance such that the oscillating tip barely hits the specimen surface.

Chapter 3

Galvanic displacement reaction

In this chapter the GDR deposition process, its application, limitation and theoretical aspects are described.

3.1 Introduction

The GDR has been proven to be an effective deposition technique in terms of cost reduction, selectivity, quickness and simplicity. The important convenience of the GDR is the production of versatile nanostructure on substrate surface which can be implemented in device application. Device application with galvanic displacement deposition can be enriched as the galvanic displacement can be implemented for the noble metal deposition on semiconductor surfaces. The GDR is also useful for the nano-patterning of semiconductor surfaces. So it is important to understand the growth mechanism and the metal-semiconductor systems in GDR. In the present thesis work insight about controlled GDR has been qualitatively and quantitatively discussed. Before going into the discussion, here few basic aspects of the GDR have been illustrated.

3.2 Different types of electroless deposition

The use of the electroless process appeared far after the electrolytic processes. The electrolytic processes begun with the Faraday equation in the middle of the nineteenth century whereas the electroless process was first introduced by Brenner and Riddell almost 100 years later [42]. We can relate the fundamental difference between these two processes by their name itself. The electrolytic process involves with external applied voltage and electroless process refers to application of no external voltage. The electroless process are mainly constrained in metal deposition, so here we discuss about the electrodeposition of the the electrolytic processes.

Illustration of the electrodeposition and electroless deposition is given in the Figure 3.1. In comparison with the electrodeposition, the electroless deposition is

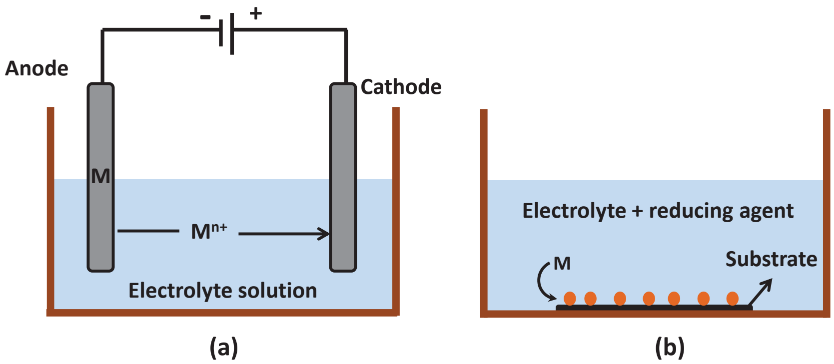

Figure 3.1: *(a) electrolysis (b) electroless process.*

more diverse in many aspects. Thus, in spite of their mechanism is explained by the redox potential, the electroless deposition is said to be chemical because no external voltage is applied. In contrast with the general metal reduction, in electroless deposition technique metal coating is obtained with out any large amount of the metal precipitation.

The electroless deposition is classified into three different types depending on deposition mechanism, namely, autocatalytic, substrate catalytic and galvanic displacement deposition. When the reduced metal itself act as a catalyst and further can reduce metal from the solution, then the deposition continues until all the ions are reduced, if sufficient amount of additives are added. Then it is called autocatalytic deposition. On the other hand, if the reduced metal can not reduce metal from the solution then the deposition ceases once the substrate is completely covered. It is then called substrate catalytic deposition. The GDR is slightly different from the previous two electroless deposition. In both the autocatalytic and substrate catalytic deposition, the substrate surface only catalyzes the metal reduction, which is accomplished by the reducing agent, but in the GDR, the substrate surface itself acts as a reducing agent and reduce the metal. The mechanism of the these three electroless deposition has been depicted in Figure 3.2. The galvanic displacement deposition proceeds as long as the electron can be transferred through the film. So the maximum film thickness deposited by the GDR is greater than that of the substrate catalytic deposition but as in the autocatalytic deposition reduced metal itself reduce more metal from solution, the maximum film thickness obtained by this process is more than both the substrate catalytic and the GDR.

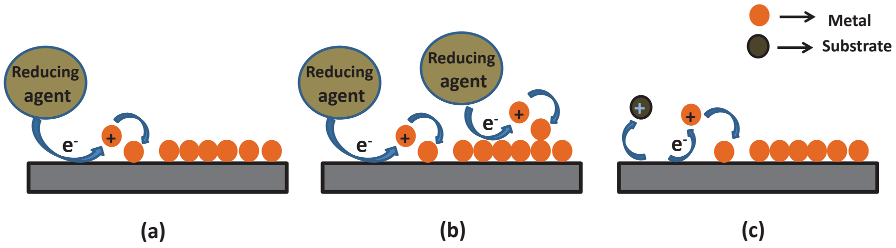

Figure 3.2: *(a)substrate catalytic, (b)autocatalytic and (c) galvanic displacement deposition.*

3.3 Different factors that influence GDR

Since the GDR does not even require any reducing agent, it is basically a direct charge exchange reaction between the two elements. Though the external applied voltage, reducing agent are absent in the GDR, the deposition environment affects the deposition process. The pH of the solution is such a parameter that has enormous impact on the galvanic displacement deposition. It can influence the initialization of the deposition process or can control the rate of the deposition.

For instance, with the same concentration of Cu solution and other experimental condition, in the acidic medium at pH 2, more homogeneous particle deposition is achieved than the deposition in the alkaline medium at pH 14 [43, 44]. Ni deposition on Si surface is not initiated at lower pH but once pH is raised the deposition starts. The bath temperature also has a direct effect on the deposition. In general, it is found that the deposition rate of the galvanic displacement increases with the bath temperature. As Yang et al observed for the Cu deposition with Si substrate cathode in presence of HF acid, the Cu deposition rate increase with the bath temperature [45]. Since the GDR is a oxidation- reduction reaction process, the charge transfer occurs to the deposited metal. So the rate of the deposition depends on both the oxidation of the substrate and the diffusion of charge. In the first step, the oxidation in the substrate surface is thermodynamically more favourable at high temperature, that consequences a greater deposition rate. On the other hand, the step of diffusion of charge may occur in the solution, in the substrate or through the deposited metal. Now the charge diffusion is a function of temperature, where it increases with the increasing temperature. Thus the increment of temperature assists the galvanic displacement process and also gives a higher rate of deposition. In this way the temperature increases the deposition rate up to a saturation level. Generally the metal nanoparticle deposited by GDR on semiconductor surface show good adhesion although it varies with the substrate and the deposited metal [25], but external additives in the galvanic displacement bath may effect on the adhesion. For example, Magagnin et al observed that addition of ascorbic acid improves the adhesion of copper film deposited by the GDR [46]. White light irradiation and stirring of the solution during deposition may also affect little the rate of the the GDR [27].

3.4 Noble metal deposition through GDR

The Au, Ag and Cu are the group 11 elements in the periodic table, with the full filled “d” orbital and half filled ‘s’ orbital in the outer shell. These three metals comes in the noble metal group though Cu is easily oxidized. Starting from the household use in bulk form, these three noble metals have fascinating properties in nano size. The unique optical properties of nanoparticles arises because of surface plasmon resonance between the free electrons of the nanoparticles and the incident electromagnetic wave. If the nanoparticle is assumed to be spherical then the polarizability is given the $3\epsilon_0 v \frac{\varepsilon-\varepsilon'}{\varepsilon+2\varepsilon'}$. Where v is the volume of the particle, ε and ε' are the permittivity of of the metal and the surrounding and ε_0 is the free space permittivity. Resonance condition is satisfied when $\epsilon = -2\epsilon'$. This is called Frölich condition for surface plasmon resonance. Surprisingly for the Au, Ag and Cu, the resonance frequency lies in the visible range [47, 48]. The fascinating optical properties of the noble metal particles make them potentially applicable in various occasions. For instance the noble metal nanoparticels can be used for cancer therapy [49]. They can be inserted into the tumor stroma by either by passive targeting which is through the fenestrations of the angiogenic vasculature or direct targeting which is done by incorporating peptides, antibodies, or DNA/RNA with the nanoparticles. After targeting the cancer cells, if radiation is applied to the diseased area then the, tumor cells are heated due to the surface plasmon resonance (SPR) of the noble metal nanoparticles [50]. The tunable surface plasmon resonance of noble metal nanoparticles makes them good candidate for sensing technology with the surface enhanced Raman scattering principle. The Raman scattering, which is an inelastic scattering of photon by the molecular vibration, is a week process. Now if the molecules are adsorbed to a metal nanoparticle the Raman scattering is increased by several times, it provides sensing the molecules even individually each of them. This enhancement in Raman scattering occurs due to local electromagnetic field enhancement by the surface plasmon of the metal nanopartocles [51]. The choice of noble metal nanoparticles comes because of their high enhancement factor and stability. Among the different noble metal nanostructures, silver has maximum enhancement factor for the surface enhanced Raman scattering. Typically silver and gold naoparticles have enhance factor of 10^6-10^7 and 10^3-10^4 [51] and the copper naoparticles have lesser enhance factor in comparison [52]. Noble metal nanoparticles also has influence on solar cell efficiency enhancement. It has been observed that incorporation of silver nanoparticle on silicon solar cell increases its efficiency by a good amount. The silver nanoparicles traps the incident light due to the localized surface plasmon resonance and increases the external quantum efficiency [13]. Now for all these application of the noble metal nanoparticles we can incorporate the GDR. Before we start, let us look into the redox potential of the noble metal gold silver and coper (Table 3.1) and compare them with the redox potential of germanium and silicon then we can see that it is higher for the noble metals [41]. The higher redox potential is more thermodynamically favourable for GDR so the noble metal can be reduced by germanium or silicon in the GDR process. Other than the deposition on the Ge or the Si substrate, different shaped noble metal nanoparticles can

Elements	**Redox potential(in V)**
Au^{3+}/Au	1.42
Ag^{+}/Ag	0.8
Cu^{2+}/Cu	0.34
Ge/Ge^{4+}	-0.12
Si/Si^{4+}	-0.86

Table 3.1: *Standard redox potential of different of different elements.*

be synthesised by wet chemical root by GDR with template nanoparticle of lower redox potential [19] and they may be used for the cancer therapy. As the redox potential difference between the noble nanoparticles and the Si and Ge indicates, noble metal nanoparticle can be deposited on Ge or Si substrate and can be used as SERS substrate. Several SERS studies for noble metal nanorticles on Ge or Si substrate by GDR, have been done. The SERS enhance factor as high as 10^9 for Ag-Ge system [12], 10^6 for Au-Ge system [20] and 10^7 for Cu-Si system [53] have bee achieved. Again for the solar cell efficiency increment, the galvanic displacement can also be implemented for the silicon wire solar cell fabrication [21] and noble particle can also be deposited at the same time to increase the absorption.

3.5 GDR on semiconductor surfaces

The first GDR was performed on the steel surface and gradually it has been applied for the deposition on different metal surfaces. The galvanic displacement of different metal nanostructure on semiconductor surfaces also paid enough attention for solar cell, censor and biomedical applications [19–21]. In this thesis work the galvanic displacement of different metal nanoparticles have been conducted mainly on the Si and Ge surfaces. The galvanic displacement deposition on Si and Ge defers due to solubility of their corresponding oxides. The galvanic displacement on Si surface is more complex compare to the galvanic displacement on Ge surface as the displacement reaction is generally performed in HF contained bath for the earlier. Air exposer of Si produces native oxide on its surface up to several $\mathring{A}$ thickness (Figure 3.3(a)). Now this unavoidable native oxide SiO_2 is not water soluble, so it hinder the direct contact of noble metal element with the Si surface, when the Si substrate is placed into the noble metal salt. As a result we don't observe any deposition, in spite of the noble metal element and Si satisfy the GDR criterion [54]. One way is to remove the oxide layer first by chemical or UV treatment and then start the deposition. Now for galvanic displacement of any metal on semiconductor surface, generally corresponding metal salt solution is used so the semiconductor surface comes in contact with water that also forms the native oxide and eventually stops the GDR. The native oxide formation of Si in pure water occurs by removal of Si atoms making the surface corroded [54]. So the galvanic displacement of metal nanoparticle on Si surface is conducted in presence

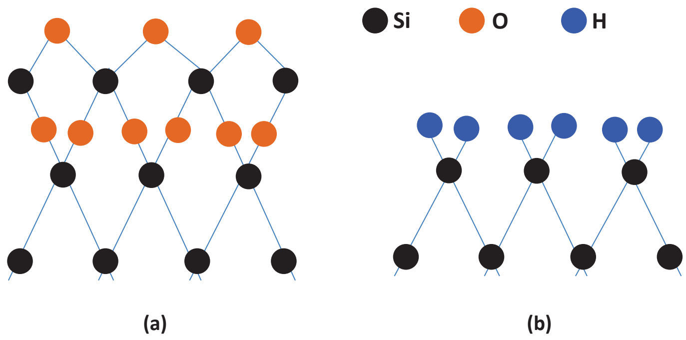

Figure 3.3: *(a) Native oxide on Si surface (b) H-termination after native oxide removal.*

of HF and it makes the reaction process more complex. When HF reacts with the native oxide of Si, it dissolves the native oxide layer by producing water soluble SiF_6^{2-}. The complete reaction is given as [55]

$$SiO_2 + 6HF = 2H^+ + SiF_6^{2-} + 2H_2O \tag{3.1}$$

The dissolution of the native oxide layer by HF ends up with H-terminated Si surface (Figure 3.3(b)). Such H-terminated Si surface prevents native oxide formation in water as well as in air for longer time. The H-terminated surface may be dissolved in pure water as well as in presence of HF [56–58]. The reaction precess of

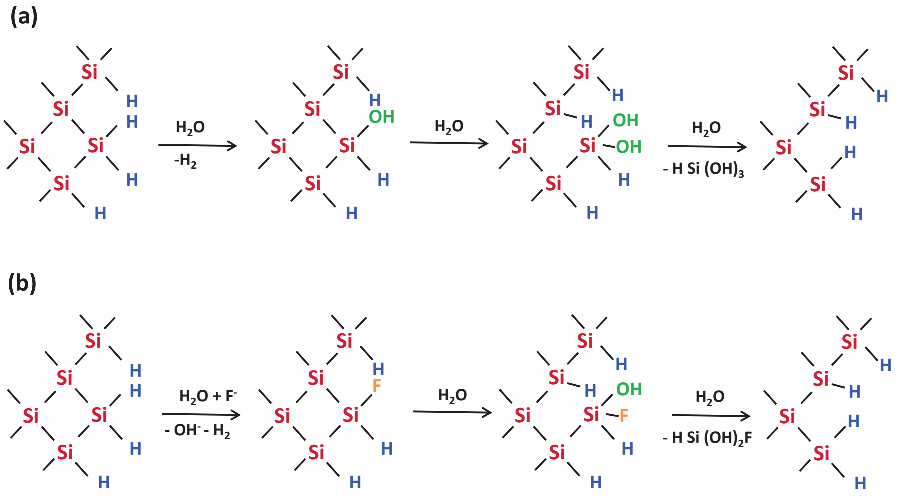

Figure 3.4: *Dissolution of H-terminated Si in (a) water, (b) in presence of HF.*

H-terminated Si in pure water is presented Figure 3.4(a). Here the $(OH)^-$ replaces the H site in steps and dissolve Si in the form $HSi(OH)_3$. The reaction process of H-terminated Si in presence of HF is presented in Figure 3.4(b). Here F^- and $(OH)^-$ replace the H site in steps and dissolve Si in the form $HSi(OH)_2F$. In both the processes the H-terminated surface is preserved. In case of GDR on Si surface in presence of HF, ion exchange occurs between the metal element and Si, at the same time Si is dissolved by HF in the form of SiF_6^{2-}. The chemical reaction (Figure 3.5(a)) of the redox couple is presented as

$$M^{n+}(aq) + Si^0(s) + 6F^-(aq) = M^0 + SiF_6^{2-}(aq) \tag{3.2}$$

Native oxide formed on Ge are GeO and GeO_2. Like the native oxide removal from the Si surface, the Ge native oxide can also be removed to get H-terminated surface by HF treatment, though such H-terminated Ge surface posses higher roughness than H-terminated Si surface [59]. During GDR on Ge surface GeO is formed,

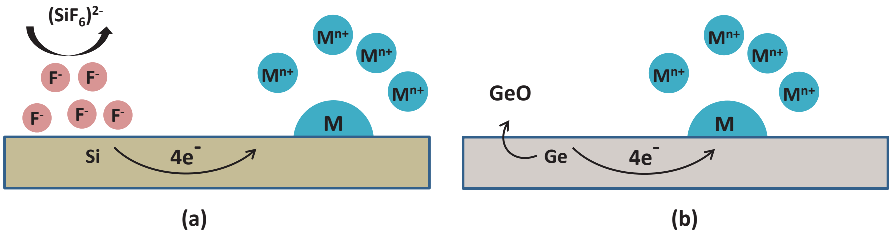

Figure 3.5: *galvanic displacement of metal element (a) on silicon , (b) on germanium.*

such oxide formation is given by [41],

$$Ge + H_2O = GeO + H_2 \tag{3.3}$$

Now, interestingly, GeO is water soluble. This leads to avoid the HF treatment for GDR on Ge surface. The displacement process on Ge surface is presented in Figure 3.5(b).

3.6 Different growth modes in GDR

The GDR provides many complex nanostructures, including nanosphere, nanodisk, nanobelt, nanodendrite, nanoinukshuk, etc [19, 27, 45]. Important feature of GDR is that the nanostructures formed by this process are with good crystallinity formed by epitaxial growth [60, 61]. An insight of lattice strain relaxation study has been done by T. Ghosh et al [61] depending upon the silver film growth on germanium surface by the GDR. The general way for the lattice stress relaxation in heteroepitaxial growth due to lattice mismatch are biaxial strain and misfit dislocation but another way is asymmetric tilt boundary formation. Such asymmetric tilt boundary induced heteroepitaxial growth was theoretically explained by Dodson et al [62]. This galvanic displacement growth study of silver nanoaprticle on germanium surface gives a better experimental evidence of the theoretical model given by Dodson et al. The epitaxial growth in GDR gives another advantage of better adhesion, which is useful for the sensing device fabrication [53]. Now let us consider the primary modes by epitaxial growth, which are namely the Frank-van der Merwe (F-M) growth, Volmer-Weber(V-W) growth, Stranski-Krastanov (S-K) growth. In F-M growth mode adatoms are adhered with the substrate surface

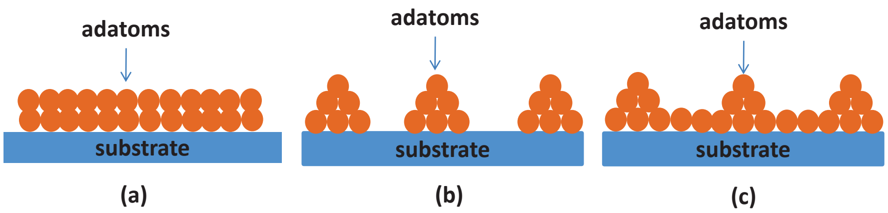

Figure 3.6: *Different growth modes (a) F-M growth, (b)V-W growth and (c) S-K growth.*

layer by layer. Thus in F-M mode smooth two dimensional film is formed (Figure 3.6(a)). In V-W growth mode, the adatoms bond together to form small cluster which is enlarged gradually (Figure 3.6(b)). So the roughness of the film grown in V-W mode is larger compared to the film grown in F-M mode but V-W mode mode provides different three dimensional shape formation in low dimension. The combination of F-M and V-W mode constitutes the S-K mode, where initially the adatoms form layer but after few monolayer formation, clusters appear to grow (Figure 3.6(c)). The smoothness of the film grown in the S-K mode is intermediate between the F-M and V-W mode film growth. These different growth modes can be explained by the thermodynamical consideration. If we consider the chemical potential of few layer of adatoms, then their chemical potential is given by Markov model [63] as

$$\mu(n) = \mu^{'} + [\phi_a - \phi_a^{'}(n)] + [\epsilon_d(n) + \epsilon_e(n)] \tag{3.4}$$

where, $\mu^{'}$ → bulk chemical potential of the adsorbate material

ϕ_a → desorption energy of an adsorbate atom from a wetting layer of the same material

$\phi_a^{'}(n)$ → desorption energy of an adsorbate atom from the substrate

$\epsilon_d(n)$ → misfit dislocation energy per atom

$\epsilon_e(n)$ → homogeneous strain energy per atom

Now if the misfit dislocation energy and the homogeneous strain energy is very small compared to the bulk chemical potential of adsorbate material then if $\frac{d\mu(n)}{dn} > 0$, the surface adhesive force is stronger than the adatoms cohesive force, so the adatoms stay bound to the substrate surface and F-M growth mode follows and if $\frac{d\mu(n)}{dn} < 0$ the adatoms cohesive force is stronger that the substrate adhesive force, so the adatoms are aggregated to form cluster and V-W mode follows. In S-K mode, initially $\frac{d\mu(n)}{dn} > 0$ condition is satisfied that gives layer growth but because of strain induced effect the growth condition is reversed and $\frac{d\mu(n)}{dn} < 0$ is established so the cluster formation starts. Initial growth in GDR was studied by many researchers, it was found that GDR follows mainly the volmer-weber growth [60, 64]. Similarly for the electrodeposition of Pb on Si, V-W growth mode was observed though the vapor of Pb in ultra high vacuum on Si, S-K mode had been witnessed. Since, in the GDR ion exchange occurs, it modifies the substrate surface such modification may lead to the V-W growth mode. For instance, Au island are easily formed on Si surface by GDR because of the H termination during the deposition process. The advantage of he V-W growth in the GDR is that different three dimensional nanostructures are produced by this process.

3.7 GDR and metal assisted etching

The GDR has been successfully incorporated for semiconductor substrate etching and obtaining their different nanostructure, which is greatly important for the semiconductor application industry. The GDR assisted chemical process is more advantageous than the chemical vapor deposition, laser ablation in many aspects for semiconductor nanostructure formation. Selectivity of GDR leads to such nanostructure formation. In this nanostructure formation by chamical process assisted with GDR, initially metal nanoparticles are deposited on the semiconductor surface by GDR and later the etching process dominates. The etching process may proceed in two different ways as depicted in (Figure 3.7). As the GDR is an ion exchange reaction, where the depositing surface get corroded, pits are formed below the deposited nanoparticles. Etching may occur along the pit or the particle uncovered area of the semiconductor surface. Etching along the pits can be performed only by the GDR. For instance, galvanic displacement deposition of silver nanoparticles on Ge for long interval provides formation of Ge nanopillar [65]. As the galvanic deposition continues for longer time, more Ge dissolves from the pit site and size of the pit increased (Figure 3.7(a)). After the deposition process ends, removal of silver particle by HNO_3 gives the final Ge nanostructure. To control the nanostructure formation application of additives may be useful. After the Ag paticle deposition on Si surface, addition of FeO_3 produces 1D Si nanostructure. Here the Fe^{3+} ion is reduced to Fe^{2+} by Si via Ag particle [66]. Silver particles remain unchanged in size as Ag^+/Ag system has more redox potential than Fe^{3+}/Fe^{2+} system. So Si is dissolved, the pit height increase but the Ag particle rests at bottom of the pit with the same size. Similarly for Ge nanostructure, after

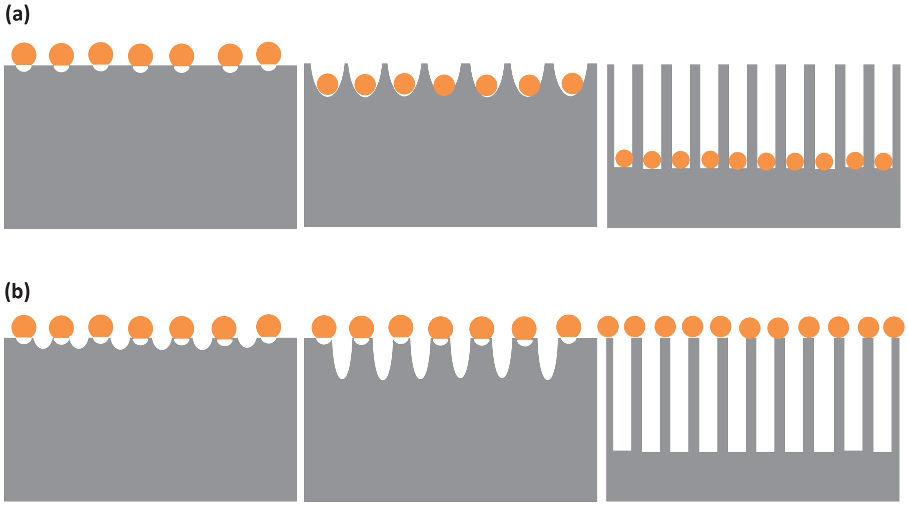

Figure 3.7: *different mode of etching (a) along the metal particles (b) along the uncovered area.*

depositing the Ag particle on Ge surface, reduction of H_2O_2 has been reported to obtain Ge nanostructure [65]. Now after the metal particle deposition, if high concentrated etchant is used then etching at the metal particle uncovered area is etched at higher rate than etching at pit. As a result semiconductor nanostructure is obtained (Figure 3.7(b)) with metal particles sitting at the extended sites [66].

Chapter 4

Controlled galvanic displacement reaction through amorphization

---

This chapter describes the insight of GDR and its relation with substrate amorphization and decomposition.

4.1 Introduction

Electroless deposition has broadened the applicability of metal deposition techniques in many respects due to its technological importance, time and cost effectiveness, and exploration for atomic level deposition. Electroless processes include the autocatalytic process, the substrate catalytic process and the GDR. These processes require no external applied voltage, which ensures immense purity in comparison with electrolytic plating, where the GDR being in the electroless family, surprisingly appears with no external reducing agent. The GDR has been successfully implemented in micro electromechanical systems (MEMS), where the requisite selective deposition is provided by the displacement process [67]. Availing the galvanic displacement technique, scanning force microscope cantilevers have been successfully coated to minimize their stress factor [68]. Magnetic nanodot formation is also conceivable by this technique, which has applications in ultra-high density ROM and RAM devices. For instance, nickel deposition at a high pH value of 8 has been attained [44, 69–71]. Turning to the structural aspects, diverse nanostructure formation by the galvanic displacement technique has also been studied. Inukshuk-like silver nanostructures made up of hexagonal building blocks have been obtained with a long period of deposition; dendritic structures have also been found to be achievable [22, 27, 72–78]. SERS study on such silver nano-inukshuks revealed an electromagnetic field enhancement, demonstrating them to be a SERS effective substrate [61], that eventually can be used in sensing devices.

These different perspectives of the GDR have been illustrated earlier in details.

To augment understanding of the underlying mechanism in the GDR, several investigations have already been performed [22, 70, 71, 79–90]. In assistance of this reaction, metallic films on metal and metal alloy surfaces have been deposited [79–81]. The deposition of noble metals such as gold, silver, platinum and palladium has been studied on semiconducting surfaces, leading to the formation of metal semiconductor interfaces [25, 27, 61, 82–85, 91–94]. A comparative study made by depositing Au on Ge and Si surfaces revealed the formation of bonds in the case of Au-Ge interfaces and their absence in the case of Au-Si systems [25]. Strong adhesion of Au was found on GaAs, GaP and InP surfaces when the substrates were activated in an acidified solution of palladium chloride. Faceted Au nanoparticles were produced on InP substrate in the presence of H_2SO_4 [86, 91]. In several studies have been accomplished on the Ag and Au nanoparticles were synthesized in the GDR and it was confirmed that the substrate got corroded during the reaction [92, 93, 95]. The detailed mechanism of the GDR is still not well understood when substrate has different disorder. Here, the extensive use of TEM and associated EDX and STEM-HAADF technique allowed us to successfully demonstrate the role of electrochemical Ostwald ripening in GDR towards formation of uniform particle on amorphous Ge (a-Ge) surfaces compared to crystalline Ge (c-Ge) during Ag deposition. The advantageous selection of Ge in the GDR provides us a fluoride-source free deposition, since the reaction product GeO is water soluble and hence we end up with a simple dip and rinse Ag deposition on Ge substrate. Uniform Ag nanoparticle formation on ion bombarded surfaces implies the role of electrochemical Ostwald ripening in addition to the GDR, governed by the particle size dependent electrochemical potential [96, 97]. In this work we propose and demonstrate the synergetic effect between electrochemical Ostwald ripening and the GDR in order to interpret the ambiguity in particle growth on surfaces with different disorder. Our work offers control over the particle formation in the GDR to some extent and pave a way towards uniform particle growth. At the same time, a comparative study has been carried out using Au and Ag and their role in substrate corrosion.Our TEM study shows that for same deposition time, Ag decomposes the Ge surface more than the Au does. This overall study gave some insight towards use of GDR in the process of thin film deposition.

4.2 Electrochemical Ostwald ripening and surface diffusion in the GDR

4.2.1 Experimental

Cleaned and degreased n-type Ge(100) substrates were bombarded with a 14 keV mass analyzed oxygen beam at a normal angle of incidence (0^o) with a fluence of 1.8×10^{18} ions per cm^2 to make an amorphous Ge substrate. The range of 14 keV O^+ ions in Ge is 59 nm from TRIM [98] calculations over the entire ion exposed area. We took one crystalline and one ion bombarded Ge substrate and dipped them into 1 mM $AgNO_3$ solution in different containers and allowed the reaction to happen under identical conditions. After a short interval of 2 minutes they were taken out of the solutions and dried in air. The topographic images of the pristine Ge surface and Ag deposited Ge substrates were obtained using a Bruker multimode-V atomic force microscope (AFM) in contact mode (air) with a silicon nitride tip of 20 nm radius of curvature. We processed the Ag deposited Ge substrates through cross sectional specimen preparation technique as described previously to study in TEM. For the plan view TEM study initially plane view specimen is made with the Ge substrate as illustrated earlier and then Silver nanostructures were grown on the electron transparent Ge discs by floating on a $AgNO_3$ solution such that Ag deposited on one side (i.e. the mirror polished side). In this way we avoid any changes in topography in the process of TEM sample preparation of these metal nanoparticles as they are very weakly bound to the Ge substrates. An FEI Tecnai G^2 F30, S-Twin microscope equipped with a Gatan Orius CCD camera was used for TEM study. The attached scanning unit and a HAADF detector from Fischione (Model 3000) was used to perform STEM-HAADF imaging. Compositional analysis was performed by the EDX (EDAX Inc.) attachment on the Tecnai G^2 F30.

4.2.2 Result and discussion

The GDR for the Ag-Ge system having a net positive cell potential ensures no need of any external reducing reagent and is described as follows [91, 93, 94].

$$Ge \longrightarrow Ge^{4+} + 4e^- \qquad (E^0 = -0.12V)$$

$$Ag^{+1} + e^- \longrightarrow Ag \qquad (E^0 = 0.8V)$$

where, E_0 is the standard electrode potential. Figure 4.1(a-c) present the AFM topographic images of the virgin germanium substrate, Ag nanoparticles were deposited on crystalline Ge, and the 14 keV oxygen ion bombarded Ge substrate, respectively. Here the substrates were dipped into 1 mM $AgNO_3$ solution for 2 min under identical conditions in the later two cases.

The silver nanoparticles deposited via the GDR on crystalline and the oxygen ion bombarded germanium substrates are shown also by the XTEM images in Figure 4.2(a-c). Substrate 1 and 2 represent the ion bombarded and crystalline germanium surfaces, respectively after deposition. In the inset of Figure 4.2(b) we show

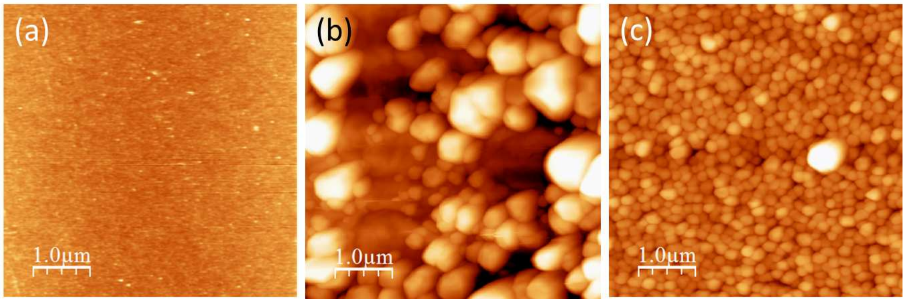

Figure 4.1: *AFM images (a) virgin Ge(100), (b) and (c) Ag nanoparticles deposited on crystalline and* O^+ *ion bombarded Ge substrate, respectively under identical conditions*

one ion bombarded Ge substrate where the lighter contrast represents the amorphous area (thickness $\sim 46.2nm$). The corresponding STEM-HAADF images from the same area are shown in Figure 4.2(d) and Figure 4.3. The higher intensity in the STEM-HAADF images is due to the silver particles having a higher atomic number, whereas the lower intensity is due to the lower atomic number germanium. Figure 4.2(e) shows the elemental mappings corresponding to the STEM-HAADF images from area 1 and 2 in Figure 4.2(d). Figure 4.2(e) successively, from left to right, shows the STEM-HAADF images, germanium maps, silver maps and the composite maps of germanium and silver. Elemental mapping is described in Figure 4.2(e), where X-rays were collected from both the substrates (marked by the orange coloured rectangular boxes in Figure 4.2(d)) by selecting the energy window of the silver L line and germanium K line in the X-ray spectra while a beam of about 1 nm is scanning the area. Thus the two elemental maps precisely confirm the formation of silver nanoparticles on crystalline and ion bombarded germanium surfaces.

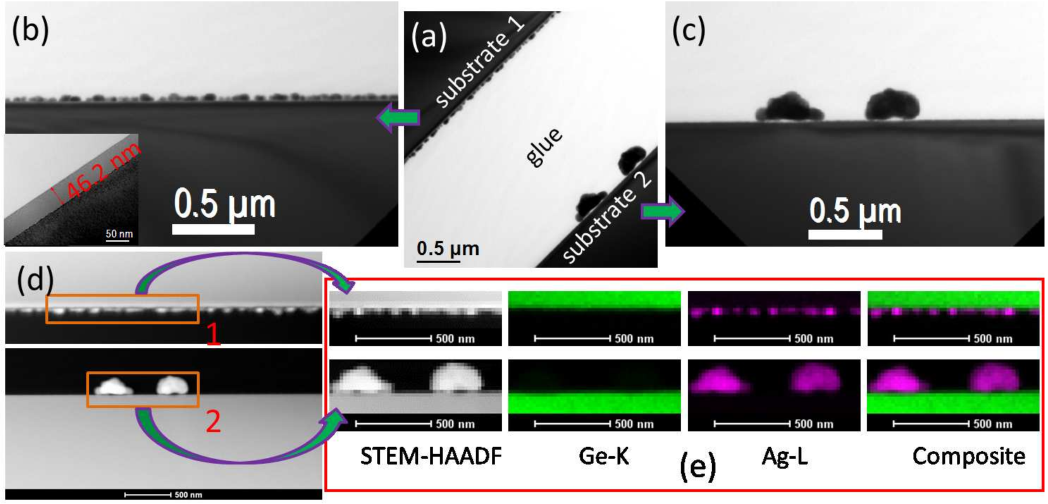

Figure 4.2: *(a) XTEM image of Ag nanoparticles deposited on ion bombarded Ge (substrate 1) and crystalline Ge (substrate 2). (b, c) Magnified images from two substrates marked by arrows. Ion bombarded Ge substrate is shown in the inset of (b). (d) STEM-HAADF image. (e) Elemental mapping of the areas marked by rectangles 1 and 2 in (d).*

One can see from XTEM and AFM study that the particles distribution is random and much bigger in size on the crystalline germanium surfaces compared to the ion bombarded surfaces. As the time of deposition (two minutes) and other experimental conditions are same in both the cases, one could expect the same result. But since the substrates have a different nature, a different mechanism is taking place in silver nanoparticle formation on c-Ge and a-Ge by the GDR. In search of such mechanisms we conducted a few controlled experiments which are described in the following sections.

C. Colliex and co-workers have studied the influence of surface defects on graphite by depositing antimony clusters produced by a gas-aggregation cluster source at room temperature by varying the density of defects in the substrate [99]. They

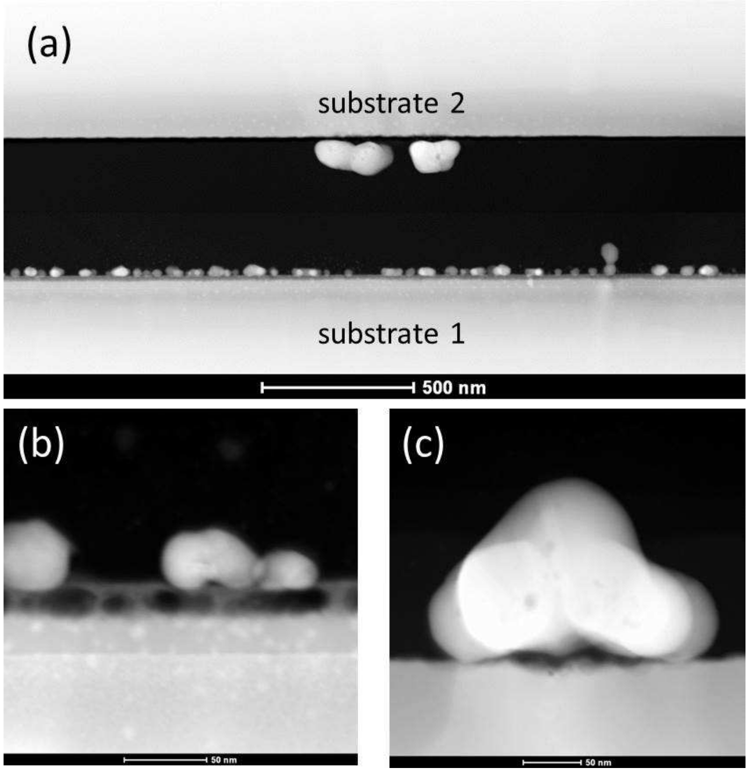

Figure 4.3: *(a) STEM-HAADF images of Ag nanoparticles on Ge substrates. Magnified images, on (b) amorphous and (c) crystalline substrate.*

have observed that as the density of surface defects increases, the density of islands increases and their size decreases. Compared to the GDR, with a completely different source of deposition, the diffusion of the antimony clusters is strongly dependent on the island temperature and the diffusion is principally thermal energy driven. To investigate the different type of particle growth in the GDR depending on the substrate having different disorder, we recall the size dependent electrochemical potential and the activation energy of nanoparticles [100–103].

Brus et al. have reported that thermally evaporated silver nanoparticles on a conducting substrate spontaneously grow to a larger size when the substrate, containing nanoparticles, is immersed into pure water [104]. A particle reconstruction to form larger particles starting with a particle size as small as 1.5 nm was shown and the mechanism was explained as electrochemical Ostwald ripening, where particle enlargement occurs as the smaller metal nanoparticles which are more easily oxidized than bulk material and are dissolved by transferring Ag^+ ions into the water, which then got deposited onto the larger particles and made them even larger. Here, the GDR and subsequent deposition occur atom by atom and we have conducted experiments on crystalline and amorphous substrates, under identical conditions. The discrepancy between the particle growth on crystalline and amorphous substrate indicates that the electrochemical Ostwald ripening took place during the process of the GDR. Plieth showed that the chemical potential of nanoparticles increases negatively as their size is decreased and is described by the following equation [96].

$$\triangle E = -(\frac{2M\gamma}{zFr}) \tag{4.1}$$

where M, γ, z, and F represent the molar volume, surface free energy, lowest valence state, and Faraday constant, respectively and r is the radius (assuming a spherical shape of the particle). A plot for the electrochemical potential shift for the silver nanoparticles using the surface free energy of silver of 1.45 J/m^2 is shown in Figure 4.4. It predicts that the chemical potential of silver atoms could be -2.146 V and the measured experimental value is -1.8 V [105]. The negative shift in the chemical potential for the smaller nanoparticles suggests that they will be more easily oxidized than the bigger nanoparticles, making the electrochemical Ostwald ripening happen, and that could lead to bigger particle formation

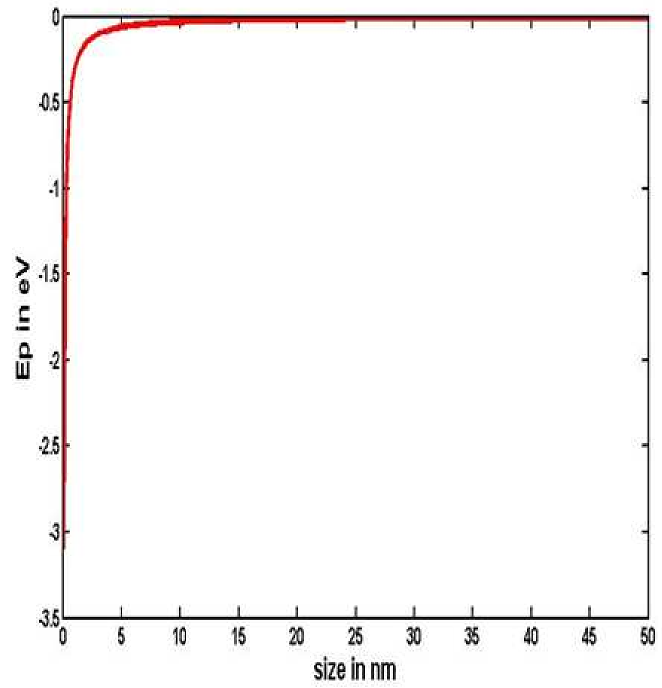

Figure 4.4: *Variation of chemical potential as described in equation 4.1 .*

at the expense of smaller particle dissolution. In the Ag particles growth on c-Ge surfaces, initially the Ag atoms got deposited on the Ge surface by the GDR (Figure 4.5(a)) and formed smaller Ag nanoparticles. These Ag nanoparticles are obviously not all the same size. In electrical equilibrium larger particles possess a partial negative charge compared to smaller particles as the Ag^+ ion density near the bigger particles decreases in the solution [96, 104, 105]. This size difference introduces electrochemical Ostwald ripening during the GDR, where the Ag^+ ions got deposited on to the bigger nanoparticles which possess partial negative charge and the electrons are supplied by the smaller particles resulting in Ag^+ ion release from the smaller particles into the solution (Figure 4.5(b)). Here the GDR also

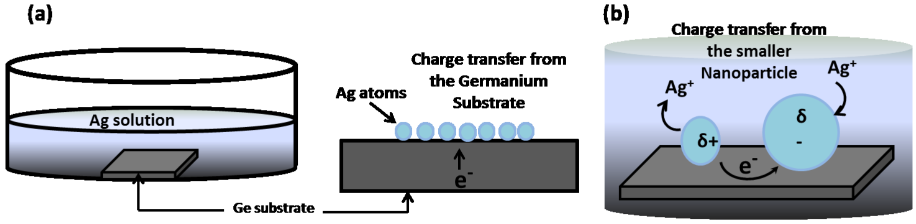

Figure 4.5: *Illustration of (a) galvanic displacement process, (b) electrochemical Ostwald ripening.*

continues at the same time but the emergence of Ostwald ripening makes the particle formation irregular. Silver particle formation on crystalline and amorphous Ge substrates shows that the amorphization reduces the contact angle of the Ag particles deposited on the Ge substrate (Figure 4.3) [106, 107]. This observation also indicates the decrease of the surface energy of the a-Ge substrate. The reduction in contact angle increases the radius of curvature (r) of the particle. Now, according to Equation 4.1, if the r value of Ag particle increases (on a-Ge) then the negative shift in electrode potential will be less and the Ag will not be easily oxidized, and eventually electrochemical Ostwald ripening will be diminished. This observation is in agreement with the uniform Ag particle formation on a-Ge surfaces. Ag particle growth on ion bombarded germanium surfaces gives rise to regular and continuous growth as the electrochemical Ostwald ripening is hindered by the amorphous nature of the substrate. The amorphization also decreases the conductivity by a few orders of magnitude [108]. This reduction in conductivity prevents the electron transfer from the smaller particle to the bigger particle in the process of electrochemical Ostwald ripening. This causes localized particle formation leading to the growth of uniform and ordered particles. We extended our study for the Ag particles growth on Ar^{2+} ion (energy: 24 keV, angle of incidence:

0^o and fluence: 7×10^{17} ions per cm^2) bombarded Ge substrate also to examine the role of oxygen ions in the amorphization process and their presence in the ion bombarded region. Oxygen atoms can saturate the dangling bonds appearing on the surfaces of voids, locally forming compounds such as GeO, and thus decreasing the extrinsic conduction. The AFM topographic image and cross sectional TEM image (Figure 4.6(a) and 4.6(b) respectively) depict a similar regular particle formation in the case of Ar ion bombarded Ge substrate. The magnified TEM image in Figure 4.6(c) clearly shows the amorphous layer due to Ar ion bombardment and Ag particle growth on the a-Ge surface. Lighter Ge contrast in the sub-surface region clearly demonstrates that the Ag particle formation is at the expense of Ge. Detailed EDX elemental maps and line profiles for the Ag particle deposition on O^+ and Ar^{2+} ion bombarded Ge are presented in Figures 4.7 and 4.8. Where two lines have been drawn in the STEM-HAADF images (Figure 4.7(a) and 4.8(a)) and x-rays have been collected along these lines; corresponding elemental profiles have been shown in Figures 4.7(c),(d) and 4.8(b),(c). Silver particle growth on O^+

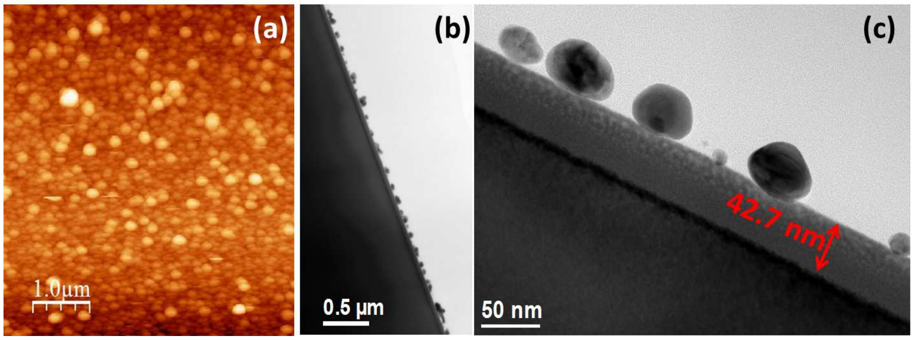

Figure 4.6: *(a) AFM image of Ag particles grown on Ar bombarded Ge surface. (b) Low magnification cross sectional TEM image. (c) Magnified TEM image of the sub-surface region from an area shown in (b).*

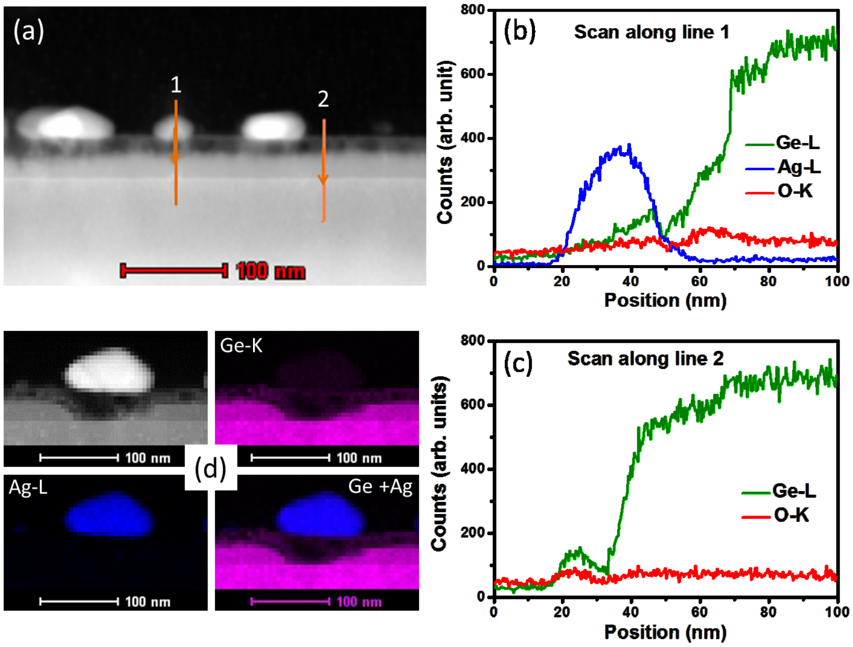

Figure 4.7: *(a) (a) STEM-HAADF image. (b) EDX elemental line profile along the line 1. (c) EDX elemental line profile along the line 2. (d) STEM-HAADF, elemental mapping using Ge-K, Ag-L lines and composite image.*

and Ar^{2+} ion bombarded Ge substrates collectively suggest that the uniform particle growth arises mainly due to the amorphization, which reduces the electron mobility and affects electrochemical Ostwald ripening in the early stages of the GDR. In the process of electrochemical Ostwald ripening, when an Ag atom was deposited on the Ge surface by the GDR very close to a bigger particle, it donates an electron to the bigger particle as described previously. This Ag^{+} ion may now move towards the bigger nanoparticle as elucidated in Figure 4.9.

Such diffusion processes will also lead to a discrepancy in the particle growth on crystalline and amorphous surfaces because amorphization by the ion bombardment creates many defects that will interrupt the diffusion of the Ag^{+} ions on the

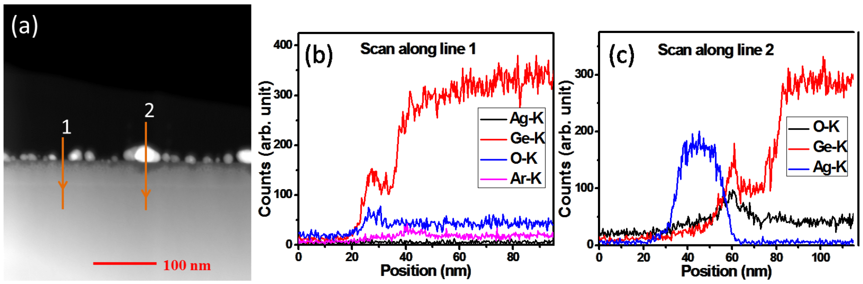

Figure 4.8: *(a) STEM-HAADF image of the Ag nanoparticles grown on Ar ion bombarded Ge substrate. (b, c) EDX elemental line profile along the line 1 and line 2, respectively shown in (a).*

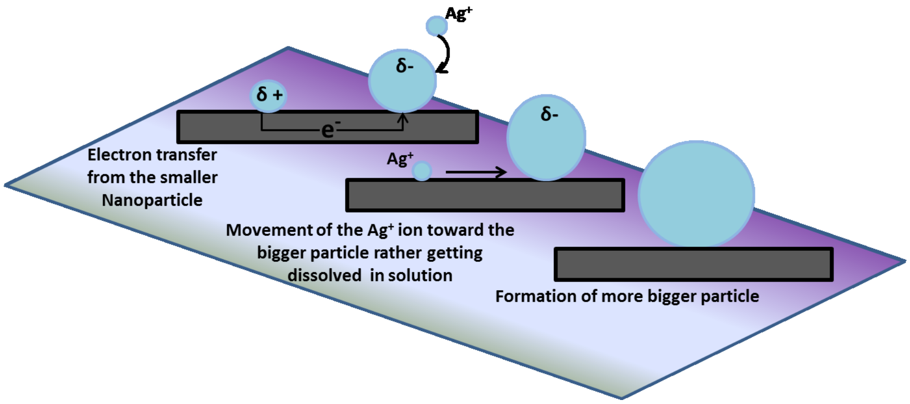

Figure 4.9: *A Illustration of the surface diffusion mechanism.*

a-Ge surface. When an atom moves on a crystalline surface it experiences a periodic potential (Figure 4.10(a)), the presence of defects can create certain minima in the periodic potential (Figure 4.10(b)) that disturbs the motion of the atom and tries to make it stabilized [109]. So for a less defective surface, it is easier for the Ag atoms to diffuse towards the bigger nanoparticles. For a more defective surface the probability of the Ag atom getting trapped is greater and these trapped Ag atoms locally accumulate more Ag ions to create nanoparticles, giving rise to a more continuous particle formation with uniform size. To understand the growth

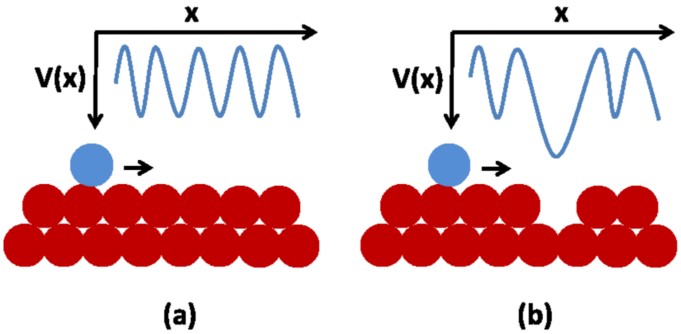

Figure 4.10: *The periodic potential experienced by an atom when moving on (a) a perfect crystalline surface, (b) a defect induced surface.*

of Ag particles on the c-Ge substrate further we have deposited Ag particles for various short intervals of time on p-type and n-type substrates (presented in Figure 4.11 and Table 4.1). One can see from these images and the corresponding particle size distributions that larger particles are formed and also inter particle separations increase gradually as the time of deposition increases. This is an indication of the Ostwald ripening process. To investigate the role of the electronic conductivity of different substrates, one can compare the 30 s, 60 s and 120 s Ag deposition on n-type and p-type crystalline Ge (depicted in Figure 4.11).

Substrate	***Time of deposition***	***Particle counts***	***Percentage of areal coverage***	***Mean size (nm)***	***Standard deviation (nm)***
n-type	***30 sec***	2891	11.60	9.1	10.8
	1 min	1571	26.01	17.6	22.7
	2 min	1390	30.78	22.8	24.2
p-type	***30 sec***	1610	15.55	17.1	13.6
	1 min	1499	25.22	23.8	16.5
	2 min	1230	29.78	28.8	19.3

Table 4.1: *Summary of the results presented in Figure 4.11.*

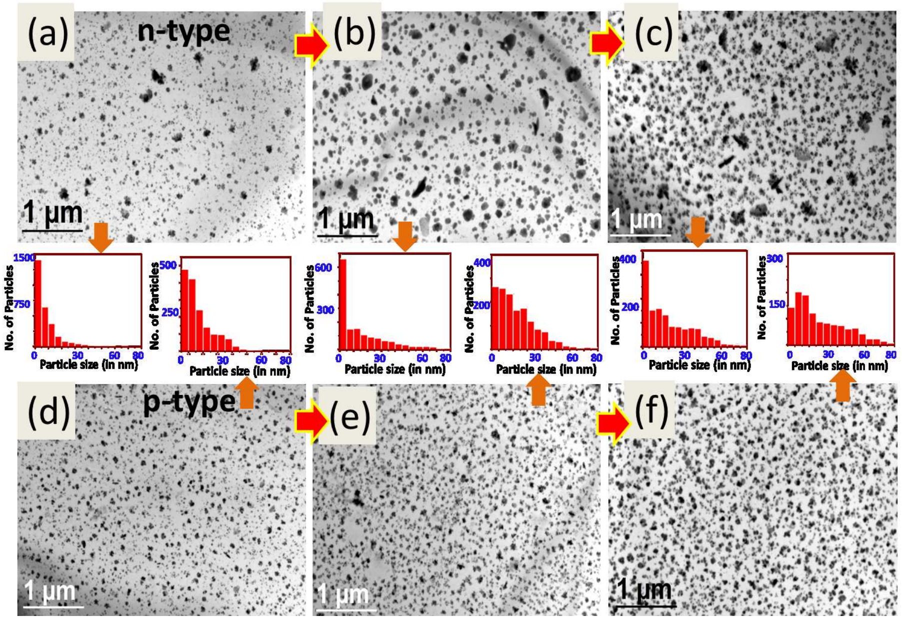

Figure 4.11: *Plan-view TEM images of Ag nanoparticles deposited on n-type and p-type c-Ge substrate of same resistivity (0.3 $\Omega - cm$) for (a) and (d) 30 sec, (b) and (e) 60 sec, (c) and (f) 120 sec, respectively. The corresponding particle size distributions are shown by orange color arrows.*

More regular Ag particle growth on p-type Ge was observed compared to the n-type, which is consistent with the earlier observation made by Buriak et al [27]. The lower mobility of holes in the p-type substrate than that of electrons in the n-type substrate makes the Ostwald ripening slower to give rise to a uniform particle distribution in the p-type c-Ge in a similar fashion to that observed in the ion bombarded amorphous substrate.

Now to separate out these two processes (viz., Ostwald ripening and the GDR) we conducted the following experiments. First, we grew Ag particles on c-Ge by floating the thin substrates (p-type and n-type of the same resistivity ($0.3\Omega - cm$) and ready for plan-view TEM measurements) on 1 mM $AgNO_3$ solution and allowed the reaction to happen for 30 seconds (here we assume that both the GDR and Ostwald ripening are happening) then observed and recorded TEM images (Figure 4.12(a) and 4.12(b). Then, the same substrates, containing Ag particles grown previously were dipped into water for 3 hours (here we assume only Ostwald ripening is happening). Again we carried out TEM measurement and recorded TEM images (Figure 4.12(d) and (e)). One can see from these TEM images, the corresponding particle size distributions and Table 4.2 that the Ag particles are becoming larger in size and the inter-particle separation also increases, which is a result of electrochemical Ostwald ripening.

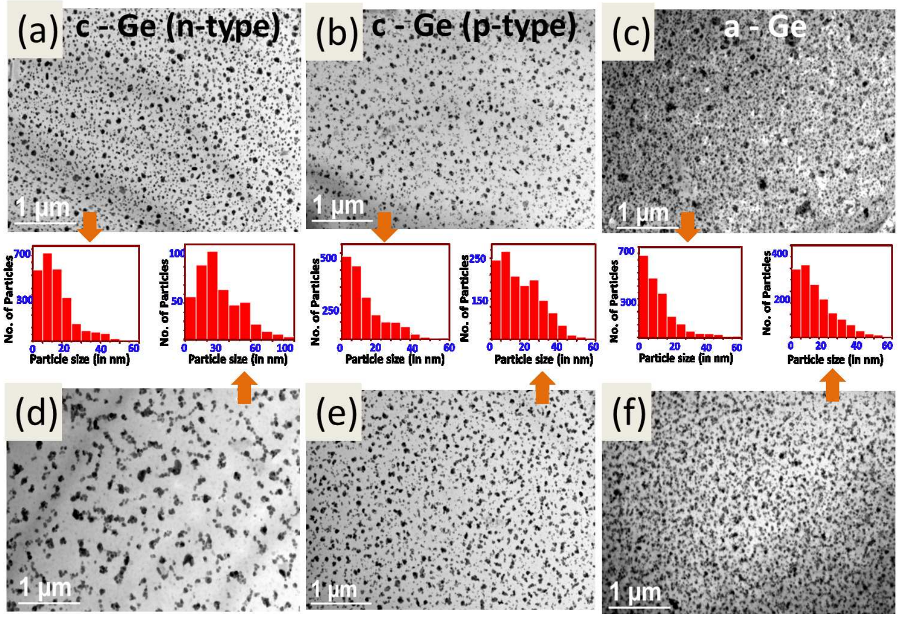

Figure 4.12: *Plan-view TEM images of Ag particles deposited for 30 seconds on (a) n-type c-Ge, (b) p-type c-Ge, (c) n-type a-Ge substrates. (d-f) The same substrates when dipped into water for 3 hours. The corresponding particle size distributions are shown by arrows.*

One can see that the particle enlargement in p-type c-Ge is smaller than that in the n-type c-Ge as the Ostwald ripening is delayed. Thus our observations confirm the occurrence of electrochemical Ostwald ripening in the GDR and particle growth

Substrate	***Water immersion***	***Particle counts***	***Percentage of areal coverage***	***Mean size (nm)***	***Standard deviation (nm)***
c-Ge(n-type)	***Before***	2466	18.63	17.2	9.1
	After	399	11.87	32.1	21.2
c-Ge(p-type)	***Before***	1610	15.55	17.1	13.6
	After	1325	14.25	20.6	10.6
a-Ge(n-type)	***Before***	1895	17.92	16.9	13.6
	After	1340	16.22	20.0	14.2

Table 4.2: *Summary of the results presented in Figure 4.12.*

is the result of a synergetic effect. Similarly, we have deposited Ag particles on an n-type a-Ge substrate for 30 seconds by the GDR and then dipped the same Ag deposited substrate into water for 3 hours. Much less change (Figure 4.12(c), 4.12(f) and Table 4.2) in the size of these Ag particles has been observed as the Ostwald ripening is hindered due to the amorphization which causes an increase in resistivity [110]. These results are summarized in Table 4.2. One can see from this table that the average particle size is increasing at the same time as the percentage of area coverage is decreasing when the substrate is immersed in water, which is a clear case of Ostwald ripening.

4.3 Substrate decomposition in GDR

4.3.1 Experimental

For the synthesis of Ag and Au nanoparticles, without adding any reducing agent two similar ($2mm \times 4mm$) substrates were dipped into aqueous silver and gold precursor solutions (1mM of $AgNO_3$ and $HAuCl_4$) separately and kept for 2 hours in the solution bath then removed and dried in air. After that, the nanoparticles contained substrates were bonded face to face and processed for cross sectional TEM

(XTEM) sample preparation using the standard method of mechanical thinning and Ar ion milling using the precision-ion-polishing system (Gatan, Pleasanton, CA) as described earlier, to analyze in the scanning transmission electron microscope (Model: FEI Tecnai G^2 F30 S-Twin, operating at 300 kV, equiped with a Fischione3000 high angle annular dark field (HAADF) detector).

4.3.2 Result and discussion

The bright-field TEM image (Figure 4.13) showing gold and silver nanoparticles formation on germanium thin film (deposited on Si substrate), where it can be seen that the germanium layer thickness got reduced in both the cases of particle formation and the reduction of Ge layer is more (200 nm to $\sim$ 40 nm) in the case of Ag particle formation than that of Au (200 mn to $\sim$ 198 nm).

Galvanic displacement of metal ions on semiconductors takes place with the donation of valence band or bonding electrons by the semiconductors itself to the metal ions, consequently the semiconductor substrate gets corroded. For the accumulation of Ag or Au on Ge surface no external influence is required and feasibility arises for suitable redox potential of Ge (0.12V). The mechanism is described as [25, 92–94]

$$AuCl_4^- + 3e^- \longrightarrow Au + 4Cl^- \qquad (E^0 = 1.002V)$$

$$Ge \longrightarrow Ge^{4+} + 4e^- \qquad (E^0 = -0.12V)$$

$$Ag^{+1} + e^- \longrightarrow Ag \quad (E^0 = 0.8V)$$

The standard cell potentials (E^0) are with respect to the normal hydrogen electrode (NHE). Positivity of the net cell potential for Au-Ge or Ag-Ge system indicates for no additional reagent requirement.

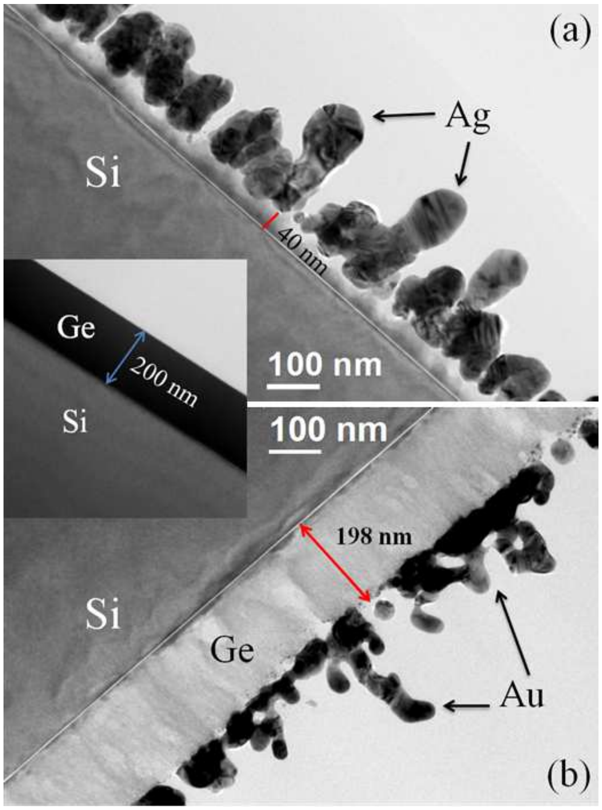

Figure 4.13: *Cross-sectional bright-field TEM images. (a) silver and (b) gold nanoparticles on germanium/silicon surfaces. As grown Ge layer on Si is shown in the inset.*

Detailed EDX analysis reveals that the substrate erosion of Ge by Ag is greater than that of Au, which is evidenced by the corresponding EDX spectra in Figure 4.14. It is visible from Figure 4.14(b) that the spectrum of Ag-Ge system shows a very weak signal of Ge from the area marked by 1 in Figure 4.14(a). In contrast, the spectrum of Au-Ge system in Figure 4.14(c) shows stronger Ge signal from the area marked by 2 in Figure 4.14(a).

The elemental distribution along different interfaces can be further demonstrated by elemental mapping using STEM-HAADF- EDX technique. The elemental mapping (Figure 4.14(d) and Figure 4.14(e) shows that the germanium

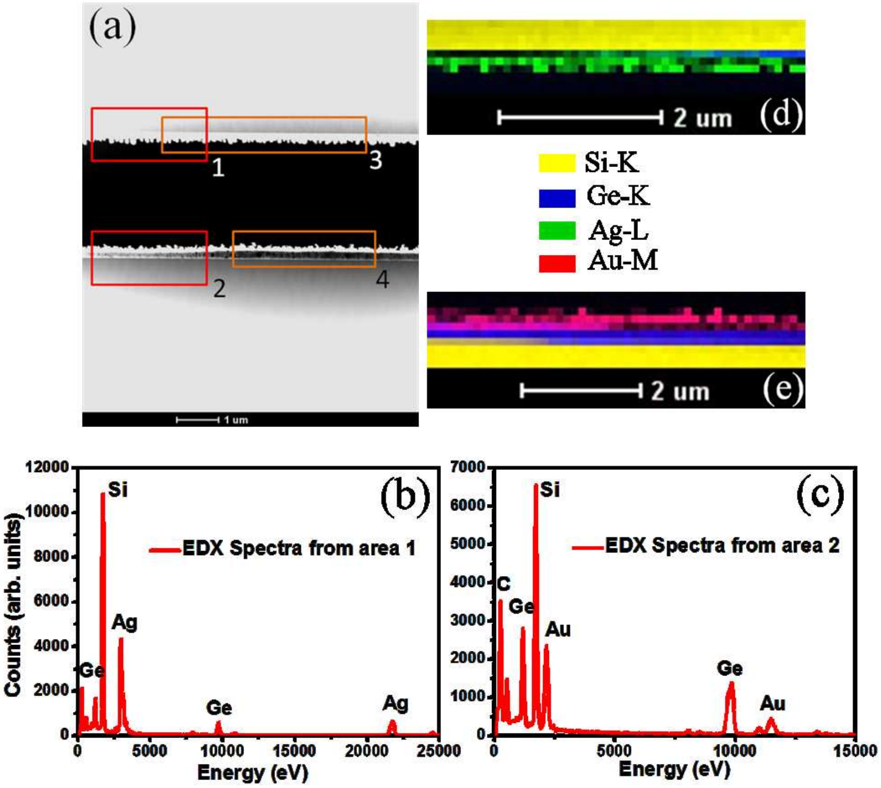

Figure 4.14: *(a) STEM-HAADF image; (b) and (c) EDX spectra from area 1 and 2 marked in (a), respectively; (d) and (e) elemental mapping from area 3 and 4 marked in (a) for Ag-Ge and Au-Ge system, respectively.*

layer in Ag deposition is almost dissolved completely but for Au-Ge a visible layer is still present. Now the greater oxidation state of Au would extract more charges from the Ge to give rise to surpassing corrosion rate than Ag and then we should have thinner Ge layer in Au rather than in Ag. The possibility for lesser erosion in Au-Ge system is that the reducing electrons are supplied by the deposited Au itself. This leads to the autocatalytic behavior of Au in later stage of deposition where the deposition started by the GDR. Once initiated, the reduced Au species serve to catalyze subsequent Au reduction.

4.4 Conclusion

We have studied the growth of silver nanostructures on germanium surfaces and could control the size of the particles on amorphous Ge over crystalline Ge substrate in the GDR. Ag particle growth on the O^+ and Ar^{2+} ion bombarded Ge substrates collectively suggest that the uniform particle growth arises mainly due to (1) an electronic effect related to reduced electron mobility upon surface amorphization and (2) a geometrical effect connected to the Ag atoms trapped on surface defects. This study of the Ag particle growth on different surfaces leads to an insight into the GDR, where an electrochemical Ostwald ripening process has been observed. Particle growth is a result of a synergetic effect. In this way by introducing defects, a controlled growth with desired particle size could be possible in this very simple, convenient and cost-effective synthesis procedure. Again, Ag and Au nanoparticles were deposited on germanium thin film (deposited on Si) by GDR and their TEM and EDX analysis show that the decomposition of Ge layer is lesser in case of Au nanoparticle formation compared to Ag, which indicates the autocatalytic behavior of Au formation on Ge. This study of GDR on ion bombarded amorphized surface and on thin film surface endeavors to look at the galvanic displacement deposition from a different perspective.

Chapter 5

Thermal evolution of nanoparticles on Si surfaces

This chapter includes the wetting, agglomeration, oxidation of nanoparticles on Si surfaces at elevated temperature.

5.1 Introduction

Thermal treatment is an effective way for size and shape modulation on nanoparticles on substrate surface. In this context annealing environment also plays an important role. If we consider thermal oxidation of copper then, cupric oxide (CuO) is a stable oxide of copper, and due to its diverse applications, immense research on CuO nanostructure fabrication have been carried out all over the world. CuO is a p-type semiconductor with a band gap of 1.4 eV [111, 112]. Higher conductivity has been observed in CuO as compared to Cu_2O, although higher carrier mobility has been observed in Cu_2O [113]. However, the higher stability of CuO makes it more applicable. In the recent years, several CuO nanostructure syntheses and their applications have been reported [114–122]. Different shaped CuO nanostructures such as nanowires, nanoplatelets, nanorods, and nanoflowers have been employed as the anode material for lithium ion batteries [114–117], and improved performance has also been observed in composite $CuO - carbon$ nanotube and $CuO - graphene$ systems [118, 119]. CuO nanostructures find promising application in many other fields such as gas sensing, catalysis, and arsenic (As) removal in water purification [120–122]. Such differently shaped CuO nanostructures have been synthesized following different processes such as hydrothermal, chemical precipitation, electrochemical as well as other methods [114–117, 123]. In this context the combination of the GDR and the rapid thermal annealing process provides a simple and quick route for the synthesis of CuO nanostructures on Si surfaces.

CuO has important applications in solar cells. With a suitable band gap, CuO

has a higher theoretical photocurrent density [124]. The practical conversion efficiency for CuO is low, which may be due to its low carrier concentration [125]. Again, the $p-typeCuOn-typeSi$ heterojunction is applicable for solar cells due to their similar electron affinity [126]. The reported open circuit voltage for a $p-CuO/n-Si$ heterojunction solar cell is 0.33 V [127] and after improving the crystalline quality and the interface quality between CuO and Si, an increased open circuit voltage of 0.509 V and a high photocurrent density of 12 mA/cm^2 have been achieved [126]. Therefore, it is important to understand the CuO/Si interface properties. We found that the formation of CuO by the thermal oxidation of Cu nanoparticles on Si surfaces leads to wetting, where no such wetting was observed when the Cu nanoparticles were annealed under a nitrogen atmosphere. This implies that the ambient conditions play an important role in the interface formation. As mentioned earlier, the GDR is categorized in the electroless family, where the nanoparticle deposition is possible without any external reducing agent [25, 92, 93] and the fundamental criterion for such deposition is that it has a net positive electrode potential between the substrate and the deposited element [25, 92, 93]. The standard potential for Cu is 0.34 V and for Si is 0.875 V [41]. Thus the net potential between Cu and Si is 1.215 V, which suggests an easy Cu deposition on Si surfaces. However the insoluble oxide layer on the Si surface prevents the metallization, where the addition of hydrofluoric acid (HF) into the copper solution removes such oxide layers formed on the Si surface and assists the GDR and the complete reaction of Cu deposition on Si takes place in the following way:

$$2Cu^{2+} + Si + 6F^{-} = 2Cu + SiF_6^{2-} \tag{5.1}$$

Since SiF_6^{2-} is water soluble, the GDR proceeds easily. This dissolution of Si in water from the surface as SiF_6^{2-} increases the Si surface roughness during the deposition.

In several studies, copper oxide on different substrates have been grown by the direct thermal oxidation of Cu. Pure copper oxide has been easily formed by thermal annealing on indium tin oxide (ITO) or glass [113]; but copper oxidation on a silicon surface may lead to copper silicidation [128]. Papadimitropoulos et al. have observed the formation of copper silicide at low annealing temperatures, and when the temperature is high, pure copper oxide is formed as the oxidation rate overcomes the silicidation [128]. The thermal oxidation produces both the Cu(I) and Cu(II) oxide depending on the duration and temperature of the annealing process. In thermal annealing of copper, Cu(II) oxide is formed at a higher temperature than the Cu(I) oxide [113]. An anealing study of a deposited Cu_2O film in an oxygen environment also shows the formation of CuO [129]. The general way of formation is Cu to Cu_2O and then CuO but it is possible to form CuO without formation of any intermediate oxide, by embedding H_2 [130]. In our present work, we have studied the oxidation of Cu nanoparticles deposited by the GDR on silicon surfaces at various ambient conditions.

Now as we saw that the substrate supported Cu nanoparticle deposition is important for various application, Ag nanoparticle deposition has also been paid attention for different application. As an example, tuning the Ag particle size and separation, total reflectance of silicon can be reduced, this can considerably enhance the silicon solar cell performance [131]. Previously we have discussed about the deposition of Ag on Ge surface by GDR. Ag nanoparticle can be deposited on the Si surface in a similar fashion as Cu deposition, in presence of HF acid. The silver particle shape and size in the galvanic displacement deposition process can be controlled by adjusting the Ag ion concentration in solution [132] or by modifying the substrate surface as we have discussed earlier. Thermal annealing of the Ag nanoparticles on the Si surface can also influence in their shape and size transformation. TEM and SEM study prove that thermal treatment can provide well separated spherical shaped particle starting from randomly distributed particles. Thus the combination of GDR and thermal treatment for Cu and Ag nanoparticles provides an easy and cost effective way to control their shape and size on substrate surface and at the same time provides an understanding for the evolution of nanoparticles on substrate surface at elevated temperature.

5.2 Role of oxygen in wetting of copper nanoparticles at elevated temperature

5.2.1 Experimental

Copper nanoparticles have been deposited on Si(100) substrates by an easy, one-step GDR. 5 mL of 10 mM CuSO4 (Merck, > 99%) solution was taken in a small petri dish and $200\mu L$ of HF (48% w/v) was added to the solution. Three TEM-ready (3 mm disc and electron transparent) and one 1×1 cm Si substrate were slowly dipped into the solution, kept for 2 min for deposition to occur, then taken out slowly from the solution and dried in air. The Si substrates were prepared for plan-view TEM studies before deposition so that after deposition, the tedious TEM sample preparation procedure (which may affect the loosely bound deposited particles on Si and can change the morphology), was not necessary. The plan-view specimen with Si was prepared in the way described earlier. After the galvanic displacement deposition of Cu on the Si plan-view specimen, measurement was performed in TEM (Model: FEI Tecnai G^2 F30 S-Twin, operating at 300 kV, equiped with a Fischione3000 high angle annular dark field (HAADF) detector). After the TEM analysis, the same samples were transferred to a rapid thermal annealing unit (model: JETFIRST100 jipelec) and annealing was performed in air, oxygen and nitrogen atmospheres, one by one. The rapid thermal annealing was performed at 500^oC for 1 min (a heating ramp rate of $10^oC/s$) was used for all three different samples. Before and after the thermal annealing, the structural analysis was done using the SAED operation in the TEM as well as by the X-ray diffraction (model: Rigaku TTRAX3, Cu Kα ($\lambda = 1.5418\mathring{A}$)). To understand the interface and thermal evolution in different environments, cross-sectional TEM studies were also carried out.

5.2.2 Result and discussion

Copper deposited on silicon surfaces by the GDR were extensively examined by TEM. The planview bright field TEM image in Figure 5.1(a) and the STEM-HAADF image in Figure 5.1(b) show the deposited copper nanoparticles on a silicon substrate. The elemental composition is presented by the EDX mapping. Figure 5.1(e) and Figure 5.1(f) show the silicon (yellow) and copper (blue) elemental mapping, respectively, collected from a region marked by an orange rectangle in the STEM-HAADF image in Figure 5.1(b). The thermal oxidation was performed in a rapid thermal annealing system at 500^oC for 1 min. We have analyzed the phase of the as-deposited material and the samples annealed under oxygen atmosphere by SAED operation. The diffraction pattern of the as-deposited sample (Figure 5.2(a)) shows some clear bright spots and faint rings. The bright spots

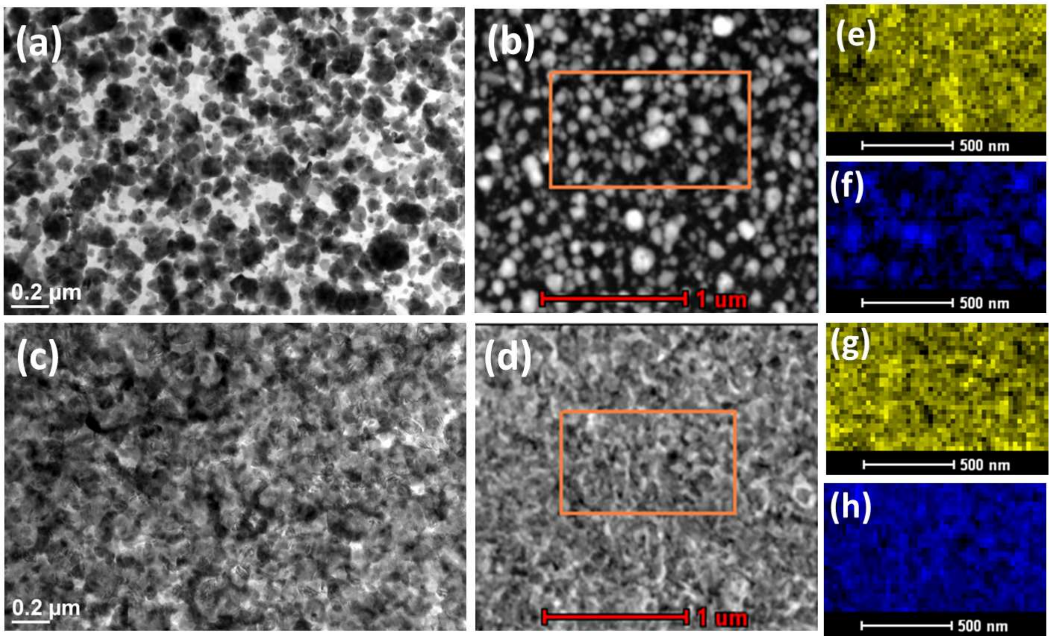

Figure 5.1: *Plan view (a) TEM image (b) STEM-HAADF image of as-deposited copper nanoparticles on Si. Plan view (c) TEM image (d) STEM-HAADF image after the same nanoparticle substrate was annealed at* 500^oC *for 1 min under oxygen atmosphere. EDX elemental image (silicon (yellow) and copper (blue)): (e) and (f) collected from the orange rectangular area in Figure (b); (g) and (h) collected from the orange rectangular area in Figure (d).*

were indexed as crystalline silicon in the [100] zone axis. The faint ring patterns correspond to the copper cubic structure along with the presence of Cu_2O. The presence of Cu_2O is due to oxidation of the Cu nanoparticle from air exposure. The diffraction pattern of the annealed sample at oxygen atmosphere shows bright ring patterns with the bright spots of crystalline silicon in [100] zone axis (Figure 5.2(b)). The bright ring pattern is indexed as the monoclinic (a = 4.682, b = 3.424, c = 5.127) CuO structure. The presence of Cu_2O is also observed but there is no presence of Cu, indicating a complete oxidation. The XRD pattern of the as-deposited Cu nanoparticles on the Si (Figure 5.3(a)) shows the peaks at 43.5^o

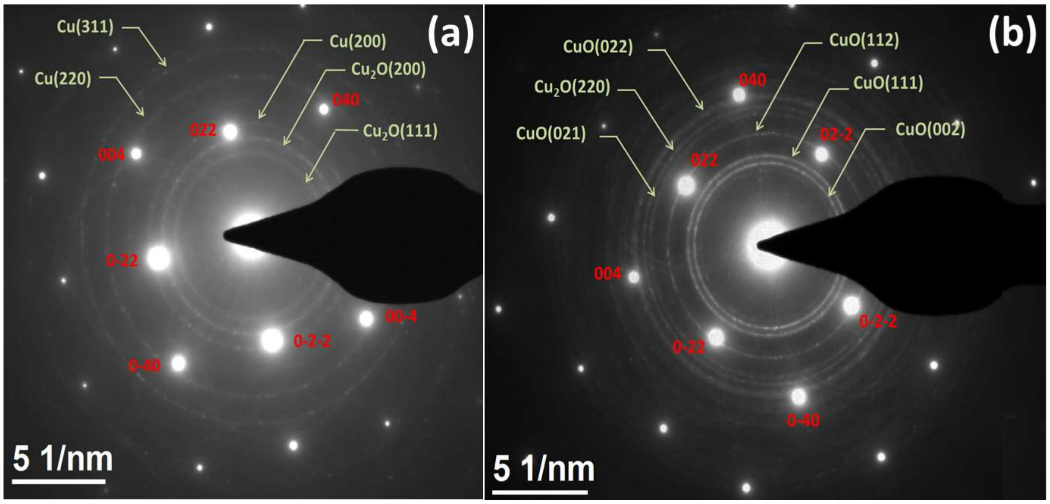

Figure 5.2: *SAED pattern of (a) as-deposited copper nanoparticles on the silicon substrate (b) the same sample annealed at* 500^oC *in oxygen ambient. The bright spot (indexed in red) are from single crystal silicon and the ring patterns (indexed in green) are from polycrystalline* Cu, Cu_2O *or* CuO

and 50.7^o which correspond to the Cu(111) and Cu(200) planes [JCPDS No. 04-0836]. The XRD pattern of the annealed sample under oxygen atmosphere (Figure 5.3(b)) shows that the copper peak disappeared and the new peaks at 35.7^o and 38.9^o appear that correspond to the (111) and (200) planes of CuO, respectively [JCPDS No. 80-1916].

The thermal annealing of thin films on a substrate leads to the formation of islands, which is the consequence of the Gibbs-Thomson effect for the energy minimization [30]. There are different theoretical explanations regarding the mechanism of particle agglomeration. In general, a copper thin film is agglomerated via grain boundary grooving mechanism during thermal annealing [133, 134]. Further annealing results in Oswald ripening [135, 136], where the atoms diffuse from smaller to larger nanoparticles and form larger copper clusters. The agglomeration of copper particles was observed in the earlier observations during thermal

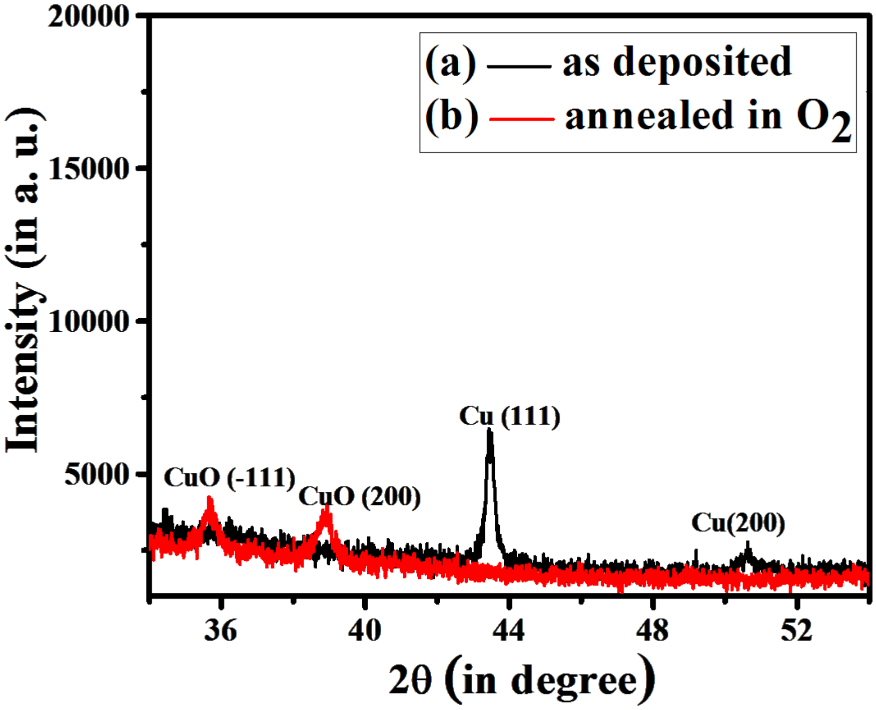

Figure 5.3: *X-ray diffraction pattern for the (a) as-deposited copper nanoparticles on silicon substrate and (b) when the copper nanoparticle substrate is annealed under oxygen at* 500^oC *for 1 min.*

annealing either in vacuum or in inert ambient where the presence of oxygen was excluded. However, oxidation plays an important role in thermal evolution of the copper thin film. The formation of oxide impedes the agglomeration of copper film during thermal annealing [133]. It is also observed that when the substrate or the Cu film is exposed to air, the agglomeration is hindered [135]. Such retardation in copper agglomeration is caused as the oxidation in the grain boundaries retards the diffusion in the grain boundaries and also affects the grain boundary grooving [135, 137, 138]. Again the agglomeration has also been observed during the oxidation of copper nanoparticles on glass substrates [139]. Similar agglomeration has been found when cuprous oxide deposited on glass, copper or tin oxide-coated glass substrates, is annealed in oxygen to form CuO [129, 140]. When Cu or Cu_2O in powder form is annealed in an oxygen environment to form CuO, particle agglomeration is also observed [141]. Thus, in general, it can be said that the copper thin film tends to agglomerate during thermal annealing at high temperatures and oxidation has a strong influence.

We have studied the annealing of copper nanoparticles on silicon surfaces under various atmospheric conditions. The copper-containing substrate, annealed in an oxygen environment at 500^oC for 1 min, is presented in the TEM image in Figure 5.1(c) and STEM-HAADF image in Figure 5.1(d) (where the images of the as-deposited Cu nanoparticles on the Si surface are presented in Figure 5.1(a) and Figure 5.1(b), respectively). We observed that for copper nanoparticles on silicon substrates annealed in oxygen environment, the particles are wetted on the silicon surface. Figure 5.1(g) and Figure 5.1(h) present the silicon and the copper elemental mapping, respectively, collected from the orange square in the STEM-HAADF image of the annealed substrate (Figure 5.1(d)). If we compare Figure 5.1(f) (the as-deposited) and Figure 5.1(h) (annealed at oxygen), one can see the presence of elemental copper is discontinuous for the as-deposited substrate, whereas it is almost continuous when annealed in the oxygen environment. This supports the wetting on Si surfaces during the formation of CuO by the thermal oxidation.

The wetting during formation of CuO on the Si surface is more prominently visible from the cross-sectional TEM images. Figure 5.4(a) and Figure 5.4(c) are the cross-sectional TEM and STEM-HAADF images of the as-deposited Cu nanoparticles on the Si surface and Figure 5.4(b) and Figure 5.4(d) are the cross sectional

TEM and STEM-HAADF images when annealed in an oxygen environment at 500^oC for 1 minute. The as-deposited Cu nanoparticles are quiet distinct, where a continuous film is formed during the thermal oxidation of Cu. The elemental mapping of Cu (Figure 5.4[1] and Figure 5.4[4]), Si (Figure 5.4[2] and Figure 5.4[5]), and composite of them (Figure 5.4[3] and Figure 5.4[6]) have been presented which were collected from the area outlined by the orange rectangle in Figure 5.4(c) and Figure 5.4(d).

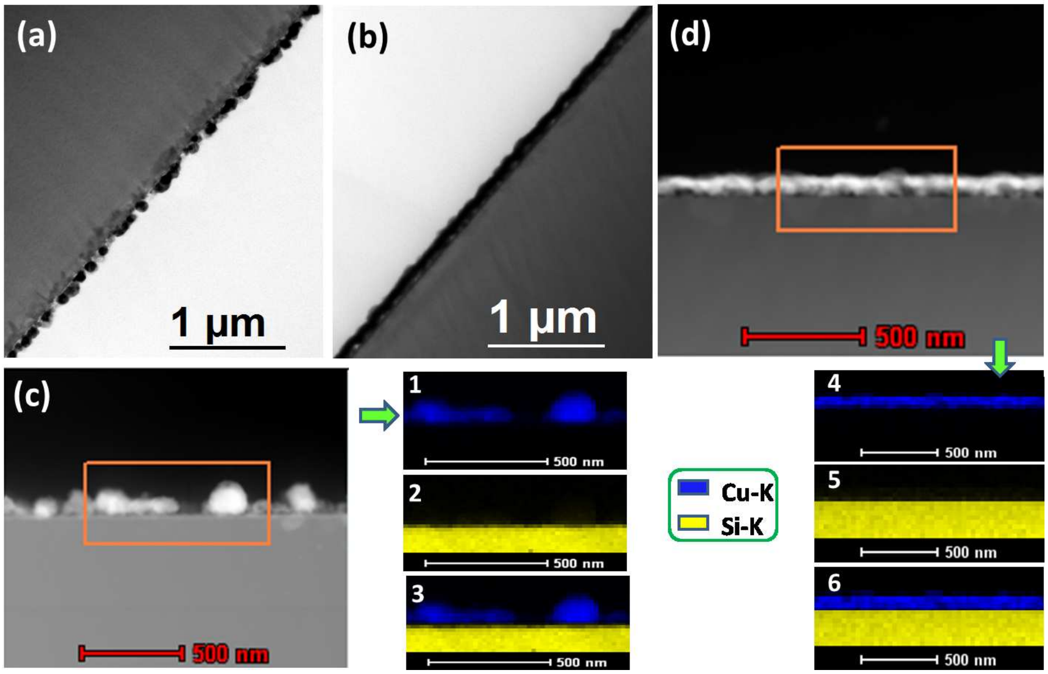

Figure 5.4: *(a),(b) Cross-sectional bright field TEM images and (c),(d) STEM-HAADF images of as-deposited and annealed at* 500^oC *in oxygen ambient copper nanoparticles on silicon substrates, respectively. The elemental mapping of Cu (1 and 4), Si (2 and 5), and the composite thereof (3 and 6) collected from the orange rectangular region of STEM-HAADF images (c) and (d), respectively.*

We have extended our study by measuring the elemental line profile using STEM-HAADF-EDX, as presented in Figure 5.5. Two elemental line profiles for Cu, O and Si have been acquired for the as-deposited sample (Figure 5.5(a)). These profiles show a higher Cu intensity when the electron beam (along the line) passes through the particle and significantly less intensity when it does not pass through any particle.

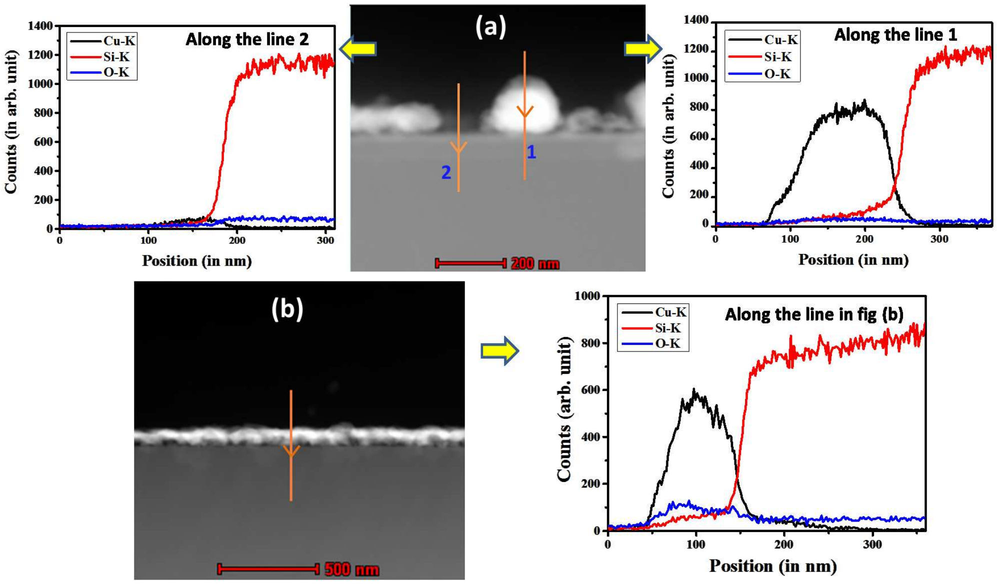

Figure 5.5: *Copper, silicon and oxygen elemental line profiles collected from the region indicated by the arrows in the STEM-HAADF images of (a) as-deposited copper nanoparticles and (b) copper nanoparticles oxidized to CuO on the silicon substrate.*

The elemental line profile for the same sample annealed in an oxygen environment at 500^oC for 1 minute shows high copper intensity as the electron beam passes through the film (Figure 5.5(b)). We have taken several such line scans on annealed samples and the result was the same all the cases. The higher oxygen intensity in the Cu film region also indicates the formation of CuO as compared to that found in the as-deposited sample. A comparative study has been performed to observe the wetting behavior during the thermal annealing of Cu nanoparticles

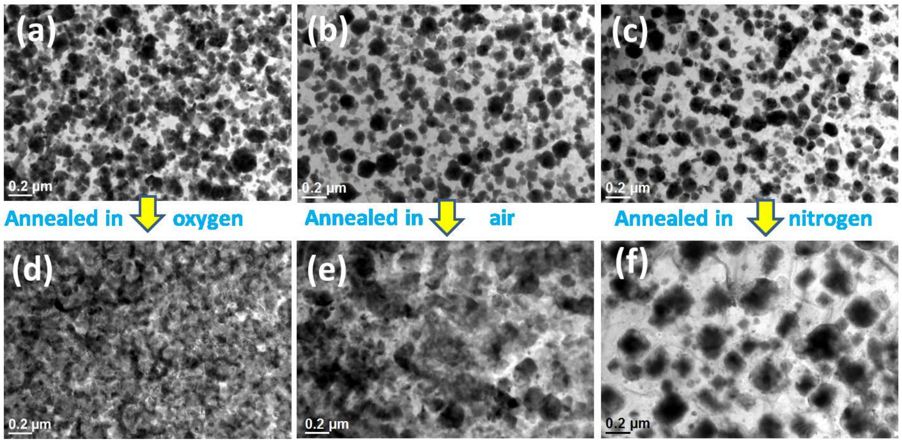

Figure 5.6: *(a-c) Cu nanoparticles on Si substrates deposited via the GDR, and (d-f) when the same substrates were annealed in oxygen, air, nitrogen, respectively*

	Percentage area coverage
As-deposited	63.8
Annealed in N_2	43.3
Annealed in Air	92.4
Annealed in O_2	97.6

Table 5.1: *Area coverage (as presented in Figure 5.6) for samples annealed under different ambient conditions.*

on Si surfaces at the same temperature (500^oC) and with the same annealing duration (1 min) but at different ambient conditions. Figure 5.6(a-c) reports on the results of as-deposited Cu nanoparticles on the silicon substrates deposited by the GDR conducted for 2 min. Those same substrates are annealed under oxygen, air and nitrogen conditions and are presented in Figure 5.6(d-f), respectively. One can clearly observe from the TEM images when the Cu particle-containing substrates are annealed under nitrogen atmosphere agglomeration occurs, but when they are annealed under oxygen or in air, wetting occurs. The corresponding area coverage (in percentage) of the annealed substrate under different environmental conditions is presented in Table 5.1. Almost the complete area is covered ($\approx 98\%$) due to wetting when the substrate is annealed in oxygen. We observed from the SAED and XRD analyses that in the process of annealing at (500^oC) in oxygen, Cu particles were transformed into CuO. This is similar to the annealing of the Cu particles under the same time when annealed in air, which also leads to the formation of CuO observed by the SAED pattern (Figure 5.7).

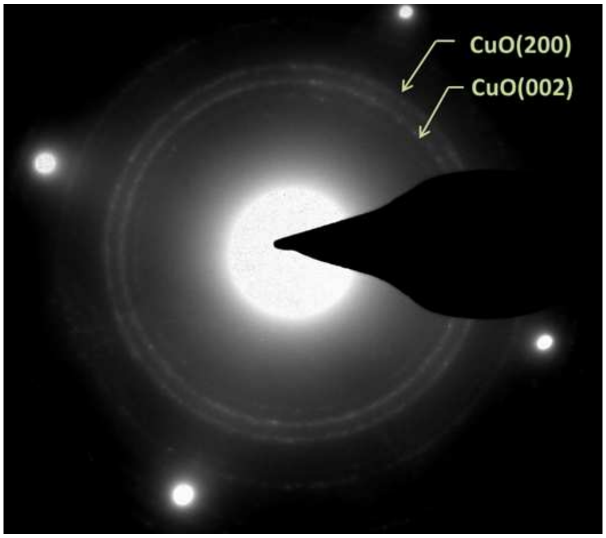

Figure 5.7: *SAED of the sample annealed in air at* 500^oC *for 1 min*

We observed wetting under both the circumstances. In contrast, when annealing in nitrogen atmosphere, we observe agglomeration. The particle distribution is shown in Figure 5.8 and the summary is presented in the Table 5.2.

For the samples annealed in the nitrogen environment, the Cu phase remains unchanged as we can see from the XRD pattern in Figure 5.9. This is consistent with the observation of Li et al.[136] that the annealing of Cu nanoparticles in nitrogen environment does not change the Cu crystallinity. During the formation

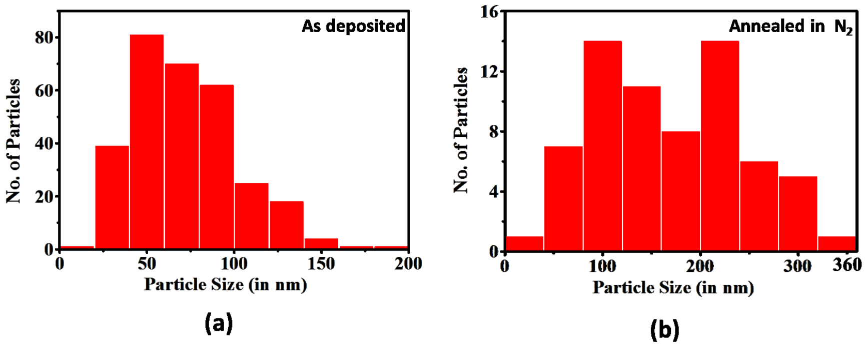

Figure 5.8: *Cu nanoparticle distribution on a Si surface for (a) as-deposited and (b) annealed in nitrogen atmosphere.*

	As-deposited	**Annealed in N_2**
Number of particles	303	67
Mean diameter (nm)	72.4	167.6
Standard deviation (nm)	31.3	74.9

Table 5.2: *Summary of the particle distribution presented in Figure 5.8.*

of copper silicide, agglomeration also occurs [142]. Thus the oxidation of copper nanoparticles on silicon leads to wetting rather than agglomeration.

The cross-sectional TEM images of the as-deposited and annealed under nitrogen and oxygen are presented in the Figure 5.10. We observe larger particle formation due to the agglomeration when annealed in a nitrogen environment and a continuous film formation due to wetting when annealed in an oxygen environment. The wetting phenomena of nanoparticles on a substrate surface is a consequence of the negative interface energy between the particles and the substrate. This was reported by Yang et al. in their study of platinum nanocrystals on silica

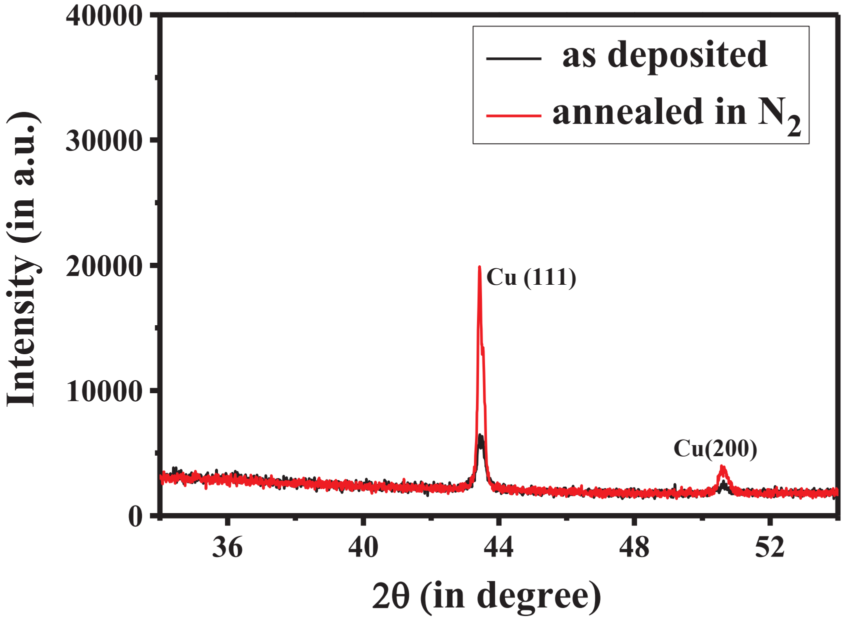

Figure 5.9: *XRD patterns of the as deposited and the* N_2 *environment annealed samples.*

surfaces [33]. In another study it was observed that when copper nanoparticles are deposited on silicon surfaces and oxidized at high temperatures to form CuO, the shape of the CuO particle appeared lamellar [143]. The thermal annealing in the oxygen environment may also produce SiO_2 at the silicon-copper surface that may affect the interface energy, but as the Cu particles are spread all over the surface, the oxygen exposure of the Si surface is reduced. Again, when the copper film is oxidized to form CuO, the film thickness is increased; such a thickness increment is due to the lattice expansion as the cubic copper lattice is transformed into a monoclinic CuO structure [113, 144]. On the other hand, the surface energy of the CuO thin film is greater than that of the Cu_2O thin film [145]. Thus combining the lattice expansion and the surface energy increment, wetting takes place during

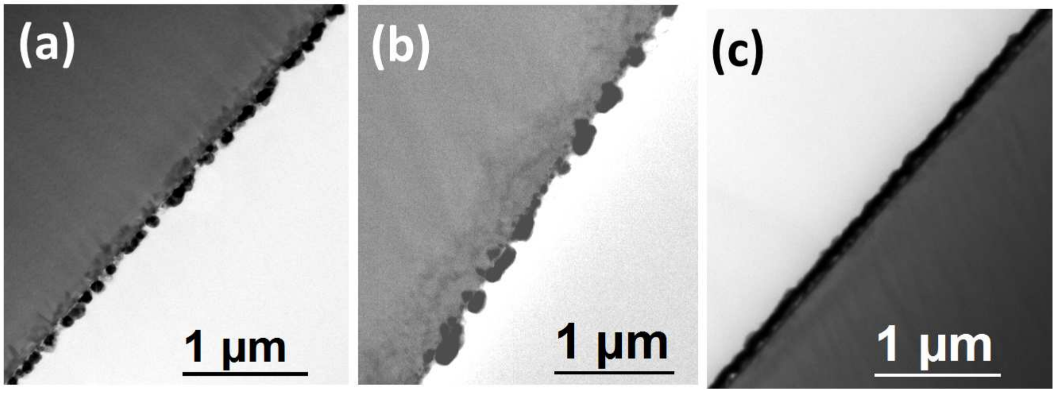

Figure 5.10: *(a) As-deposited Cu nanoparticles on Si and when annealed at* 500^oC *for 1 min in (b) nitrogen and (c) oxygen environment.*

formation of CuO on the silicon surface. The wetting which occurs during the formation of CuO suggests a strong interaction between the CuO and SiO_2/Si surfaces.

5.3 GDR and RTA in size/shape controlling silver nanoparticles

5.3.1 Experimental

We have deposited silver nanoparticle on Si substrate by the GDR and performed rapid thermal annealing (RTA). The as deposited and the annealed silver nanoparticles on the silicon surface has been studied by the transmission electron microscopy (TEM) in cross-sectional geometry and scanning electron microscopy (SEM). For silver nanoparticle deposition a 5 mL of 10 mM silver nitrate solution was prepared in a small beaker and 200 μL of hydrofluoric acid (HF 48% GR) added into it. Now Si substrate was slowly dipped into the silver solution and kept for 2 minutes for deposition to take place. Then the substrate was taken out of the solution and dried at room temperature. The silver deposited Si substrate was annealed at 500^oC in RTA system (JET-FIRST100, Jeplec) at a heating ramp rate of $10^oC/sec$ in nitrogen environment. The annealing was continued for 60 seconds. TEM cross sectional specimen was prepared with the as deposited and annealed substrate in the way described earlier and characterized in TEM (Model: FEI Tecnai G^2 F30 S-Twin, operating at 300 kV, equiped with a Fischione3000 high angle annular dark field (HAADF) detector).

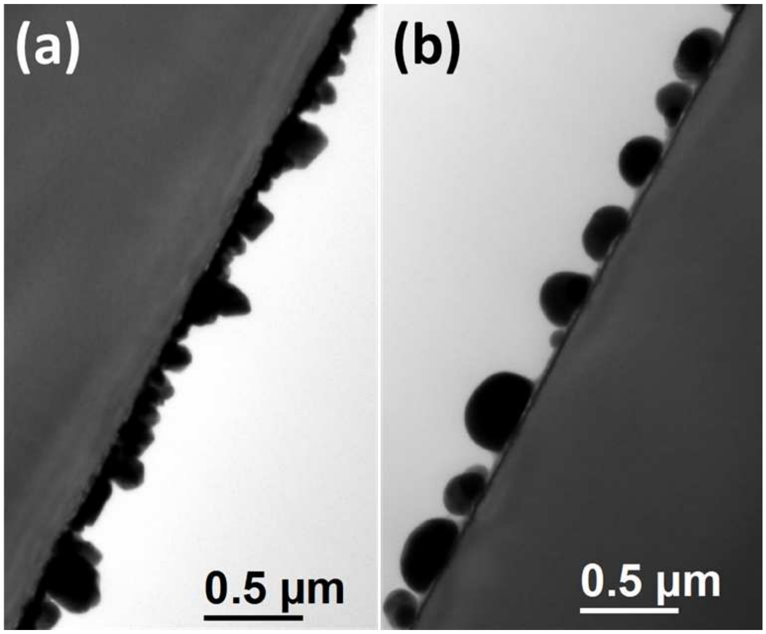

Figure 5.11: *Ag nanoparticles on Si surface (a) as deposited, (b) annealed at* 500^oC*.*

5.3.2 Result and discussion

Since, for the galvanic displacement deposition on Si, HF is required to be added and the complete reaction for Ag deposition on Si takes place in the following way [132, 146]

$$2Si + 6F^- \rightarrow SiF_6^{2-} + 4e^-$$

$$Ag^{+} + e^{-} \rightarrow Ag$$

The formation of silver nanoparticles on Si surface has been shown by the cross sectional bright field TEM image (Figure 5.11(a)). The Ag, Si and the composite elemental mapping from the yellow colored rectangular area of the STEM-HAADF image of as deposited silver nanoparticle on silicon substrate, has been presented in the Figure 5.12(a).

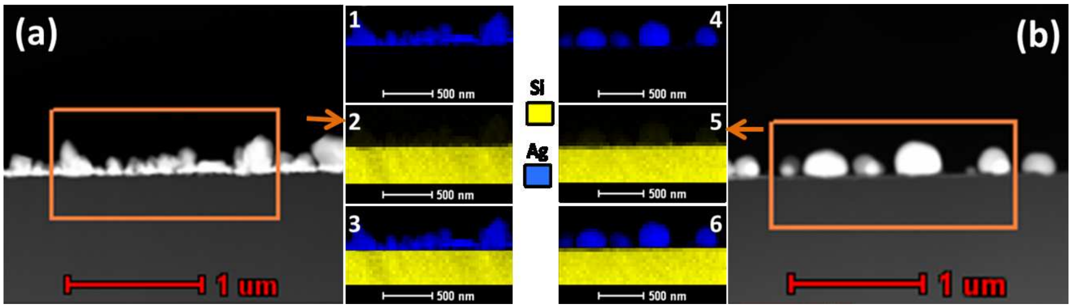

Figure 5.12: *Elemental mapping of Ag (1, 4), Si (2, 5), overlay of Ag and Si (3, 6) from the rectangular area of the (a) as deposited and (b) annealed samples using STEM-HAADF-EDX technique.*

The elemental mapping assured that Ag particles have been formed on the Si surface. One can see that the shape of the Ag particles is irregular. The growth of Ag particles occurred following Volmer-Weber growth mode [27], where the islands form initially and the enlargement of the island gives rise to continuous film deposition as depicted in Figure. 5.13(a). The thermal annealing has been performed at $500^{o}C$ which is below the melting point of the silver and silicon. The bright field TEM image of the annealed Ag nanoparticles deposited Si substrate has been shown in the Figure 5.11(b). The Ag, Si and the composite elemental mapping from the yellow colored rectangular area of the STEM-HAADF image of the annealed sample, has been presented in the Figure 5.12(b). One can observe that

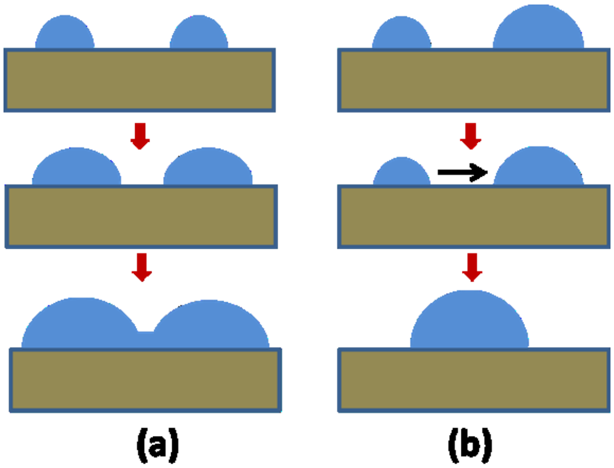

Figure 5.13: *Schematic showing different steps of larger particle formation.*

due to the thermal annealing the shape of the Ag nanoparticles on the Si surface has been transformed into spherical shaped and they are also well separated. The changed spherical shape of the Ag particles appears because of the Gibb-Thomson effect of surface free energy minimization during the thermal treatment [30]. One

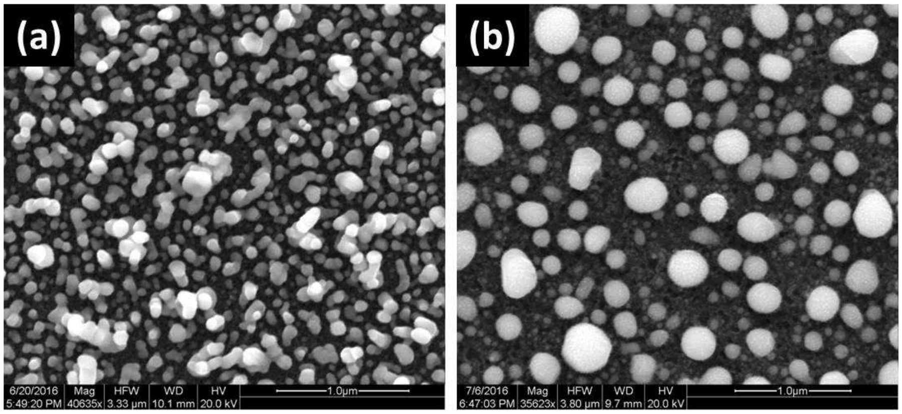

Figure 5.14: *SEM images of the Ag nanoparticles on Si substrate (a) as deposited (b) annealed at* 500^oC.

can see that after the annealing, Ag particles are well separated (Figure 5.14(b)), this arises due to the irregular shape of the as deposited Ag particles. The other reason is the Ostwald ripening (Figure. 5.13(b)), where the atomic species from the smaller particles move toward the bigger particles and make them even bigger [135]. Thus utilizing the GDR and rapid thermal annealing well separated round shaped larger silver nanoparticles on silicon substrate can be achieved in a quick and easy way.

5.4 Conclusion

We have investigated the role of oxygen in wetting of Cu nanoparticles on silicon (100) substrates deposited by the GDR using XRD, TEM and EDX. The rapid thermal annealing in oxygen atmosphere at 500^oC shows the formation of monoclinic CuO. Annealing under nitrogen environment does not convert the copper to any other phase. Annealing in nitrogen environment leads to agglomeration due to the surface energy minimization. Oxidation of the copper nanoparticles on the silicon surface by rapid thermal annealing shows that during the oxidation wetting occurs rather than agglomeration. The lattice transformation as well as the surface energy modification during the CuO formation by thermal oxidation of Cu nanoparticles on the silicon surface leads to the wetting. Such wetting implies a strong interaction between CuO and SiO_2/Si surfaces. This study may be useful to understand and improve the efficiency of $p-CuO/n-Si$ heterojunction solar cells. Again thermally induced Gibbs-Thomson effect and Ostwald ripening process provide size and shape control of nanoparticles as we witnessed for the study of thermal evolution of Ag nanoparticles on Si surface. So the thermal evolution of nanoparticle can be utilized for getting well separated particle distribution or a smooth film on substrate surface depending on choice of implementation.

Chapter 6

Summary

This chapter summarized different findings of this thesis work.

Beside the broadening of research in nanoscience and nanotechnology over the past few decades, the assembling of nanostructures on solid surfaces has become an integral part of it. The nanoparticle deposition has been proven to be effective for sensing devises, enhancing solar cell efficiency and many other applications. In this context the GDR is a feasible and efficient deposition technique. In comparison with the other electroless depositions, namely the autocatalytic and substrate-catalytic deposition, the galvanic displacement deposition is more advantageous as it does not require any reducing agent that could eventually leads to contamination free film growth. The GDR even surpasses the conventional gas deposition in few aspects, like selectivity, three dimensional nanostructure growth. The structure of nanoparticles plays a important role to determine its characteristics, individually and as well as on substrate surface. Thermal treatment of substrate supported nanoparticles thus also attracts enough attention. Thermal evolution of nanomaterials on substrate surface may improve the substrate adhesion, conduct phase separation or may remove residual oxide. If we look at the structural transformation due to the thermal treatment, depending upon surface energy, intermixing, time scale of temperature, two general mechanisms, viz. agglomeration and wetting assist such advantageous features, said earlier. The favorable process is the agglomeration but wetting may occur under different conditions.

Now the GDR is fast process as it proceeds in a charge exchange way by oxidation and reduction. In the present thesis work the controlled film thickness achieved in the GDR was demonstrated at the same time implementation of GDR in other cases and also thermal treatment for obtaining different shaped nanostructure was taken into account.

In chapter 1, an acquaintance of GDR as a part of the nanoparticle deposition technique has been given. The nanopartticle synthesis procedures, evolution of nanoscience and contribution of galvanic displacement deposition have been discussed. Along side the difficulties in probing the nanomaterial, technological advancements, different nanomaterial characterization tools were elaborated. The importance of thermal evolution of nanomaterial on substrate surface was also considered. The parameters determining the shape of the nanoparticles on substrate surface during thermal annealing and theoretical modelling have been illustrate in brief. At the end, an outlook of this thesis work has been given.

In chapter 2, different experimental technics that is in utilization of this thesis work, have been described. As TEM is an inseparable part of nano probing technique, specially for the structural and elemental characterization, in this thesis work the TEM and its different associated techniques have been utilized extensively. The basic principle and different operation of TEM have been elaborated in details. Where cross section and plan-view of substrate supported nanopartcles and their preparation processes, the implementation of SAED for phase determination of nanomaetrial, site selected elemental analysis by STEM-HAADF technique with line profile and spectrum imaging have been elucidated. For particle size distribution and initial structural information implementation of SEM has been shown. As a non-destructive technique, the operation of AFM has also been included. For the thermal evolution of the nanoparticles on substrate surface an RTA system has been used, so its small depiction has been provided.

In chapter 3, different preliminary aspects of GDR have been discussed. In this chapter classification of electroless deposition, advantages of GDR over the other elecroless depositions and different controlling parameter of the GDR have been shown. Growth mode in the GDR has been disclosed to understand the three dimensional nanostructure growth by this deposition method. Possibilities of semiconductor surface nanopatterning by the GDR has also been cast light on. **In chapter 4**, the insight of the GDR has been investigated. Galvanic displacement deposition of Ag nanoparticle has been conducted on crystalline and ion bombarded amorphous Ge surfaces. TEM observation showed a continuous particle growth on the ion bombarded surface in comparison with the crystalline surface. Since the silver deposition bath environment also satisfies the conditions of electrochemical Ostwald ripening, we introduce the idea of occurrence of electrochemical Ostwald ripening in GDR. As the particles deposited by galvanic displacement do not have equal size and the bigger particle possesses a partial negative charge compared to the smaller particles; in the Ostwald ripening mechanism, ions are deposited on the bigger particles accepting electrons from the smaller particles sitting near them, making ion dissolution and size reduction of the smaller particles. Occurrence of electrochemical Ostwald ripening in GDR makes irregular shaped particles on crystalline Ge surface but in case of ion bombarded Ge, the charge transfer and hence the Ostwald ripening is hindered, thus a regular shaped and continuous particle distribution is obtained. To get better experimental evidence of occurrence of Ostwald ripening in GDR, after galvanic displacement deposition of Ag particles on Ge substrate, the particle contained substrate was immersed in water. Under this circumstance GDR can not occur, so the only possibility remains is Ostwald ripening. It was observed that for the crystalline Ge surface, particle enlargement occurs at the cost of smaller particles that ensures the Ostwald ripening. For the ion bombarded Ge surface particles remain almost unchanged as the Ostwald ripening is seized by lack of charge transfer through the substrate due to amorphization. The substrate decomposition in GDR has also been investigated. To find the amount of corrosion in the GDR, initially Ge film was deposited on Si substrate, and then Ag and Au were deposited separately. It was observed that the substrate decomposition in Au is very less, while sufficient amount of Ge film was corroded in Ag deposition. This comparison provide the autocatalytic nature of Au deposition int the solution bath. The study of metal nanoparticle deposition on the ion bombarded substrate and on thin film collectively provides a control achieving in the GDR.

In chapter 5, the thermal evolution of nanoparticles on substrate surface has been presented. Using the GDR, at first Cu nanoparticles were deposited on Si substrate, then this Cu particle contained was annealed RTA unit in different environment. When the Cu nanoparticles were annealed in N_2 atmosphere, agglomeration occurs which is thermodynamically favorable and governed by Gibbs's energy minimization principle. When the Cu nanoparticles were annealed in O_2 atmosphere, wetting occurs rather than agglomeration. SAED and XRD analysis show that the Cu phase is transformed into CuO phase and when annealing was performed in N_2 atmosphere the Cu phase remained unchanged. Due to the lattice transformation and the surface energy modification in CuO formation for the O_2 atmosphere annealing of the Cu nanoparticles on Si surface lead to such wetting. Thermal evolution of Ag nanoparticles, deposited by GDR on Si surface has also been studied. It has been observed that starting from random shaped Ag particle, by the rapid thermal annealing in N_2 atmosphere, a well separated and round shaped particle distribution can be achieved. Thus the combination of GDR and thermal treatment can provide formation nanoparticles of different shape and size on solid surface.

During this thesis work, we have learned that the GDR is a useful technique for selective deposition of metal nanoparticles on substrate surface. The study of the GDR on ion bombarded surface provides a way to control the growth rate. The occurrence of electrochemical Ostwald ripening was established in this study. This may be implemented in formation of different faceted nanostructure formation on substrate surface. The substrate decomposition in GDR is an important way for semiconductor surface nanostructuring. The implementation of GDR and subsequent thermal treatment can be effective way to control shape and size of nanoparticles on substrate surface. Wetting and dewetting may happen depending on different phase formation. In this way, by this thesis work a little effort was given towards the advancement of knowledge.

Bibliography

[1] Siegel, R. *Nanophase Materials, in Encyclopedia of Applied physics 11th ed.* Weinheim: VCH, (1994).

[2] Jones, A. *Royal Society Open Science* **3**(12), 160221–160238 (2016).

[3] Kumar, P., Robins, A., Vardoulakis, S., and Britter, R. *Atmospheric Environment* **44**(39), 5035–5052 (2010).

[4] Strambeanu, N., Demetrovici, L., and Dragos, D. In *Nanoparticles' Promises and Risks*. Springer (2015).

[5] Sciau, P. *Nanoparticles in Ancient Materials: The Metallic Lustre Decorations of Medieval Ceramics*, volume 115. INTECH Open Access Publisher, (2012).

[6] Sharma, V., Park, K., and Srinivasarao, M. *Materials Science and Engineering: R: Reports* **65**(1), 1–38 (2009).

[7] Jones, A., Köhler, M., Ysard, N., Bocchio, M., and Verstraete, L. *Astronomy & Astrophysics* **602**, A46–A49 (2017).

[8] Kruis, F. E., Fissan, H., and Peled, A. *Journal of Aerosol Science* **29**(5), 511–535 (1998).

[9] Obaidat, I. M., Issa, B., and Haik, Y. *Nanomaterials* **5**(1), 63–89 (2015).

[10] STATNANO. `http://statnano.com/publications/4144` url date 05-12-2017.

[11] Dey, P., Nath, T., and Taraphder, A. *Applied Physics Letters* **91**(1), 012511–012514 (2007).

[12] Wang, T., Zhang, Z., Liao, F., Cai, Q., Li, Y., Lee, S.-T., and Shao, M. *Scientific Reports* **4**, 1–9 (2014).

[13] Liu, Y., Zi, W., Liu, S. F., and Yan, B. *Solar Energy Materials and Solar Cells* **140**, 180–186 (2015).

[14] Baia, M., Toderas, F., Baia, L., Popp, J., and Astilean, S. *Chemical Physics Letters* **422**(1), 127–132 (2006).

[15] Markelonis, A. R., Wang, J. S., Ullrich, B., Wai, C. M., and Brown, G. J. *Applied Nanoscience* **5**(4), 457–468 (2014).

[16] Yuan, Z., Dryden, N. H., Vittal, J. J., and Puddephatt, R. J. *Chemistry of Materials* **7**(9), 1696–1702 (1995).

[17] Narayan, R. J. *Diamond and Related Materials* **14**(8), 1319–1330 (2005).

[18] Kong, Y., Yu, D., Zhang, B., Fang, W., and Feng, S. *Applied Physics Letters* **78**(4), 407–409 (2001).

[19] Liu, R. and Sen, A. *Chemistry of Materials* **24**(1), 48–54 (2011).

[20] Zhang, Z., Liao, F., Ma, S., Gao, S., and Shao, M. *Surface and Interface Analysis* **47**(3), 398–402 (2015).

[21] Sivakov, V., Andrä, G., Gawlik, A., Berger, A., Plentz, J., Falk, F., and Christiansen, S. *Nano Letters* **9**(4), 1549–1554 (2009).

[22] Wang, T., Hu, F., Ikhile, E., Liao, F., Li, Y., and Shao, M. *Journal of Materials Chemistry C* **3**(3), 559–563 (2015).

[23] Ferralis, N., Maboudian, R., and Carraro, C. *The Journal of Physical Chemistry C* **111**(20), 7508–7513 (2007).

[24] Magagnin, L., Maboudian, R., and Carraro, C. *Thin Solid Films* **434**(1), 100–105 (2003).

[25] Magagnin, L., Maboudian, R., and Carraro, C. *The Journal of Physical Chemistry B* **106**(2), 401–407 (2002).

[26] Mieszawska, A. J. and Zamborini, F. P. *Chemistry of Materials* **17**(13), 3415–3420 (2005).

[27] Aizawa, M., Cooper, A. M., Malac, M., and Buriak, J. M. *Nano Letters* **5**(5), 815–819 (2005).

[28] Pinkhasova, P., Chen, H., Sukhishvili, S., Du, H., et al. *RSC Advances* **3**(39), 17954–17961 (2013).

[29] Prévot, G., Nguyen, N. T., Alloyeau, D., Ricolleau, C., and Nelayah, J. *ACS Nano* **10**(4), 4127–4133 (2016).

[30] Bonzel, H. P. *Physics Reports* **385**(1), 1–67 (2003).

[31] Baldwin, M., Chidambaram, P., and Edwards, G. *Metallurgical and Materials Transactions A* **25**(11), 2497–2506 (1994).

[32] Sangiorgi, R., Muolo, M. L., CHATAIN, D., and EUSTATHOPOULOS, N. *Journal of the American Ceramic Society* **71**(9), 742–748 (1988).

[33] Yu, R., Song, H., Zhang, X.-F., and Yang, P. *The Journal of Physical Chemistry B* **109**(15), 6940–6943 (2005).

[34] Ostwald, W. *Lehrbuch der Allgemeinen Chemie*, volume 2. Leipzig, Germany, (1896).

[35] Zhang, Z., Wang, Z., He, S., Wang, C., Jin, M., and Yin, Y. *Chemical Science* **6**(9), 5197–5203 (2015).

[36] Lifshitz, I. M. and Slyozov, V. V. *Journal of Physics and Chemistry of Solids* **19**(1-2), 35–50 (1961).

[37] Stavans, J. *Reports on progress in physics* **56**(6), 733–789 (1993).

[38] Stevenson, P. *Current Opinion in Colloid & Interface Science* **15**(5), 374–381 (2010).

[39] Wynblatt, P. and Gjostein, N. *Acta Metallurgica* **24**(12), 1165–1174 (1976).

[40] Chakraverty, B. *Journal of Physics and Chemistry of Solids* **28**(12), 2401–2412 (1967).

[41] Carraro, C., Maboudian, R., and Magagnin, L. *Surface Science Reports* **62**(12), 499–525 (2007).

[42] Brenner, A. and Riddell, G. E. *Plating and Surface Finishing* **85**(8), 54–55 (1998).

[43] Djokić, S., Djokić, N., Guthy, C., and Thundat, T. *Electrochimica Acta* **109**, 475–481 (2013).

[44] Gorostiza, P., Kulandainathan, M. A., Díaz, R., Sanz, F., Allongue, P., and Morante, J. R. *Journal of The Electrochemical Society* **147**(3), 1026–1030 (2000).

[45] Zhong, S., Yang, Z.-G., and Cai, J. *Journal of The Electrochemical Society* **152**(3), C143–C148 (2005).

[46] Magagnin, L., Maboudian, R., and Carraro, C. *Electrochemical and Solid-State Letters* **4**(1), C5–C7 (2001).

[47] Jain, P. K., Huang, X., El-Sayed, I. H., and El-Sayed, M. A. *Plasmonics* **2**(3), 107–118 (2007).

[48] Kreibig, U. and Vollmer, M. *Optical Properties of Metal Clusters*, volume 25. Springer Science & Business Media, (2013).

[49] Conde, J., Doria, G., and Baptista, P. *Journal of Drug Delivery* **2012**, 1–12 (2011).

[50] Huang, X., El-Sayed, I. H., Qian, W., and El-Sayed, M. A. *Journal of the American Chemical Society* **128**(6), 2115–2120 (2006).

[51] Wilson, A. J. and Willets, K. A. *Wiley Interdisciplinary Reviews: Nanomedicine and Nanobiotechnology* **5**(2), 180–189 (2013).

[52] Lin, H., Shao, Q., Hu, F., Wang, H., and Shao, M. *Thin Solid Films* **558**, 385–390 (2014).

[53] Shao, Q., Que, R., Shao, M., Cheng, L., and Lee, S.-T. *Advanced Functional Materials* **22**(10), 2067–2070 (2012).

[54] Raider, S., Flitsch, R., and Palmer, M. *Journal of The Electrochemical Society* **122**(3), 413–418 (1975).

[55] Verhaverbeke, S., Teerlinck, I., Vinckier, C., Stevens, G., Cartuyvels, R., and Heyns, M. *Journal of The Electrochemical Society* **141**(10), 2852–2857 (1994).

[56] Allongue, P., Costa-Kieling, V., and Gerischer, H. *Journal of the Electrochemical Society* **140**(4), 1018–1026 (1993).

[57] Allongue, P., de Villeneuve, C. H., Morin, S., Boukherroub, R., and Wayner, D. D. *Electrochimica Acta* **45**(28), 4591–4598 (2000).

[58] Allongue, P., Kieling, V., and Gerischer, H. *Electrochimica Acta* **40**(10), 1353–1360 (1995).

[59] Rivillon, S., Chabal, Y. J., Amy, F., and Kahn, A. *Applied Physics Letters* **87**(25), 253101–253104 (2005).

[60] Sayed, S. Y., Wang, F., Malac, M., Meldrum, A., Egerton, R. F., and Buriak, J. M. *ACS Nano* **3**(9), 2809–2817 (2009).

[61] Ghosh, T., Das, P., Chini, T. K., Ghosh, T., and Satpati, B. *Physical Chemistry Chemical Physics* **16**(31), 16730–16739 (2014).

[62] Dodson, B. W., Myers, D. R., Datye, A., Kaushik, V., Kendall, D., and Martinez-Tovar, B. *Physical Review Letters* **61**(23), 2681–2684 (1988).

[63] Markov, I. V. *Crystal Growth for Beginners: Fundamentals of Nucleation, Crystal Growth and Epitaxy*. World scientific, (2003).

[64] Warren, S., Reitzle, A., Kazimirov, A., Ziegler, J., Bunk, O., Cao, L., Renner, F., Kolb, D., Bedzyk, M., and Zegenhagen, J. *Surface Science* **496**(3), 287–298 (2002).

[65] Ito, K., Yamaura, D., and Ogino, T. *Electrochimica Acta* **214**, 354–361 (2016).

[66] Peng, K., Wu, Y., Fang, H., Zhong, X., Xu, Y., and Zhu, J. *Angewandte Chemie International Edition* **44**(18), 2737–2742 (2005).

[67] Carraro, C., Magagnin, L., and Maboudian, R. *Electrochimica Acta* **47**(16), 2583–2588 (2002).

[68] Fritz, M. C., Carraro, C., and Maboudian, R. *Tribology Letters* **11**(3), 171–175 (2001).

[69] Zhuo, K., Jeong, M.-G., and Chung, C.-H. *RSC Advances* **3**(31), 12611–12615 (2013).

[70] Zhang, Y., Ang, S., Tay, A. A., Xu, D., Kang, E., Neoh, K., Chong, L. P., and Huan, A. *Langmuir* **19**(17), 6802–6806 (2003).

[71] Niwa, D., Homma, T., and Osaka, T. *The Journal of Physical Chemistry B* **108**(28), 9900–9904 (2004).

[72] Sayed, S. Y., Daly, B., and Buriak, J. M. *The Journal of Physical Chemistry C* **112**(32), 12291–12298 (2008).

[73] Xie, S., Zhang, X., Xiao, D., Paau, M. C., Huang, J., and Choi, M. M. *The Journal of Physical Chemistry C* **115**(20), 9943–9951 (2011).

[74] Xie, S., Zhang, X., Yang, S., Paau, M. C., Xiao, D., and Choi, M. M. *RSC Advances* **2**(11), 4627–4631 (2012).

[75] Liu, R., Li, S., Yu, X., Zhang, G., Ma, Y., Yao, J., Keita, B., and Nadjo, L. *Crystal Growth & Design* **11**(8), 3424–3431 (2011).

[76] Gutes, A., Carraro, C., and Maboudian, R. *Journal of the American Chemical Society* **132**(5), 1476–1477 (2010).

[77] Wen, X., Xie, Y.-T., Mak, W. C., Cheung, K. Y., Li, X.-Y., Renneberg, R., and Yang, S. *Langmuir* **22**(10), 4836–4842 (2006).

[78] Huan, T. N., Kim, S., Van Tuong, P., and Chung, H. *RSC Advances* **4**(8), 3929–3933 (2014).

[79] Brevnov, D. A., Olson, T. S., López, G. P., and Atanassov, P. *The Journal of Physical Chemistry B* **108**(45), 17531–17536 (2004).

[80] Yang, L. and Luan, B. *Journal of The Electrochemical Society* **152**(7), C474–C481 (2005).

[81] Djokić, S. *Journal of the Electrochemical Society* **143**(4), 1300–1305 (1996).

[82] Srinivasan, R. and Suni, I. I. *Surface Science* **408**(1), L698–L702 (1998).

[83] Liu, F.-M. and Green, M. *Journal of Materials Chemistry* **14**(10), 1526–1532 (2004).

[84] Srinivasan, R. and Suni, I. I. *Journal of The Electrochemical Society* **146**(2), 570–573 (1999).

[85] Rossiter, C. and Suni, I. I. *Surface Science* **430**(1), L553–L557 (1999).

[86] Hormozi Nezhad, M. R., Aizawa, M., Porter, L. A., Ribbe, A. E., and Buriak, J. M. *Small* **1**(11), 1076–1081 (2005).

[87] Gorostiza, P., Allongue, P., Díaz, R., Morante, J. R., and Sanz, F. *The Journal of Physical Chemistry B* **107**(26), 6454–6461 (2003).

[88] Sun, Y. and Wiederrecht, G. P. *Small* **3**(11), 1964–1975 (2007).

[89] Okinaka, Y. and Hoshino, M. *Gold Bulletin* **31**(1), 3–13 (1998).

[90] Zhao, L., Siu, A. C.-L., Petrus, J. A., He, Z., and Leung, K. T. *Journal of the American Chemical Society* **129**(17), 5730–5734 (2007).

[91] D'Asaro, L., Nakahara, S., and Okinaka, Y. *Journal of the Electrochemical Society* **127**(9), 1935–1940 (1980).

[92] Porter, L. A., Choi, H. C., Ribbe, A. E., and Buriak, J. M. *Nano Letters* **2**(10), 1067–1071 (2002).

[93] Aizawa, M. and Buriak, J. M. *Journal of the American Chemical Society* **128**(17), 5877–5886 (2006).

[94] Bindra, P. and Roldan, J. *Journal of Applied Electrochemistry* **17**(6), 1254–1266 (1987).

[95] Ghosh, T., Kabiraj, D., and Satpati, B. In *AIP Conference Proceedings*, volume 1665, 080040–080043. AIP Publishing, (2015).

[96] Plieth, W. *Surface Science* **156**, 530–535 (1985).

[97] Makov, G., Nitzan, A., and Brus, L. E. *The Journal of Chemical Physics* **88**(8), 5076–5085 (1988).

[98] Ziegler, J. F. and Biersack, J. P. *Treatise on Heavy-Ion Science* , 93–129 (1985).

[99] Yoon, B., Akulin, V., Cahuzac, P., Carlier, F., De Frutos, M., Masson, A., Mory, C., Colliex, C., and Bréchignac, C. *Surface Science* **443**(1), 76–88 (1999).

[100] Chaki, N. K., Sharma, J., Mandle, A., Mulla, I., Pasricha, R., and Vijayamohanan, K. *Physical Chemistry Chemical Physics* **6**(6), 1304–1309 (2004).

[101] Ng, K. H., Liu, H., and Penner, R. *Langmuir* **16**(8), 4016–4023 (2000).

[102] Ivanova, O. S. and Zamborini, F. P. *Journal of the American Chemical Society* **132**(1), 70–72 (2009).

[103] Kuo, C. L. and Hwang, K. C. *Chemistry of Materials* **25**(3), 365–371 (2013).

[104] Redmond, P. L., Hallock, A. J., and Brus, L. E. *Nano Letters* **5**(1), 131–135 (2005).

[105] Henglein, A., Mulvaney, P., and Linnert, T. *Faraday Discussions* **92**, 31–44 (1991).

[106] Hu, X., Cahill, D. G., and Averback, R. S. *Journal of Applied Physics* **92**(7), 3995–4000 (2002).

[107] Satpati, B., Satyam, P., Som, T., and Dev, B. *Applied Physics A: Materials Science & Processing* **79**(3), 447–451 (2004).

[108] Chopra, K. and Bahl, S. *Physical Review B* **1**(6), 2545–2356 (1970).

[109] Barabási, A.-L. and Stanley, H. E. *Fractal Concepts in Surface Growth.* Cambridge university press, (1995).

[110] Jaouen, C., Delafond, J., and Riviere, J. *Journal of Physics F: Metal Physics* **17**(2), 335–350 (1987).

[111] Ghijsen, J., Tjeng, L. v., Van Elp, J., Eskes, H., Westerink, J., Sawatzky, G., and Czyzyk, M. *Physical Review B* **38**(16), 11322–11330 (1988).

[112] Koffyberg, F. and Benko, F. *Journal of Applied Physics* **53**(2), 1173–1177 (1982).

[113] Jayatissa, A. H., Guo, K., and Jayasuriya, A. C. *Applied Surface Science* **255**(23), 9474–9479 (2009).

[114] Zou, G., Li, H., Zhang, D., Xiong, K., Dong, C., and Qian, Y. *The Journal of Physical Chemistry B* **110**(4), 1632–1637 (2006).

[115] Gao, X., Bao, J., Pan, G., Zhu, H., Huang, P., Wu, F., and Song, D. *The Journal of Physical Chemistry B* **108**(18), 5547–5551 (2004).

[116] Wang, F., Tao, W., Zhao, M., Xu, M., Yang, S., Sun, Z., Wang, L., and Song, X. *Journal of Alloys and Compounds* **509**(41), 9798–9803 (2011).

[117] Pan, Q., Jin, H., Wang, H., and Yin, G. *Electrochimica Acta* **53**(2), 951–956 (2007).

[118] Zheng, S.-F., Hu, J.-S., Zhong, L.-S., Song, W.-G., Wan, L.-J., and Guo, Y.-G. *Chemistry of Materials* **20**(11), 3617–3622 (2008).

[119] Wang, B., Wu, X.-L., Shu, C.-Y., Guo, Y.-G., and Wang, C.-R. *Journal of Materials Chemistry* **20**(47), 10661–10664 (2010).

[120] Zhu, G., Xu, H., Xiao, Y., Liu, Y., Yuan, A., and Shen, X. *ACS applied Materials & Interfaces* **4**(2), 744–751 (2012).

[121] Huang, H., Zhang, L., Wu, K., Yu, Q., Chen, R., Yang, H., Peng, X., and Ye, Z. *Nanoscale* **4**(24), 7832–7841 (2012).

[122] Martinson, C. A. and Reddy, K. *Journal of Colloid and Interface Science* **336**(2), 406–411 (2009).

[123] Xu, M., Wang, F., Ding, B., Song, X., and Fang, J. *RSC Advances* **2**(6), 2240–2243 (2012).

[124] Masudy-Panah, S., Siavash Moakhar, R., Chua, C. S., Tan, H. R., Wong, T. I., Chi, D., and Dalapati, G. K. *ACS applied Materials & Interfaces* **8**(2), 1206–1213 (2016).

[125] Masudy-Panah, S., Radhakrishnan, K., Tan, H. R., Yi, R., Wong, T. I., and Dalapati, G. K. *Solar Energy Materials and Solar Cells* **140**, 266–274 (2015).

[126] Masudy-Panah, S., Dalapati, G. K., Radhakrishnan, K., Kumar, A., Tan, H. R., Naveen Kumar, E., Vijila, C., Tan, C. C., and Chi, D. *Progress in Photovoltaics: Research and Applications* **23**(5), 637–645 (2015).

[127] Gao, F., Liu, X.-J., Zhang, J.-S., Song, M.-Z., and Li, N. *Journal of Applied Physics* **111**(8), 084507–084511 (2012).

[128] Papadimitropoulos, G., Vourdas, N., Vamvakas, V. E., and Davazoglou, D. *Thin Solid Films* **515**(4), 2428–2432 (2006).

[129] Mahalingam, T., Chitra, J., Chu, J., Velumani, S., and Sebastian, P. *Solar Energy Materials and Solar Cells* **88**(2), 209–216 (2005).

[130] Kim, J. Y., Rodriguez, J. A., Hanson, J. C., Frenkel, A. I., and Lee, P. L. *Journal of the American Chemical Society* **125**(35), 10684–10692 (2003).

[131] Thouti, E., Chander, N., Dutta, V., and Komarala, V. K. *Journal of Optics* **15**(3), 035005–035012 (2013).

[132] Gutes, A., Laboriante, I., Carraro, C., and Maboudian, R. *The Journal of Physical Chemistry C* **113**(39), 16939–16944 (2009).

[133] Kwon, J.-Y., Yoon, T.-S., Kim, K.-B., and Min, S.-H. *Journal of Applied Physics* **93**(6), 3270–3278 (2003).

[134] Saxena, R., Frederick, M., Ramanath, G., Gill, W., and Plawsky, J. *Physical Review B* **72**(11), 115425–115432 (2005).

[135] Fillot, F., Tőkei, Z., and Beyer, G. *Surface Science* **601**(4), 986–993 (2007).

[136] Yang, X. H., Zeng, F. G., and Li, X. J. *Materials Science in Semiconductor Processing* **16**(1), 10–14 (2013).

[137] Gadkari, P., Warren, A., Todi, R., Petrova, R., and Coffey, K. *Journal of Vacuum Science & Technology A: Vacuum, Surfaces, and Films* **23**(4), 1152–1161 (2005).

[138] Lee, S. Y., Hummel, R., and Dehoff, R. *Thin Solid Films* **149**(1), 29–48 (1987).

[139] Figueiredo, V., Elangovan, E., Goncalves, G., Barquinha, P., Pereira, L., Franco, N., Alves, E., Martins, R., and Fortunato, E. *Applied Surface Science* **254**(13), 3949–3954 (2008).

[140] Johan, M. R., Suan, M. S. M., Hawari, N. L., and Ching, H. A. *International Journal of Electrochemcal Science* **6**, 6094–6104 (2011).

[141] Gondal, M., Qahtan, T. F., Dastageer, M. A., Maganda, Y., Anjum, D. H., et al. *Journal of Nanoscience and Nanotechnology* **13**(8), 5759–5766 (2013).

[142] Liu, W., Chen, W., Tsai, T., Hsieh, S., and Liu, C. *Applied Surface Science* **253**(12), 5516–5520 (2007).

[143] Gong, Y., Lee, C., and Yang, C. *Journal of Applied Physics* **77**(10), 5422–5425 (1995).

[144] Serin, N., Serin, T., Horzum, Ş., and Çelik, Y. *Semiconductor Science and Technology* **20**(5), 398–401 (2005).

[145] Ogwu, A., Bouquerel, E., Ademosu, O., Moh, S., Crossan, E., and Placido, F. *Acta Materialia* **53**(19), 5151–5159 (2005).

[146] Gu, C., Tu, J., and Zhang, T. *Applied Surface Science* **257**(5), 1779–1785 (2010).